

Noncontact Measurement of High Temperature Using Optical Fiber Sensors

Final Report

Contract no. NAG-1-831
R.O. Claus, Principal Investigator

Fiber & Electro-Optics Research Center
648 Whittemore Hall,
Dept. of Electrical Engineering
Virginia Tech
Blacksburg, VA 24061-0111

(NASA-CR-186975) NONCONTACT MEASUREMENT OF
HIGH TEMPERATURE USING OPTICAL FIBER SENSORS
Final Report (Virginia Polytechnic Inst.
and State Univ.) 95 p

N90-28825

CSSL 14B

G3/35 Unclas
0303804

Fiber & Electro-Optics
RESEARCH CENTER

**Noncontact Measurement of
High Temperature
Using Optical Fiber Sensors**

Final Report

**Contract no. NAG-1-831
R.O. Claus, Principal Investigator**

**Fiber & Electro-Optics Research Center
648 Whittemore Hall,
Dept. of Electrical Engineering
Virginia Tech
Blacksburg, VA 24061**

Contents

1.0 Accomplishments	1
1.1 Summary	2
1.2 Acknowledgements	3
2.0 Optical Fiber-based Ratio Pyrometry	4
2.1 Analytical Studies	4
2.1.1 Configuration Factor Analysis	6
2.1.2 Numerical Simulation	12
2.1.3 Model for Ratio Pyrometry	13
2.2 Laboratory Studies	15
2.2.1 Detector Linearity Test	15
2.2.2 Filter Tests	11
2.2.3 Optimization of Light Guide	16
2.3 Pyrometer Prototype Design	19
2.3.1 Physical Set-up	19
2.3.2 Prototype Pyrometer Testing	20
2.3.3 Test of Effects of Iris Diameter	22
2.4 Field Tests of Prototype Pyrometer at NASA MSFC	23
2.4.1 Calibration	23
2.4.2 Mounting Details	24
2.4.3 Data Acquisition	24
2.4.4 Data Analysis	25
2.4.4.1 Processing of Original Data	25
2.4.4.2 Processing of Filtered Data	26
2.4.5 Experimental Results	28
2.4.5.1 Original Data	28
2.4.5.2 Filtered Data	28
2.5 Conclusions and Recommendations	30
3.0 Optical Fiber Holography	31
3.1 Holographic Matched Filters for Processing Modal Domain Sensor Outputs	31
3.1.1 Holographic Matched Filters for Modal Domain Sensors	33
3.1.2 Theory	34
3.1.3 Experiment	36
3.1.4 Experimental Results for Matched Filter Holography	37
3.2 Evanescent Wave Holography	39
3.2.1 Principles of Evanescent Wave Holography with Optical Fibers	40

3.2.2	Theory	44
3.2.2.1	Recording of the Hologram	44
3.2.2.2	Reconstruction of the Hologram	47
3.2.2.3	Diffraction Efficiency	49
3.2.3	Experiment	50
3.2.3.1	Fiber Preparation	51
3.2.3.2	Fiber Coating	53
3.2.3.3	Experimental Set-up	55
3.2.3.4	Sensitization of Gelatin	56
3.2.3.5	Exposure and Development	57
3.2.3.6	Data	57
3.2.4	Discussion	58
3.2.5	Conclusions	59
4.0	Active Fiber Technology	60
4.1	Rare-earth Based Glass Amplifiers	60
4.1.1	Existing Techniques to Manufacture Rare-earth Fibers	60
4.1.2	Diffusion Technique to Fabricate Rare-earth Glass Rod	61
4.1.3	Optical Signal Amplification Experiment	63
4.1	Discussion	60
5.0	References	64

List of Appendices

Appendix A.	NASA1 FORTRAN Configuration Factor Model	53
Appendix B.	NASA2 FORTRAN Tilted Fiber Model	69
Appendix C.	Ratio Pyrometry Model	72
Appendix D.	Prototype Pyrometer Component List	74
Appendix E.	Data Transfer Program	76
Appendix F.	Published Papers Relating to Optical Fiber Holography	79

List of Figures

Figure 2.1. Geometry for radiative transfer model.....	7
Figure 2.2. Geometry for configuration factor.....	8
Figure 2.3. Geometry for tilted fiber	13
Figure 2.4 Spectral Characteristics of Blackbody Radiation and Narrow Band Filter.....	14
Figure 2.5 Theoretical Pyrometry Curve.....	15
Figure 2.6 Detector Linearity	15
Figure 2.7 Experimental Set-up for Filter Tests	16
Figure 2.8 Experimental Pyrometry Curve	17
Figure 2.9 Experimental Set-up for Fiber Tests	17
Figure 2.10 Detector Voltage using Hollow-core Fiber Bundles	18
Figure 2.11 Portable Pyrometer Set-up	19
Figure 2.12 Laboratory Set-up.....	20
Figure 2.13 Pyrometer Calibration Results	21
Figure 2.14 Effects of Iris Diameter	22
Figure 2.15 Effects of Iris Diameter on SNR.....	23
Figure 2.16 Calibration Curve at MSFC.....	24
Figure 2.17 Data Obtained from Niobium Processing.....	25
Figure 2.18.a Power Spectral Density for Channel 1.....	26
Figure 2.18.b Power Spectral Density for Channel 2	27
Figure 2.20 Butterworth Filters with cut-off @ 400 Hz	27
Figure 2.21 Ratio of Original Data.....	29
Figure 2.22 Ratio of Filtered Data	29
Figure 3.1 Typical output farfield pattern for two-mode fiber	32
Figure 3.2 Pin-hole processing of modal domain sensor output	32
Figure 3.3 Experimental set-up for writing matched filter	33
Figure 3.4 Experimental set-up for processing sensor output with matched filter	34
Figure 3.5 Alignment of mirrors and detector	37
Figure 3.6 Output of matched-filter processed sensor.....	38
Figure 3.7 Output of pinhole aperture sampled sensor	38
Figure 3.8 Recording of evanescent wave hologram in optical fiber	40
Figure 3.9 Refractive index variation of hologram in DCG.....	41
Figure 3.10 Reconstruction of the hologram	42
Figure 3.11 Illumination with the conjugate reference wave U_r^*	42
Figure 3.12 Illumination with the object wavefield U_o	43
Figure 3.13 Illumination with the conjugate object wavefield.....	43
Figure 3.14 Definition of beams employed in recording and reconstruction	45
Figure 3.15 Attachment of fiber to glass slide mount	52

Figure 3.16 Geometry for determination of depth of polish.....	52
Figure 3.17 Experimental set-up for exposure of hologram.....	55
Figure 4.1 Extended MCVD process for fabrication of rare-earth-based fibers.....	61
Figure 4.2 Set-up for diffusion experiment.....	62
Figure 4.3 Experiment for measurement of optical signal amplification.....	63

List of Tables

Table 2.1 Filter Spectral Characteristics	14
Table 2.2 Ratio of Unfiltered Data	26
Table 2.3 Ratio of Filtered Data	28
Table 3.1 Symbol notation	44
Table 3.2 Measured efficiencies for hologram reconstruction	57
Table 3.3 Procedure for Fabrication of Evanescent Wave Holograms.....	59

1.0 Accomplishments

- **Designed, assembled, and tested a prototype 2-color optical pyrometer on the 105-meter Microgravity Materials Processing Drop Tube at NASA Marshall Space Flight Center.**
- **Researched the application of holographic elements to optical fiber sensors.**
 - **Demonstrated use of holographic matched filters for processing outputs from fiberoptic modal domain sensors.**
 - **Demonstrated writing of evanescent wave gratings in the modified cladding of an optical fiber.**
- **Researched techniques for doping optical fibers and glass rods with lanthanide rare earths for low cost fabrication of optical amplifiers and temperature.**

1.1 Summary

The primary goal of this research program was the investigation and application of noncontact temperature measurement techniques using optical techniques and optical fiber methods. In particular, a pyrometer utilizing an infrared optical light pipe and a multiwavelength filtering approach was designed, revised, and tested. This work was motivated by the need to measure the temperatures of small metallic pellets (3 mm diameter) in free fall at the Microgravity Materials Processing Drop Tube at NASA Marshall Space Flight Center. In addition, research under this program investigated the adaptation of holography technology to optical fiber sensors, and also examined the use of rare-earth dopants in optical fibers for use in measuring temperature.

The pyrometer development effort involved both theoretical analysis and experimental tests. For the analysis, a mathematical model based on radiative transfer principles was derived. Key parameter values representative of the drop tube system, such as particle size, tube diameter and length, and particle temperature, were used to determine an estimate of the radiant flux that will be incident on the face of an optical fiber or light pipe used to collect radiation from the incandescent falling particle. An extension of this work examined the advantage of inclining or tilting the collecting fiber to increase the time that the falling particle remains in the fiber field-of-view. Those results indicate that increases in total power collected of about 15% may be realized by tilting the fiber.

In order to determine the suitability of alternative light pipes and optical fibers, and experimental set-up for measuring the transmittance and insertion loss of infrared fibers considered for use in the pyrometer was assembled. A zirconium fluoride optical fiber and several bundles of hollow core fiber of varying diameters were tested. Results indicated that these waveguides suffered from high attenuation, and that the incident power fluxes measured at the detector were insufficient to maintain an adequate signal-to-noise ratio when used to measure the temperatures of small particles. A one-inch diameter calcium fluoride rod was later successfully tested, and subsequently incorporated into the pyrometer design.

A prototype two-color pyrometer was assembled and tested at Virginia Tech, and then tested on the Drop Tube at NASA Marshall SFC. Radiation from 5 mm diameter niobium drops falling in the Drop Tube was successfully detected, and recorded for later analysis. Subsequent analysis indicated that the imaging of light output from the light pipe onto the detector active areas was not identical for both detectors. In addition, this variation between detector coupling appears to have depended on the position of the falling particle as it fell. This variation in coupling introduced a large error into the data, resulting in a large uncertainty in establishing the actual temperature of the falling particle.

Research into the application of holography technology to optical fiber sensors was conducted in two areas: the use of holographic matched filters for processing the outputs of fiber optic "modal domain" strain sensors, and the writing of holographic gratings into the claddings of modified optical fibers. Holographic matched filters were used to improve the processing of output signals from optical fiber strain sensors that utilize mode-mode interference in a few-mode fiber (so-called "modal domain sensors"). The holographic filter approach should prove more rugged than alternative processing approaches since the matched filters lend themselves more easily to construction in a monolithic package. Evanescent wave gratings were successfully written in a dichromated gelatin emulsion that was integrated into the cladding of an optical fiber. The gratings demonstrated the diffraction of light propagating in the optical fiber through the interaction of the evanescent field of the propagating modes with the grating. The evanescent wave holograms are expected to have applications in optical time domain reflectometry (OTDR) based sensors and for controlling the modes in modal domain sensors.

Research was initiated into the development of low cost techniques for doping glass rods with lanthanide rare earth in order to render the rods capable of amplification of optical signals. Samples were prepared by indiffusion of neodymium into soda lime glass, but the level of doping could not be measured due to limits of the available spectroscopic instruments. Optical signal amplification was not observed experimentally. Optical fibers doped with rare earths are expected to have applications for signal amplification in optical communications, and as distributed temperature sensors due to the temperature dependence of the fluorescence of rare earths.

1.2 Acknowledgements

We gratefully acknowledge the sponsorship of NASA Langley Research Center. Additionally, we are indebted to Dr. Mike Robinson of NASA Marshall Space Flight Center for making the Drop Tube available for tests. Tom Rathz of the University of Alabama, Huntsville, and his crew at the Drop Tower were extremely helpful during testing.

We are also obliged to Prof. Guy Indebetouw of the Virginia Tech Physics Department for providing laboratory space and equipment for the matched filter experiments, and for outlining the theoretical analysis for those experiments.

2.0 Optical Fiber-based Ratio Pyrometry

The main emphasis of this research program has been the development of an instrument capable of measuring the temperature of a small (~3 mm diameter) metallic pellet in free fall. Such pellets are typical of experiments performed at the NASA Marshall Space Flight Center Drop Tube in Huntsville, Alabama. The Drop Tube is an evacuated, 105-m tall tube which allows researchers the facilities to perform materials processing experiments in a low-g environment.¹ Typical Drop Tube experiments to study solidification or containerless processing start by heating a small sample of material at the top of the tube by an electron-beam furnace or an electromagnetic levitation/RF heating furnace. After the sample becomes molten, it is dropped into the tube. As the drop falls for the 4.5 seconds of free fall, it cools and solidifies. The sample can be retrieved from a trap at the bottom of the tube, and materials analyses are then performed on the sample.

It would be highly desirable to determine the temperature history of a sample as it drops down the tube. Currently, this is estimated by applying the principles of heat transfer to the known initial temperature of the sample and the elapsed time of the drop.² Some confidence in this analytically determined temperature history could be provided by measuring the temperature of the sample at one or more points along its drop with a noncontact temperature measurement system. Preliminary experiments towards this end were performed by Hoffmeister and Bayuzik.³ Their approach utilized two-color pyrometry with silicon detectors, a fused silica lightpipe, and bandpass filters centered at 900 nm and at 650 nm. The use of silicon detectors effectively limits the measurement range of the instrument to a minimum of about 1600° C, due to the abrupt drop in responsivity of the detectors above 1.1 μm. The pyrometer developed in this research was intended to extend this temperature range down to 200° C by adopting indium antimonide detectors, calcium fluoride lenses, and a calcium fluoride light pipe.

2.1 Analytical Studies

Every physical body above absolute zero in temperature emits spectral radiation which is dependent on its temperature. Planck's law describes radiation of the ideal thermal radiator, a blackbody, and is given below:

$$W_{\lambda} = \frac{C_1}{\lambda^5 [e^{C_2/(\lambda T)} - 1]} \quad (2.1)$$

where:

W_λ : hemispherical spectral radiant energy

C_1 : 37,413 [W $\mu\text{m}^4/\text{cm}^2$]

C_2 : 14,388 [$\mu\text{m K}$]

λ : wavelength of radiation [μm]

T : absolute temperature of blackbody [K]

The radiation of a greybody, a real thermal radiator, deviates from blackbody radiation by a quantity called the hemispherical spectral emittance, $\epsilon_{\lambda,T}$, and is defined by:

$$\epsilon_{\lambda,T} = \frac{W_{\lambda a}}{W_\lambda} \quad (2.2)$$

The radiation and total power, respectively, from a greybody can be written as:

$$W_{\lambda a} = \frac{C_1 \epsilon_{\lambda,T}}{\lambda^5 [e^{C_2/(\lambda T)} - 1]} \quad (2.3)$$

$$W_{\text{ta}} = C_1 \int_0^\infty \frac{\epsilon_{\lambda,T}}{\lambda^5 [e^{C_2/(\lambda T)} - 1]} d\lambda \quad (2.4)$$

Note that $\epsilon_{\lambda,T}$ varies with both λ and T , and is usually different for different materials. The ratio, or two-color, pyrometry technique can measure temperature relatively independent of variations in emissivity. The method requires that the total power, W_{ta} , be determined for two different wavelengths and then the ratio of these two W_{ta} s be taken as a measure of temperature. If the wavelengths are closely spaced so that the emissivity has not changed significantly, then the spectral emittance, $\epsilon_{\lambda,T}$, can be approximated as constant and will cancel from the ratio. This can be shown numerically as:

$$\frac{W_{\text{ta}1}}{W_{\text{ta}2}} = \frac{\epsilon_{\lambda_1}}{\epsilon_{\lambda_2}} \left(\frac{\lambda_2}{\lambda_1} \right)^5 e^{(C_2/T)(1/\lambda_2 - 1/\lambda_1)} \quad (2.5)$$

where $\epsilon_{\lambda_1} \approx \epsilon_{\lambda_2}$.

2.1.1. Configuration Factor Analysis

The free fall of the heated pellet in the drop tube results in its presence within the field-of-view of the fiber for a very short interval of time. Consequently, the amount of radiant flux incident on the fiber face is very small. A mathematical model has been derived to determine the amount of radiant flux incident on the fiber face. Using this model, a computer program was written to yield numerical values representative of the proposed measurement system.

The following assumptions were made:

- (1) The pellet is falling through the geometric center of the drop-tube.
- (2) The pellet is spherical in shape.
- (3) The fiber face area is negligible compared to the pellet surface area.
- (4) The radiation emitted by the pellet towards the fiber, as it is in the process of 'entering' and 'leaving' the field-of-view of the fiber, is neglected. In other words, the radiation when the pellet is in the field-of-view is considered to be constant from point (1) to point (2), as shown in Figure (1).
- (5) The radiation from the fiber towards the pellet is neglected.
- (6) The velocity of the pellet within the field-of-view of the fiber is constant.
- (7) The temperature of the pellet within the field-of-view of the fiber is constant.

One of the mathematical difficulties in treating radiative transfer between surfaces is accounting for the geometric relations involved in how the surfaces view each other. A method of accounting for the geometry is introduced in the form of a quantity called the "geometric configuration factor." This greatly simplifies the analysis.

First the configuration factor of the system as shown in Figure 2.1 will be found. Figure 2.2 shows the fiber face area as a differential element dA_1 , and the pellet as a sphere of surface area A_2 . The orientation is such that the normal to the center of the differential element passes through the center of the sphere. The standard result of the configuration factor of the system shown in Figure 2.2 is

$$F_{d1-2} = \left[\frac{r_2}{h} \right]^2. \quad (2.6)$$

For the case when the pellet is directly in front of the fiber as shown in Figure 2.1, equation 2.6

becomes

$$F_{d1-2} = \left[\frac{r_2}{L} \right]^2 \quad (2.7)$$

where L = radius of the drop tube.

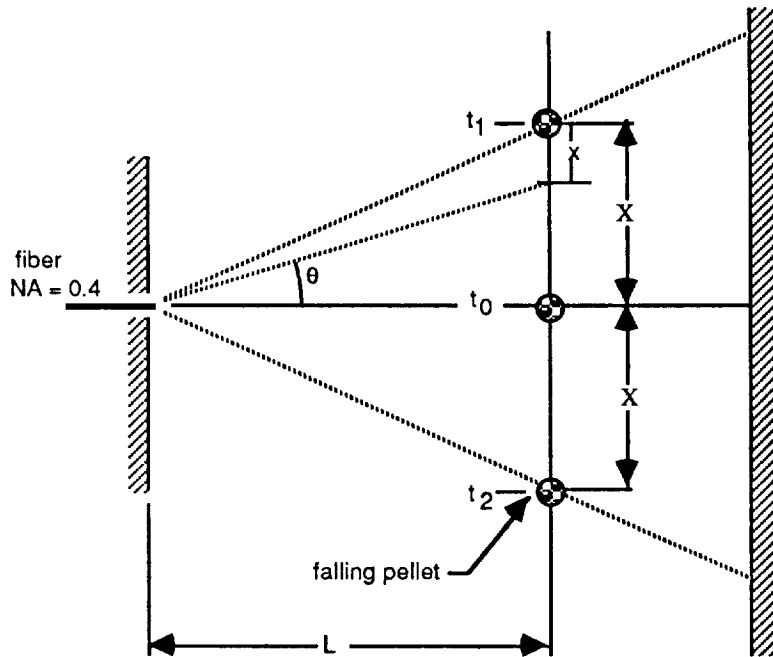


Figure 2.1. Geometry for radiative transfer model.

Since we are considering the flow of radiant flux from A_2 to dA_1 , we need to find dF_{2-d1} (the configuration factor needed for calculating energy flow from A_2 to dA_1). The reciprocity relation

between a differential element and a finite area states that

$$A_2 dF_{2-d1} = dA F_{d1-20} \quad (2.8)$$

or

$$dF_{2-d1} = \frac{dA_1}{A_2} F_{d1-20} \quad (2.9)$$

where

dA_1 = area of fiber face

A_2 = surface area of the pellet.

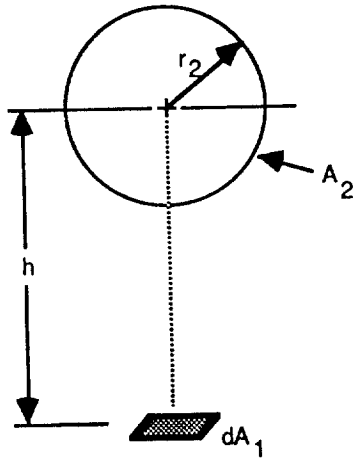


Figure 2.2. Geometry for configuration factor.

Since $A_1 = \pi r_1^2$, then $dA_1 = 2\pi r_1 dr_1$ and

$$dF_{2-d1} = \frac{2\pi r_1}{A_2} F_{d1-2} dr_1. \quad (2.10.a)$$

The area of the sphere presented to the fiber is $A_2 = \pi r_2^2$, so

$$dF_{2-d1} = \frac{2\pi r_1}{\pi r_2^2} F_{d1-2} dr_1. \quad (2.10.b)$$

The relation in equation (2.10) assumes that the normal to the fiber face passes through the center of the spherical pellet. Therefore, in order to consider for the cases when the pellet is at some angle, the component of the fiber face area is taken which is such that the normal to the component always passes through the center of the spherical pellet.

Therefore equation (2.10) becomes

$$dF_{2-d1} = \frac{2\pi r_1 \cos \theta}{\pi r_2^2} \left[\frac{r_2}{L} \right]^2. \quad (2.11)$$

Now, θ is a function of "x," as shown in Figure 2.1, and θ is related to the geometry by

$$\cos \theta = \frac{L}{\sqrt{L^2 + (X-x)^2}}. \quad (2.12)$$

In equation (2.12), the quantities "L" and "X" are constant and "x" varies with time "t." Writing "x" in terms of "t," we get

$$x = \left(\frac{2X}{\Delta T} \right) t \quad (2.13)$$

where,

ΔT = Time for which the pellet is in the field-of-view,

$2X$ = Total vertical distance traveled through the field-of-view,

and "t" varies from t_1 to t_2 as shown in Fig. (2.1).

Now, equation (2.12) becomes

$$\cos \theta = \frac{L}{\sqrt{L^2 + \left\{ X - \left(\frac{2X}{\Delta T} \right) t \right\}^2}}. \quad (2.14)$$

Substituting (2.14) in (2.13), we get

$$dF_{2-d1} = \frac{2r_1}{\sqrt{L^2 + \left\{ X - \left(\frac{2X}{\Delta T} \right) t \right\}^2}} \left(\frac{r_2}{L} \right)^2 dr_1. \quad (2.15)$$

The radiant flux incident on the incremental area dA_1 of the fiber end at a given time t is

$$dQ_{2-d1}(t) = \sigma K^4 A_2 dF_{2-d1}(t), \quad (2.16)$$

where

dQ_{2-d1} = incremental flux incident on the fiber face,

σ = Stephan - Boltzmann constant = 5.66961×10^{-8} W/m²K⁴.

K = temperature of pellet (source), and

A_2 = surface area of the pellet.

To find the total flux incident on the entire fiber end over the entire time that the pellet remains within the fiber field-of-view (FOV), equation 2.16 is integrated over the area of the fiber end and over the time interval that the pellet is within the fiber numerical aperture. Since the fiber is horizontal, and its field-of-view is symmetrical with respect to the horizontal, the total time duration of the fiber in the FOV is twice the time interval t_1 - t_0 (Figure 2.1). Thus

$$\begin{aligned} Q_{2-1} &= 2 \int_{t_1}^{t_0} \int_0^a \sigma K^4 A_2 dF_{2-d1}(t) dt \\ &= 2 \int_{t_1}^{t_0} \int_0^a \sigma K^4 \pi r_2^2 \left(\frac{2\pi r_1}{\pi \sqrt{L^2 + \left(X - \frac{2X}{\Delta T}t\right)^2}} \right) dr_1 dt \end{aligned} \quad (2.17)$$

where a is the radius of the fiber core. Simplifying this result and performing the first integral leads to

$$Q_{2-1} = \int_{t_1}^{t_0} \frac{\sigma K^4 r_2^2 a^2}{\sqrt{L^2 + X^2 - \frac{4X}{\Delta T}t + \left(\frac{2X}{\Delta T}\right)^2 t^2}} dt. \quad (2.18)$$

As it is assumed that the temperature of the pellet remains constant during the short interval of time the pellet is in the field-of-view of the fiber, we find that equation (2.17) has all the terms constant except dF_{2-d1} , which varies with time.

Let

$$A = L^2 + X^2,$$

$$B = -\left(\frac{4X^2}{\Delta T}\right), \text{ and}$$

$$C = \left(\frac{2X}{\Delta T}\right)^2.$$

Substituting A,B and C in equation (2.18), we have

$$Q_{2-1} = \int_1^b \frac{\sigma K^4 r_2^2 a^2}{\sqrt{A + Bt + Ct^2}} dt. \quad (2.19)$$

From standard integral tables

$$\int \frac{dx}{\sqrt{a + bx + cx^2}} = \frac{1}{\sqrt{c}} \log(2\sqrt{c[a + bx + cx^2]} + 2cx + b) \quad (2.20)$$

then equation (2.19) becomes

$$Q_{2-1} = \sigma K^4 r_2^2 a^2 \sqrt{\frac{\Delta T}{2X}} \left\{ \log \left(2\sqrt{\frac{2X}{\Delta T} \left[(L^2 + X^2) - \left(\frac{4X^2}{\Delta T}\right) t_0 + \left(\frac{2X}{\Delta T}\right) t_0^2 \right]} + \frac{4X}{\Delta T} t_0 - \frac{4X^2}{\Delta T} \right) \right. \\ \left. - \log \left(2\sqrt{\frac{2X}{\Delta T} \left[(L^2 + X^2) - \left(\frac{4X^2}{\Delta T}\right) t_1 + \left(\frac{2X}{\Delta T}\right) t_1^2 \right]} + \frac{4X}{\Delta T} t_1 - \frac{4X^2}{\Delta T} \right) \right\} \quad (2.21)$$

Equation (2.21) is the expression that relates the total radiant flux incident on the fiber face to the fiber parameters and the speed with which the pellet transits the fiber's field of view.

The derivation above requires the assumption that the fiber end face area is negligible compared with the pellet area. An alternate technique developed by Feinhold and Gupta to calculate the configuration factors in radiation from spheres does not require this assumption. In addition, complex formulae involving multiple integrals, which often could only be solved using numerical methods, can be avoided.⁴ This technique leads to extremely simple formulae and was used to determine the configuration factor for the drop tube geometry.

When employing the Feinhold and Gupta technique, it is not necessary to assume that the fiber face area is negligible with respect to the pellet area. The configuration factor obtained is valid for general A_1 and A_2 , and does not limit $A_2 \gg A_1$. It is found to be

$$F_{1-2} = \frac{1}{2} \left(1 - \frac{1}{\sqrt{1 + (r_1/L)^2}} \right) \quad (2.22)$$

Applying the Binomial Theorem to the above result (for $r_1 \ll L$) results in

$$\begin{aligned} F_{1-2} &= \frac{1}{2} \left(1 - \frac{1}{\sqrt{1 + (r_1/L)^2}} \right) \approx \frac{1}{2} \left(1 - \frac{1}{1 + \frac{1}{2}(r_1/L)^2} \right) \\ &= \frac{1}{2} \left(\frac{\frac{1}{2}(r_1/L)^2}{1 + \frac{1}{2}(r_1/L)^2} \right) \approx \frac{1}{4} \left(\frac{r_1}{L} \right)^2. \end{aligned} \quad (2.23)$$

The configuration factor thus obtained (equation 2.23) from the method of Feinhold and Gupta agrees in magnitude with the relation (equation 2.7) that requires that $A_2 \gg A_1$.

2.1.2. Numerical Simulation

The model derived in Section 2.1.1 was coded into a FORTRAN computer program named NASA1 FORTRAN (Appendix A). The resulting data gives the resulting incident radiant flux "Q" in watts for different temperatures "K" in Kelvin, for the time that the pellet remains in the field of view at various distances "H" down the tube in meters, starting from the top of the drop tube. For these calculations the pellet was assumed to be 3 mm in diameter, and the fiber had core diameter of 200 μm and NA of 0.4. Also, the drop tube was assumed to be of radius 6 inches.

The results indicated that the radiant flux incident on a 200 micron fiber (with NA of 0.4), 10 meters down the drop-tube and at temperature 773 K is 0.45×10^{-11} Watts. This number decreases as we move down the drop tube (e.g. at 190 meters down the drop-tube it falls down to 0.5×10^{-13} Watts). Further, at higher temperatures, we find that the amount of incident radiant flux increases. At a temperature of 3773 K and 10 meters down the drop-tube, the value becomes 0.25×10^{-8} Watts. It should be noted that these numbers are for an ideal case, as the falling pellet is assumed to be a blackbody. These numbers would further decrease if the falling pellet is considered to be a gray body and other effects like attenuation of fiber, such as an anti-reflection coating, or stray reflections from the inside wall of drop-tube are taken into account.

The field-of-view and hence the transit time of the pellet in the field-of-view can be increased by orienting the fiber at an angle with respect to the vertical wall of the drop tube. This approach is

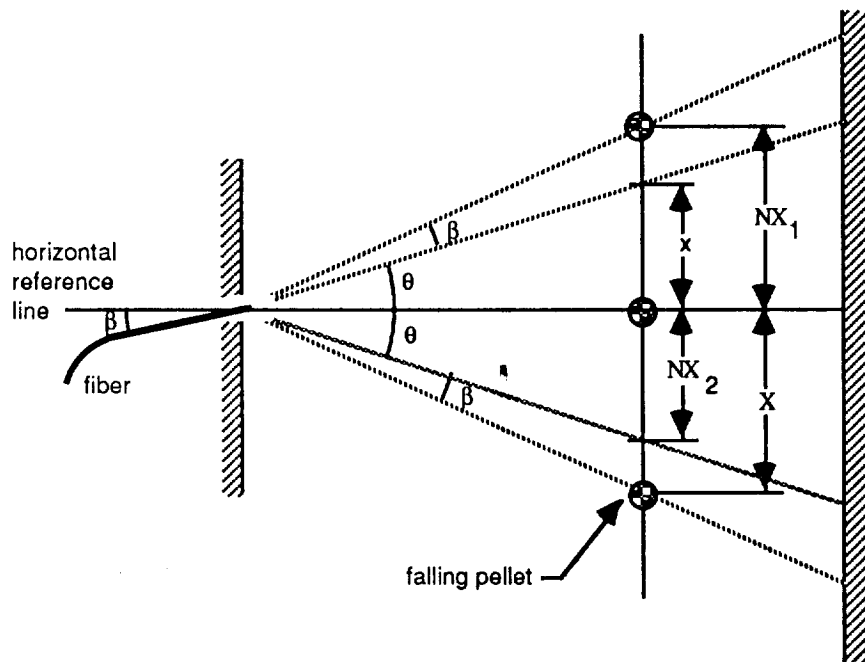


Figure 2.3. Geometry for tilted fiber.

shown in Figure (3). Here β , the angle by which the fiber is tilted, is assumed to be less than θ , where $\theta = \sin^{-1}(NA)$, where NA is the numerical aperture of the fiber. The relations for increased fiber tilt were programmed into program NASA2 FORTRAN (Appendix B).

The results from program NASA2, corresponding to a pellet temperature 2773 K, show that the radiant flux incident on the fiber-face, 10 meters down the drop-tube, and tilted at an angle of 20° with respect to the horizontal, is 0.87×10^{-9} Watts. This corresponds to a 17.6% increase in the incident radiant flux over the case of the non-tilted fiber. Similarly, at 190 meters down the drop-tube, with the fiber tilted at 20° , it becomes 0.1×10^{-10} Watts, which corresponds to a 12.4% increase in the incident radiant flux. As we move down the drop-tube, both the time in which one pellet remains in the field-of-view and the incident radiant flux decrease appreciably.

2.1.3. Model for Ratio Pyrometry

A set of infrared narrow band filters was selected to investigate ratio pyrometry experimentally. To take advantage of the temperature range of an IRCON blackbody calibrator (650°C - 1200°C) that was chosen as a source, the bandpass filters with specifications shown in Table 2.1 were chosen. The spectral characteristics of the filters are shown graphically with respect to theoretical radiance curves of the blackbody calibrator in Figure 2.4.

	<u>center wavelength</u>	<u>half peak bandwidth</u>
FILTER 1:	2.8225 μm	119 nm
FILTER 2:	3.1191 μm	107 nm

Table 2.1
Filter Spectral Characteristics

A FOPTRAN program was written in order to determine a theoretical model for the radiant energy available at the detectors after filtering (see Appendix C). The program uses a numerical integration subroutine which evaluates Planck's equation describing blackbody radiation, over the wavelength limits of each filter respectively as the temperature is varied from 500° C-3500° C. The filter output as a function of temperature can be expressed as

$$F_1(T) = \int_{f_1} \frac{\epsilon_{\lambda,T} C_1}{\lambda^5 [e^{C_2/(\lambda T)} - 1]} d\lambda \quad (2.14)$$

and

$$F_2(T) = \int_{f_2} \frac{\epsilon_{\lambda,T} C_1}{\lambda^5 [e^{C_2/(\lambda T)} - 1]} d\lambda. \quad (2.15)$$

The program then calculates the ratio of the energy, F_1/F_2 , at each temperature to obtain a single-valued curve which is a function of temperature and independent of source spectral emissivity. The theoretical model obtained is shown in Figure 2.5.

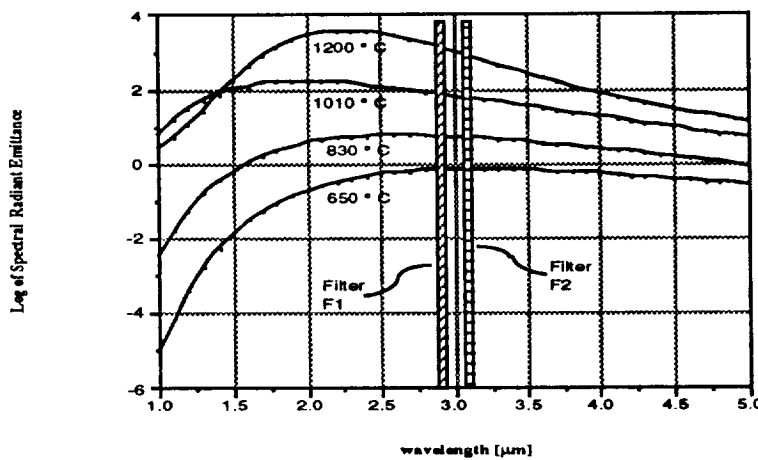


Figure 2.4
Spectral Characteristics of Blackbody Radiation and Narrow Band Filters

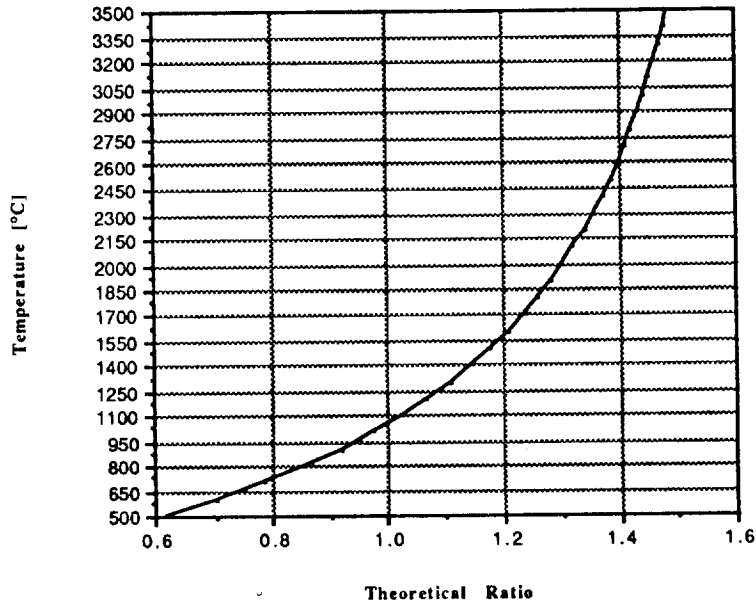


Figure 2.5
Theoretical Pyrometry Curve

2.2 Laboratory Studies

2.2.1 Detector Linearity Test

Two EG&G JUDSON Indium Antimonide (InSb) detectors were selected for use in the pyrometry experiments. The detectors, which are liquid nitrogen cooled, are responsive to light from 1-5 μm .

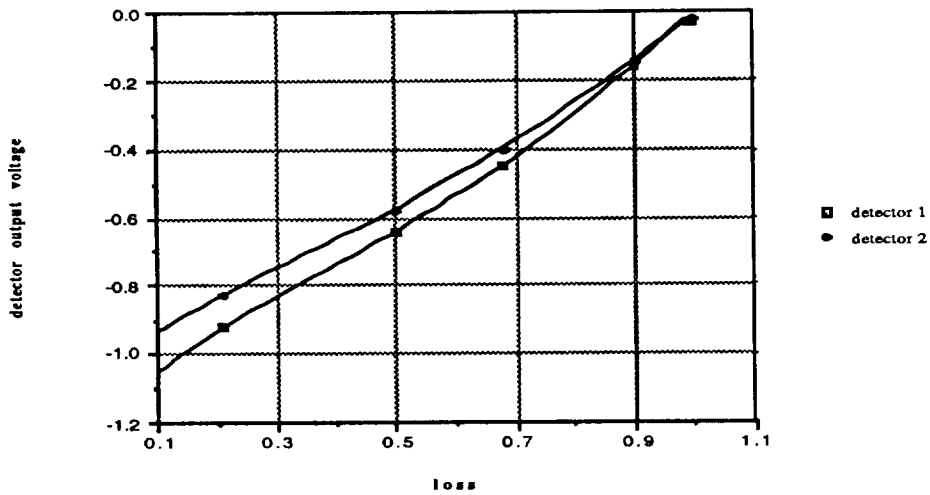


Figure 2.6
Detector Linearity

Using calibrated neutral density filters, the linearity of both detectors was investigated. With the blackbody source radiating at 1200 ° C, the results are shown in Figure 2.6. The results illustrated in Figure 2.6 show that both detectors behave linearly.

2.2.2 Filter Tests

In order to determine if the filters selected for the pyrometry experiment would yield a single-valued curve with respect to source temperature, a simple experiment was performed. The experimental set-up is shown in Figure 2.7. As the temperature of the blackbody calibrator was varied from 650° C-1200° C at increments of 50° C, detector voltage values were recorded for both narrow band filters. The results of the ratio of the detector voltages at particular temperatures are shown in Figure 2.8. An exponential curve is shown interpolated to the experimental data, and the theoretical model has been overlaid for comparison.

The experimental results were extremely close to the theoretical model which was discussed earlier, with differences probably due to idealized filter parameters used in the theoretical model.

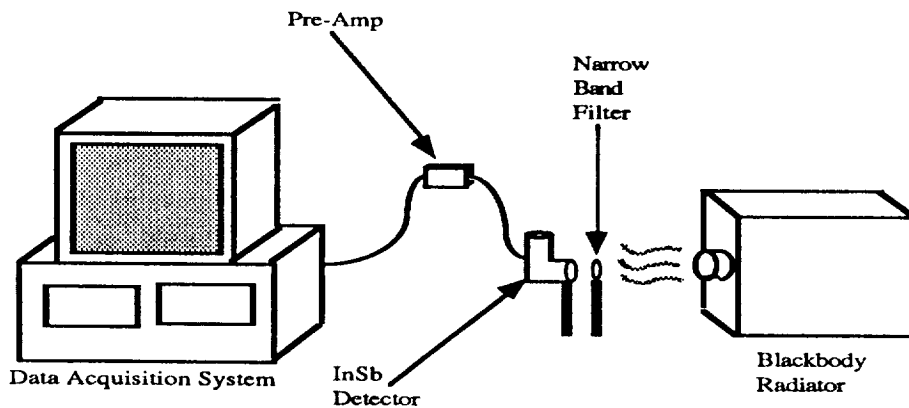


Figure 2.7
Experimental Set-up for Filter Tests

2.2.3 Optimization of Light Guide

In order to determine if enough power is present at the detector when using fibers to guide the infrared radiation, the experiment illustrated in Figure 2.9 was performed. First, a single zirconium fluoride fiber, one meter long, was investigated. Due to the small core diameter (200 μm) and high losses in the test grade fiber, insufficient power was intercepted from the blackbody, and the power delivered to the detector was below the noise floor of the detector. Due

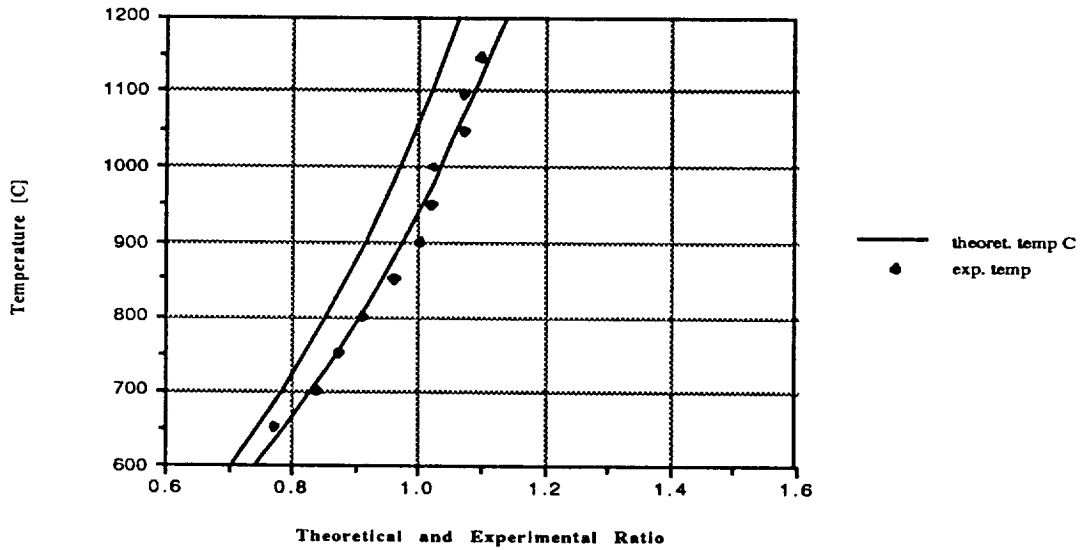


Figure 2.8
Experimental Pyrometry Curve

to the expense and limited availability of experimental IR fibers such as zirconium fluoride, experiments with IR fiber bundles were impractical. For this reason, a circular bundle of hollow-core optical fibers, drawn at Virginia Tech's Fiber & Electro-Optics facility, was investigated.

Recent studies involving hollow-core fibers and tubes have shown their ability to guide IR radiation^{5,6,7}. Hollow-core fibers, which use air as the radiation transmitting medium, guide radiation by a different mechanism than step-index fibers, which rely on a sequence of total internal reflections at the core-cladding interface. In hollow-core fibers, only rays with a very small angle

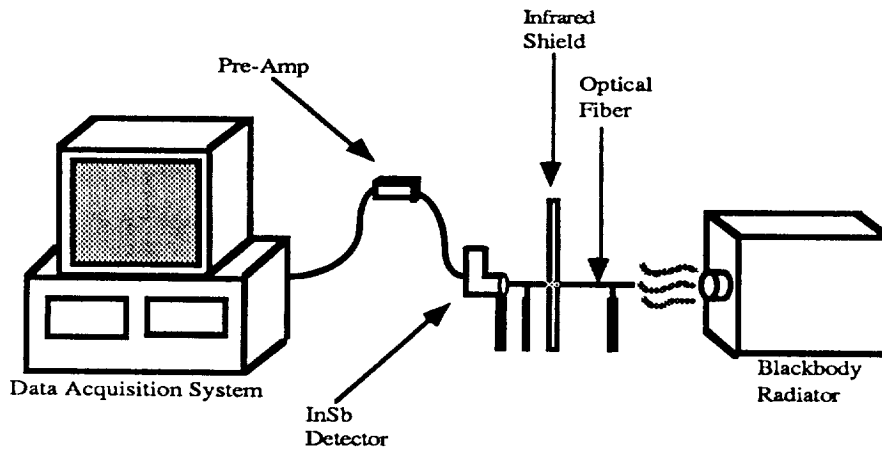


Figure 2.9
Experimental Set-up for Fiber Tests

of incidence to the air-wall interface will be significantly reflected back towards the center of the fiber and consequently guided. Due to this manner of light guiding, one of the most serious problems in hollow-core waveguides is high loss due to bending, as well as loss due to small NA.

Two bundles of hollow-core fiber were investigated. One of the fiber bundles investigated consisted of 35 fibers developed and manufactured at Virginia Tech, all one foot long, with inner-core diameters of 245 μm . The second bundle, manufactured by Hughes Aircraft Company, consisted of 3 fibers, one foot long, with inner-core diameters of 42 mm. The total outer diameter of both fiber bundles was approximately 5.6 mm. The fibers were held straight and a shield was placed in front of the InSb detector to insure that only the light which passes through the fiber bundle arrived at the detector. The detector voltage was recorded as the temperature of the blackbody source was varied from 650° C-1200° C at 50° C increments. The results are shown in Figure 2.10.

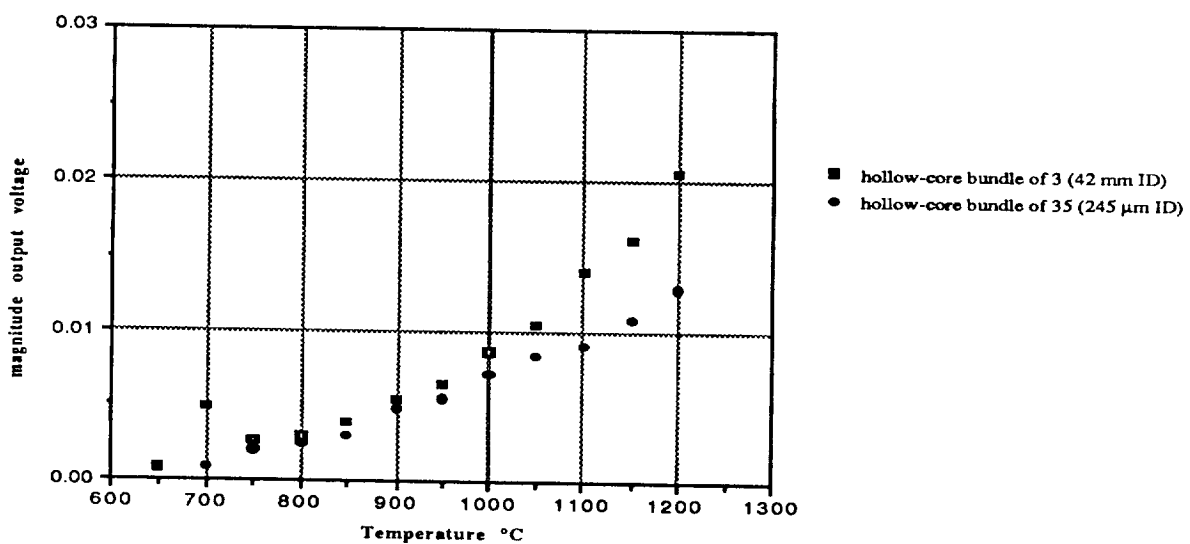


Figure 2.10
Detector Voltage using Hollow-core Fiber Bundles

The results obtained from the experimental test are consistent with theory. Experimentally, we observe more power being guided through the fiber bundle as the temperature of the source is increased. We also see that the bundle of fibers with the larger core diameters transmitted more

power. Although the transmittance of these bundles was greater than that of the zirconium fluoride fiber, it was not sufficient for a high signal-to-noise ratio when used in conjunction with the narrow-band infrared filters. The option of larger bundles was considered, but problems implementing these at the drop tube were foreseen. Due to the hollow nature of these fibers, evacuating the drop tube would become a problem. A calcium fluoride substrate would need to be vacuum-fitted to the tube in the flange to prevent outgassing. The hollow core fibers would then view the molten particle through this substrate. In order to avoid this complexity, other options were considered. The most feasible approach was to obtain and test a calcium fluoride rod of a standard diameter, so that common vacuum fittings could be easily obtained and used at the drop tube. A calcium fluoride rod, 1 inch in diameter and 6 inches in length, was obtained and tested in the laboratory. The resulting were promising and the rod was incorporated into the pyrometer set-up.

2.3 Prototype Pyrometer Design

2.3.1 Physical Set-up

A portable box with removable lid was constructed in order that the pyrometer could be mounted on the drop-tube at Marshall Space Flight Center (MSFC) in Huntsville, Alabama. Figure 2.11 is a top view of component location in the prototype box. A detailed list of components used is given in Appendix D.

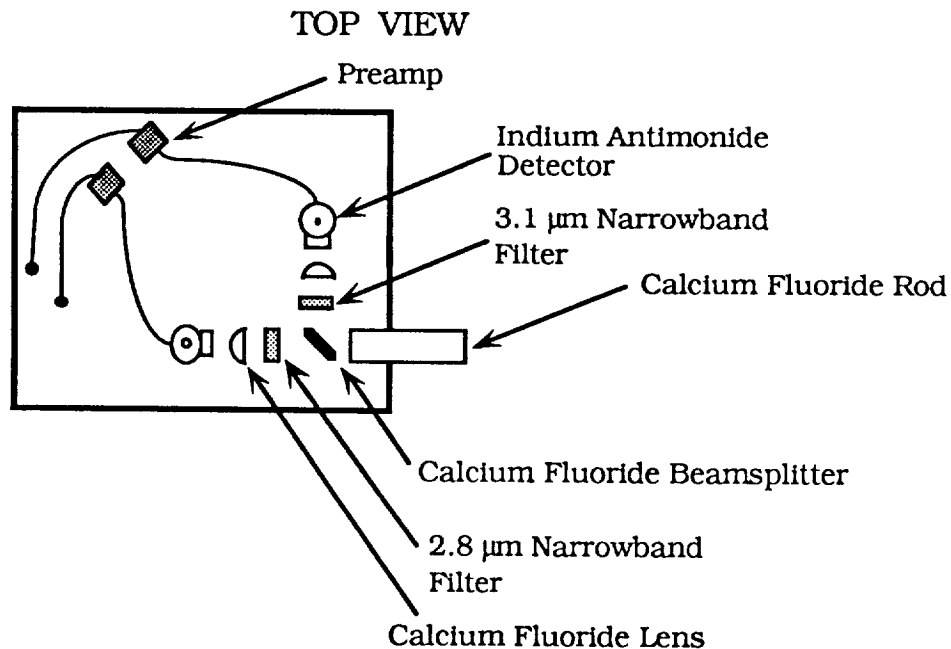


Figure 2.11
Portable Pyrometer Set-up

2.3.2 Prototype Pyrometer Testing

In order to determine the temperature of a molten object within the pyrometers field-of-view, an experiment was run to establish a calibration curve. The experiment was run several times in order to look at the repeatability of the experiment. The set-up for the laboratory experiment is shown in Figure 2.12. The Iron blackbody radiator (model BCH), which has an emissivity ≥ 0.99 and is calibrated for the temperature range of $650^{\circ}\text{C} - 1200^{\circ}\text{C}$, was placed 6 inches away from the end of the rod. A metal sheet with a variable speed shutter and variable iris was placed between the pyrometer and blackbody to ensure the the calcium fluoride rod did not sustain any thermal damage from prolonged exposure to the high temperatures of the blackbody calibrator.

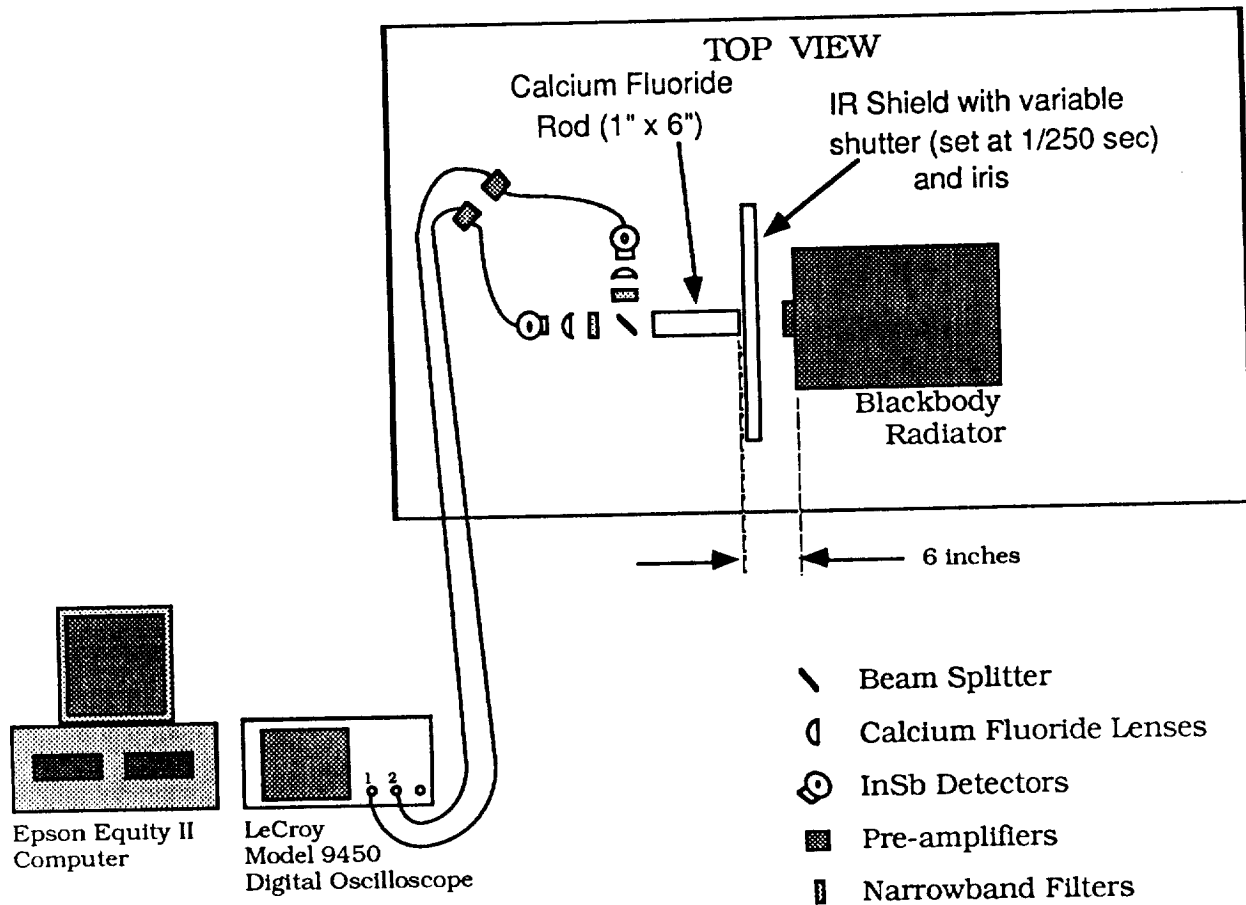


Figure 2.12
Laboratory Set-up

The Indium Antimonide (InSb) detectors were cooled with liquid nitrogen for 2 hours before beginning the experiment to ensure minimal drift of the detector offset voltage. With the blackbody calibrator set at 650° C and the shutter open, the heights and distances of all the components as well as the angle of the beam splitter were adjusted to allow for a maximum signal in both channels of the LeCroy digital oscilloscope. As the temperature of the blackbody calibrator was increased from 650° C to 1200° C at 50° C increments, the magnitude of the voltage of the detectors was recorded at each 50° C increment in temperature. For each data point, the shutter was opened for 4 ms, to simulate a molten particle dropping by the pyrometer. The initial detector offset, which is due to dark current in the detectors, was also recorded. The change in detector voltage was determined by subtracting the initial offset from the detector magnitude for each channel at different temperatures. The ratio of the change in detector voltage for each channel was then taken and plotted with respect to the corresponding temperature. The test was repeated three times. The resulting calibration curves are shown in Figure 2.13. A theoretical curve, calculated with a FORTRAN program {Appendix C} using Planck's Law and parameters (central wavelength, λ_0 , and half peak bandwidth) obtained from the filter transmittance curves, is shown along with the calibration curves. Each set of data, including the theoretical data, has an exponential curve fit to the data.

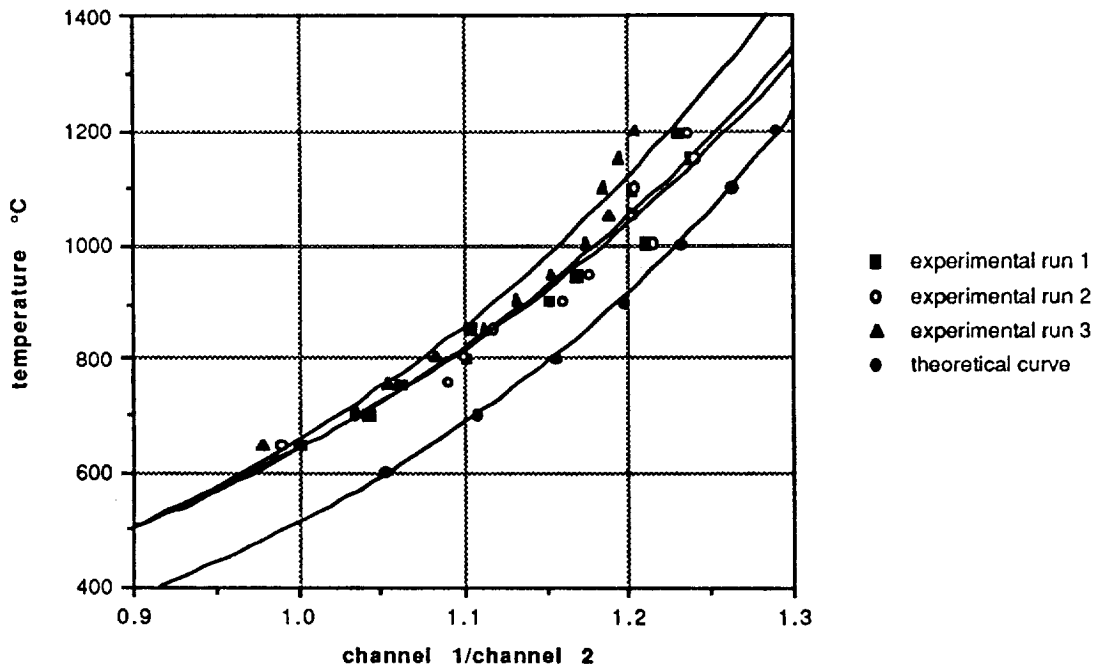


Figure 2.13
Pyrometer Calibration Results

The offset between the theoretical and experimental curves is probably due to the idealized filter parameters and component alignment in the pyrometer box.

2.3.3 Test of Effects of Iris Diameter

The set-up shown in Figure 2.12 was used to determine how the size of the molten particle to be evaluated would affect the performance of the pyrometer. The blackbody radiator was set to 1000° C. The diameter of the iris, measured by digital calipers, was varied from 2 mm to 13 mm in increments of 1 mm. The shutter was opened for 4 ms, and the change in detector voltage was recorded for both channels. The ratio of the change in detector voltage for each channel was the determined numerically. The results are shown in Figure 2.14. A plot of the signal-to-noise ratio (SNR) is also shown in Figure 2.15.

Because a variable iris in front of the blackbody aperture does not strictly model a small radiating particle, the results do not necessarily give a limitation on the size of the particle. The results do show, however, that as the size of the particle decreases, the performance of the pyrometer is adversely effected.

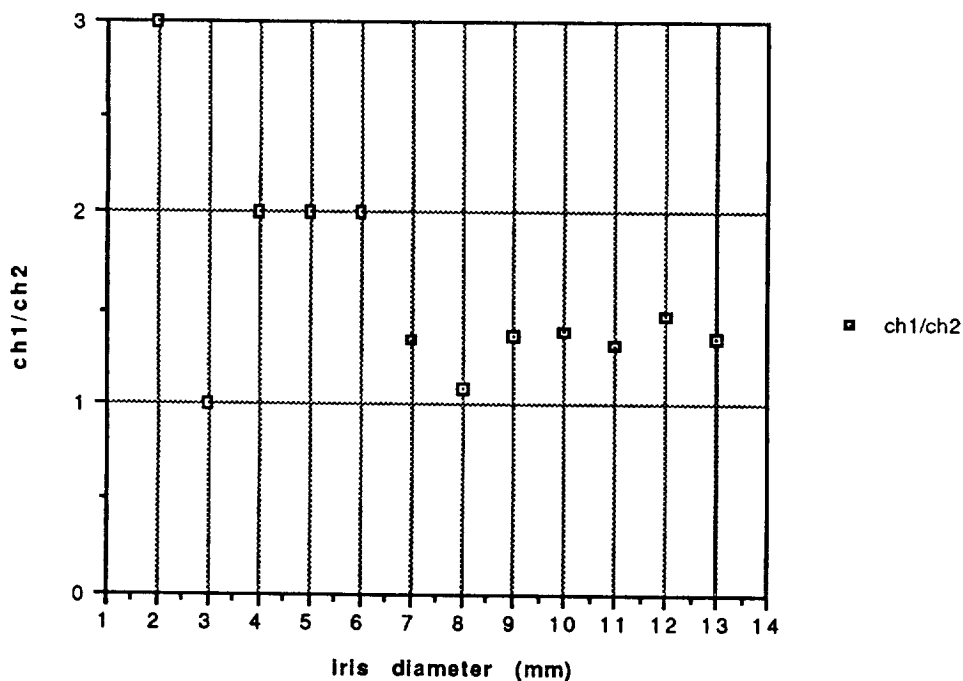


Figure 2.14
Effects of Iris Diameter

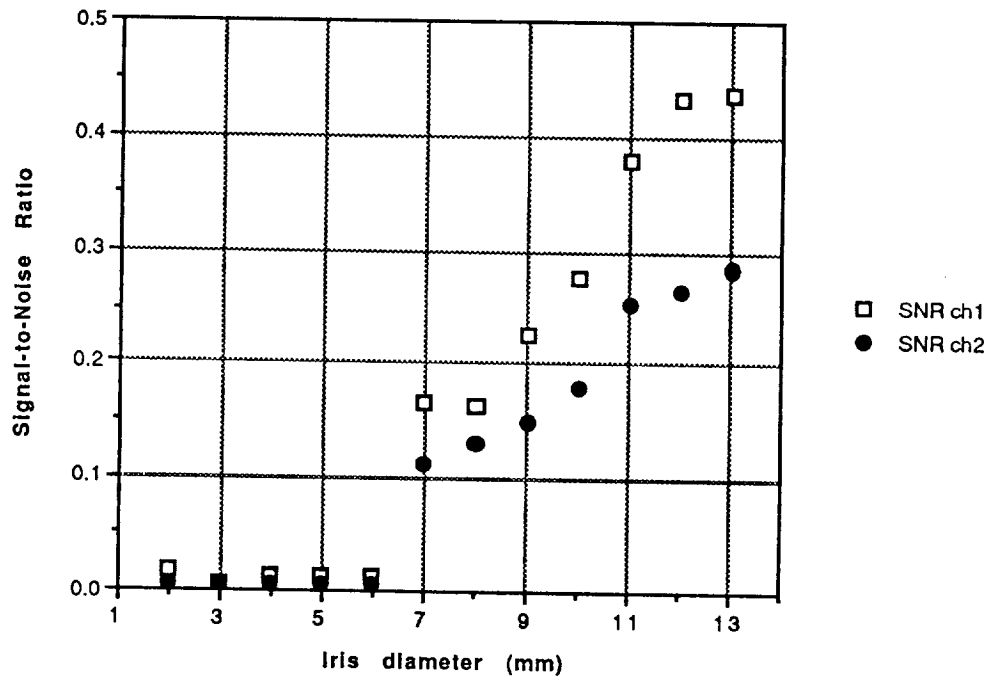


Figure 2.15
Effects of Iris Diameter on SNR

2.4 Field Tests of Prototype Pyrometer at NASA MSFC

During field tests of the pyrometer at Marshall Space Flight Center, niobium drops were processed. At the top of the drop tube, a niobium wire (62 mil diameter, MARZ grade) was fed into an electron-beam (EB) furnace. As the end of the wire was heated, the melted niobium formed a drop on the end of the wire. Once the size of the drop was large enough (5.485 to 5.543 mm in diameter), it broke away from the wire and began to fall down the tube. The size of the drop, which remains constant for a set diameter of niobium wire, is determined by the liquid-to-solid surface tension and the mass of the material. The particle cooled and solidified before hitting the bottom of the tube. The prototype pyrometer was set up to observe the niobium particles as they dropped down the tube.

2.4.1 Calibration

The prototype pyrometer was set-up and calibrated using the blackbody calibrator as in Figure 2.3.2. The signal in both channels of the digital oscilloscope was optimized at 650° C, by adjusting the heights and distances of the components. After this, data was taken at four different

temperatures to obtain a calibration curve for the experiments to follow. The calibration points, calculated from the data, are shown in Figure 2.16 with an exponential curve fitted to the data. Also shown is the theoretical curve for comparison.

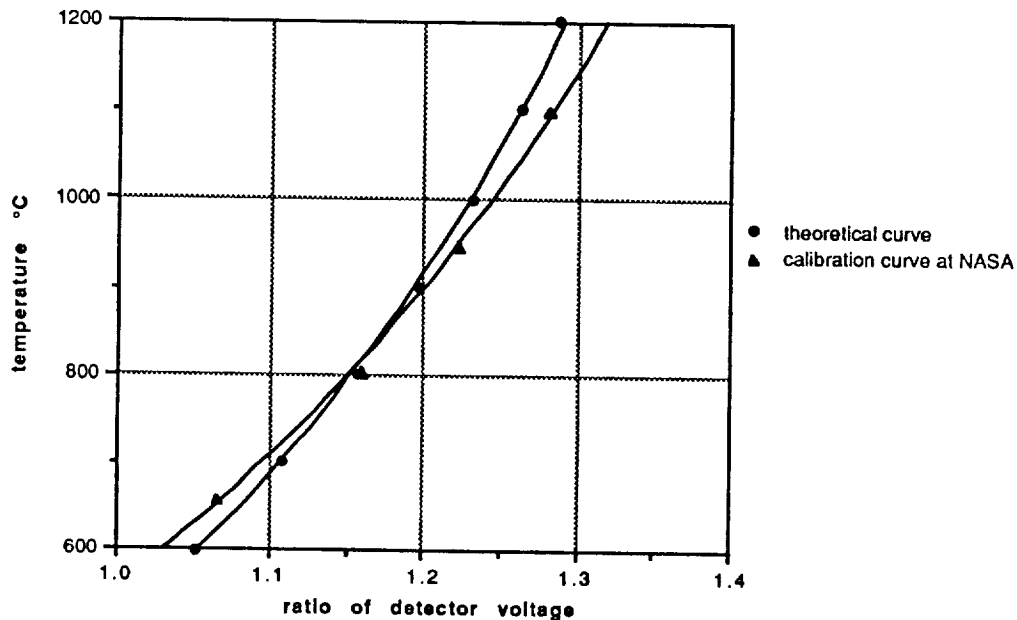


Figure 2.16
Calibration Curve at MSFC

2.4.2 Mounting Details

With all components properly mounted in the box, the pyrometer was moved to a port 22.6 meters below the E-beam furnace. The calcium fluoride rod was carefully fed through a 2 3/4" Conflat vacuum flange, making sure that none of the components in the pyrometer box were bumped and knocked out of alignment. A flat black stove-pipe section had been inserted at the 12th level port in order to decrease stray reflections from the drops on the tube. The stove pipe section was slightly skewed in the drop tube, thereby obstructing a small portion of the instrument port on the 12th floor.

Care was taken to minimize ground loops. The preamps of the pyrometer were attached to an instrument ground that was provided throughout the drop tube building. Once the pyrometer had been securely mounted to the drop tube, the drop tube was evacuated to approximately 10^{-6} torr.

2.4.3 Data Acquisition

A silica photodetector, located immediately below the drop tube furnace, was used as a trigger for the data acquisition. The data from the detector preamps was acquired by the digital processing

oscilloscope at a sampling rate of 10 kHz. A program (Appendix E) was written in order to transfer the data from the digital oscilloscope to a file on the hard drive of the computer. Backup copies of these files were also made on floppy disks. A plotter was used to copy data obtained on the digital oscilloscope.

2.4.4 Data Analysis

2.4.4.1 Processing of Original Data

A software package called MATLAB™ was used to determine the initial detector offset and the magnitude of the voltage when the particle was detected. MATLAB™ is an interactive software package for scientific and engineering numeric computation. Figure 2.17 shows a sample of the drop data obtained from the niobium processing.

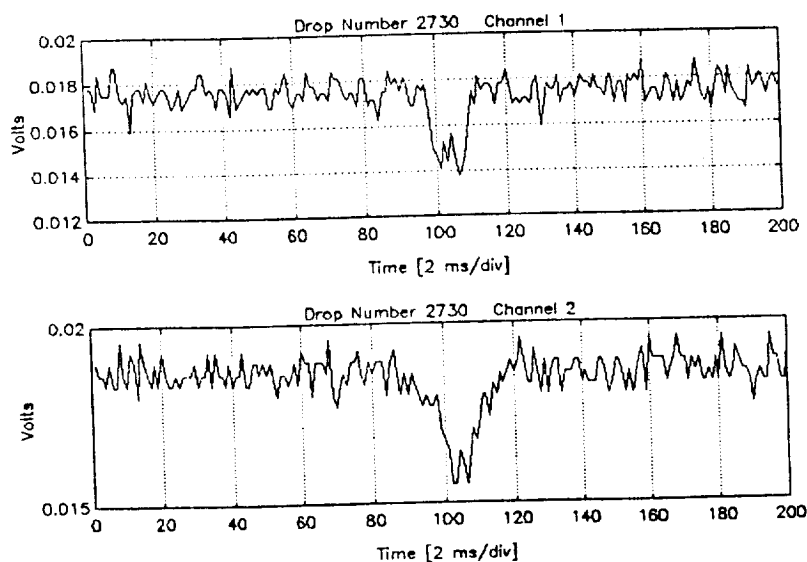


Figure 2.17
Data Obtained from Niobium Processing

MATLAB™ was used to determine the initial detector offset by having the software package determine the mean value of a specific number of points before the drop event occurred. In the data in Figure 2.17, the initial offset was determined by taking the mean of points 1 through 80 on the time axis. The magnitude of the voltage when the particle was detected was determined by the same method. Due to the noise present in the detected signal, determining a value for the magnitude of the voltage when the particle was present was difficult. Therefore, a digital filtering technique, discussed in the next section, was adopted. Table 2.4.1 shows the official drop number and the ratio of the channels for each drop detected.

Official Drop Number	2695	2730	2734	2735	2737	2738	2745	2747	2748	2752	2753	2757	2759	2760
Ratio	2.364	1.409	1.375	1.238	1.591	1.071	1.556	2.077	1.875	1.182	0.800	1.538	1.714	0.970

Table 2.2
Ratio of Unfiltered Data

2.4.4.2 Processing of Filtered Data

Due to high frequency noise present in the detector outputs, digital filtering techniques were investigated to reduce the influence of the noise. Figures 2.18.a and 2.18.b show the power spectral density of the noise floor for both detectors on channels 1 and 2 respectively, as calculated by a Fast Fourier Transform (FFT) routine.

Two types of low-pass digital filters were examined; these were the Butterworth filter and the Chebyshev filter. A Butterworth filter design possesses maximum flatness in the passband at the cost of less stopband attenuation. As the order, n , of the filter approaches infinity, the amplitude response of the Butterworth filter approaches an ideal lowpass filter characteristic; however, the filter delay also approaches infinity. A Chebyshev frequency-response characteristic possesses ripples, or increases and decreases in gain, within the passband while maximizing the attenuation

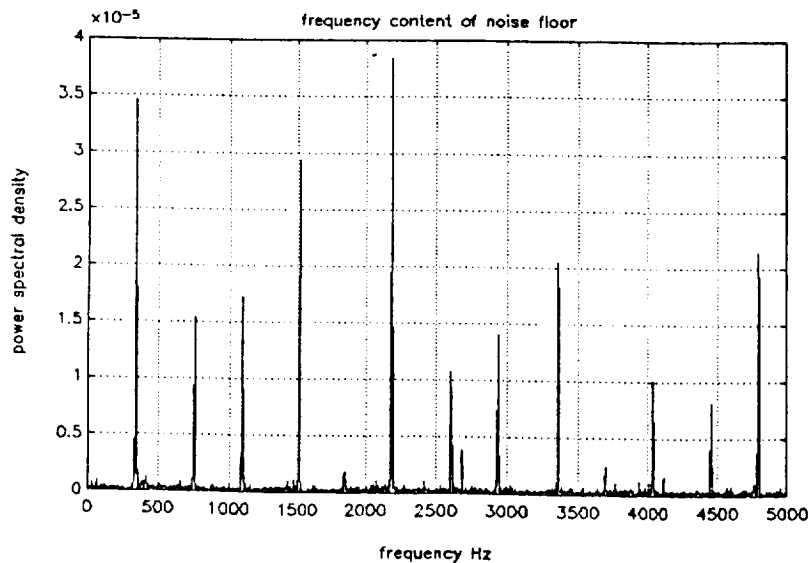


Figure 2.18.a
Power Spectral Density for Channel 1

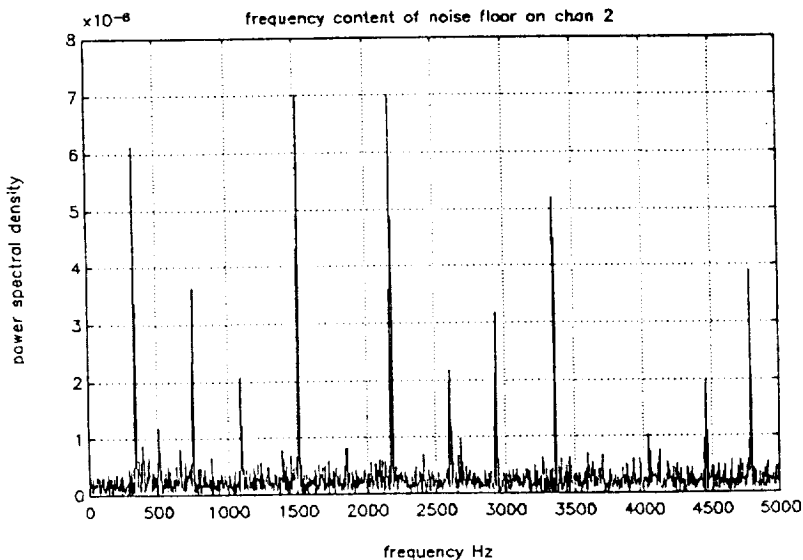


Figure 2.18.b
Power Spectral Density for Channel 2

in the stopband.^{8,9} Different orders of the filters were looked at as well as different cut-off frequencies. Plots of the data using cut-off frequencies from 200-600 Hz were examined. Cut-off frequencies of 300 Hz and lower washed out the signal obtained from the drop of niobium. Frequencies above 400 Hz did not significantly filter the noise within the signal. The cut-off frequency of 400 Hz was chosen because the noise component around 337 Hz only added a small ripple to the signal and did not appear to affect the signal detrimentally. The Butterworth filter was chosen as a better filtering technique for this application than the Chebyshev due to the ripple

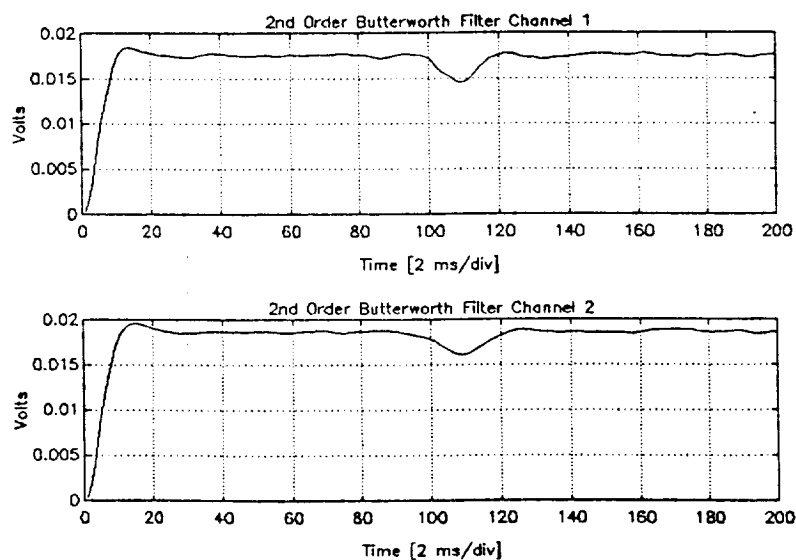


Figure 2.20
Butterworth Filters with cut-off @ 400 Hz

associated with the latter. The original data was filtered by different orders (1st through 4th) of the Butterworth filter. MATLAB™ was again used to determine the initial detector offset and the magnitude of the voltage when the particle was detected. In Figure 2.20 sample data from Figure 2.17 is shown filtered using a 2nd order Butterworth filter with a cut-off frequency of 400 Hz.

Table 2.2 below shows the the official drop number and the ratio of the channels for each drop detected using different order filters.

Official Drop Number	2695	2730	2734	2735	2737	2738	2745	2747	2748	2752	2753	2757	2759	2760	
Ratio	1st	1.500	1.160	1.300	1.143	1.240	0.562	1.333	1.667	1.462	1.172	1.133	1.200	1.318	1.226
	2nd	1.625	1.167	1.421	1.150	1.292	0.667	1.381	1.556	1.462	1.259	1.107	1.222	1.350	1.167
	3rd	1.625	1.125	1.500	1.100	1.304	0.647	1.450	1.556	1.462	1.269	1.107	1.222	1.300	1.207
	4th	1.588	1.160	1.474	1.143	1.320	0.667	1.409	1.667	1.429	1.241	1.133	1.200	1.429	1.226

Table 2.3
Ratio of Filtered Data

2.4.5 Experimental Results

2.4.5.1 Original Data

Figure 2.21 shows the ratios of the two channels from the original data. For all the drops detected, the ratios of the unfiltered detector voltages show a standard deviation of 0.432 and a mean of 1.483 for the ratio of the channels. According the calibration curve in Figure 2.16, the ratios of the drops indicate a range of temperatures from 400° C to well over 3500° C, and a mean temperature of 1800° C.

2.4.5.2 Filtered Data

Figure 2.22 shows the ratios of the two channels from the filtered data for each order of filter.

The ratios of the filtered data show a standard deviation of 0.24 and a mean value of 1.27 for the 14 drops analysed. The variance between the different order Butterworth filters was small, as can be seen from the figure above, but different means were obtained from that of the unfiltered data.

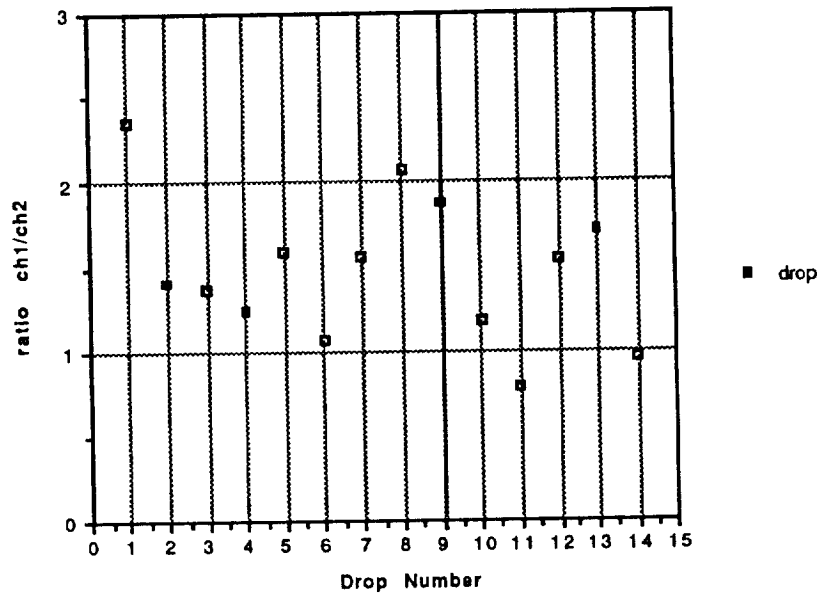


Figure 2.21
Ratio of Original Data

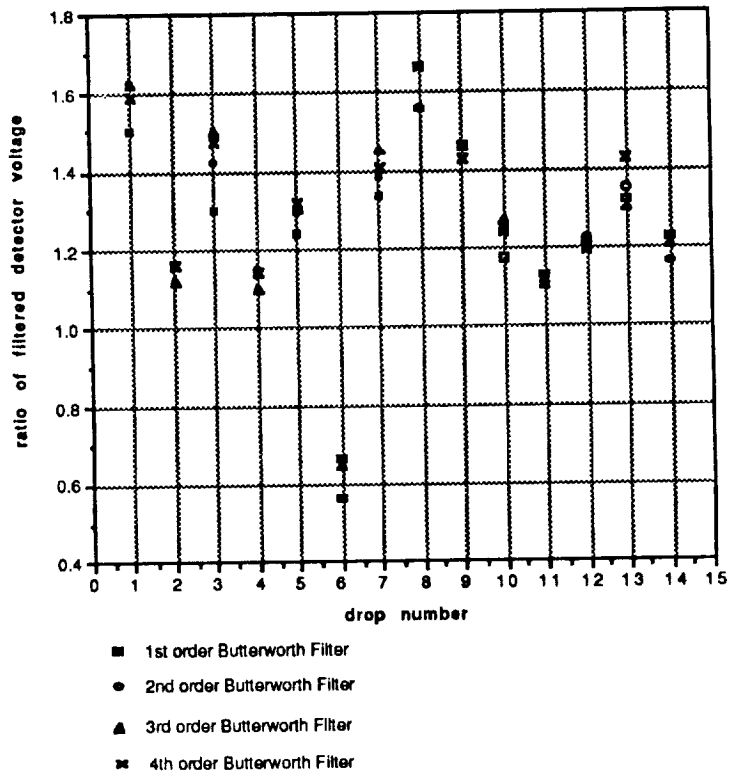


Figure 222
Ratio of Filtered Data

According to the calibration curve in Figure 2.16, the ratios of the drops, excluding the drop number 6 (2738), indicate a range of temperatures from 700° C to 2300° C, and a mean temperature of 1100° C.

2.5 Conclusions / Recommendations

Since the melting point of niobium is 2468° C, we should expect to see pellet temperatures below that at a port 22.6 meters below the furnace. This was not the case for the results obtained from the non-filtering approach. The use of digital low pass filters to analyse the data is a preferable approach because of the smaller variances between the drops than the unfiltered drops and the consistency between the different orders of the filtered data.

Although the variance in the filtered data was smaller than that of the unfiltered data, estimating the temperatures with the use of the calibration curve leads to a wide range of possible temperatures, from 700 ° C to 2300° C. This wide range of possible temperature values shows that the prototype pyrometer did not operate as anticipated. A possible explanation for the poor performance of the pyrometer is possibly the deviation of the molten particle from the center-line of the drop tube.

In some of the drops obtained at NASA, a signal was observed in only one of the two channels of the oscilloscope. The channel which did not record the signal from the drop varied with the drop. The oscilloscope was assumed to be working properly because signals were observed in both channels for most drops. These drops lead to an assumption that the power incident on each detector may be dependent on the angle of incidence of the drop on the rod looking into the tube. This angular dependence could also be the reason for the variance between the drops detected at the drop tube.

Future tests of this pyrometer design should investigate this possible angular dependence of the pyrometer. Suitable methods to eliminate or minimize this effect could also be investigated. Possible options could include physically narrowing the field-of-view (FOV) of the pyrometer, or more specifically, the calcium fluoride rod. This may be accomplished by masking the rod, possibly with photolithographic techniques, so that it only sees the drops which fall down the center-line of the tube. Another method of narrowing the FOV may be to recess the rod in the flange of the drop tube instead of allowing it to penetrate into the drop tube diameter.

3.0. Optical Fiber Holography

Optical fibers have been successfully employed as sensors for detection of a wide range of observables, such as strain, temperature, displacement, electric and magnetic fields, and acoustic fields. Due to their small size and flexibility, optical fibers configured as strain sensors show great promise for applications where they can be embedded in a host material. So configured, the fibers may be used to determine vibrational modes, acoustic emissions, integrated or localized strain, or temperature. Possible applications include sensing strain within structural members of the proposed space station and national aerospace plane.

Two approaches for strain sensing that have been extensively researched at Virginia Tech are mode-mode interference in few mode fibers¹⁰, and optical time domain reflectometry.¹¹ In this project, the principles of optical fiber-based holography have been applied to extend these results. Publications based on the results of this research are presented in Appendix F.

3.1. Holographic Matched Filters for Processing Modal Domain Sensor Outputs

Holographic matched filters were used to improve the processing of output signals from optical fiber strain sensors that utilize mode-mode interference in a few-mode fiber. The holographic filter approach should prove more rugged than alternative approaches since the matched filters lend themselves more easily to construction in a monolithic package.

Optical fiber sensors employing the interference between two or more propagating modes in a fiber have been termed "modal domain sensors." Typically the sensor fiber is operated in a wavelength regime where only a few modes propagate. By adjusting a coherent source of the proper wavelength to achieve the correct excitation conditions at the input of the fiber, the far-field output pattern exiting the fiber can be made to assume the form of a small number of intensity lobes that rotate or oscillate in a predictable fashion when the fiber is strained. For example, when a nominally single-mode circular-core fiber is injected with light of a wavelength shorter than the second mode (LP₁₁) cutoff wavelength, more than one mode may propagate. The wavelength and fiber parameters may be chosen such that only the first two linearly polarized modes LP₀₁ and LP₁₁ (including degeneracies) may propagate. This will occur if $2.405 < V < 3.832$, where V is a dimensionless propagation constant defined by

$$V = \frac{2\pi a}{\lambda} (n_1^2 - n_2^2)^{1/2} \quad (3.1)$$

where a is the core diameter, λ is the wavelength, n_1 is the core refractive index, and n_2 is the cladding refractive index. When an axial stress is applied to the fiber, strain will be imparted to the fiber, resulting in three changes: the fiber elongates, the refractive index of the fiber core changes

due to the elasto-optic effect, and the core diameter reduces slightly due to the Poisson effect. The last two effects change the propagation constants of the LP_{01} and LP_{11} modes differently, yielding a net change in the far-field intensity pattern. If, for example, only the LP_{01} and the even LP_{11} modes are excited at the input of the fiber, then the far-field pattern will assume the form of a two-lobed pattern (Figure 3.1), and the intensities of the two distinct lobes will alternate in an oscillatory manner with increasing strain. The modal domain sensor is therefore equivalent to a fiber optic differential interferometer, with both arms of the interferometer contained in a single fiber. The elimination of the need for couplers and a separate reference fiber renders the construction of the modal domain sensor simpler than the classic fiber optic Mach Zender interferometer. However, the differential detection inherent in the modal domain sensor results in a sensitivity three orders of magnitude less than that of the Mach Zender sensor.

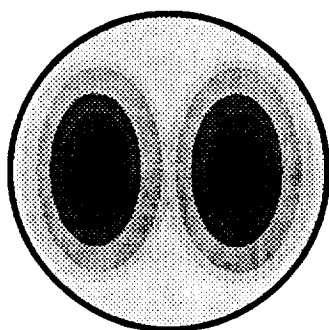


Figure 3.1.
Typical output farfield pattern for two-mode fiber

Techniques for processing the far-field output of a modal domain sensor include using a pin-hole aperture to sample the intensity distribution at a single point, and the use of a fiber optic bundle connected to a detector array.¹² With pinhole detection, a small aperture is used to sample the far-field pattern at a point as in Figure 3.2. A photodetector placed behind the aperture measures the

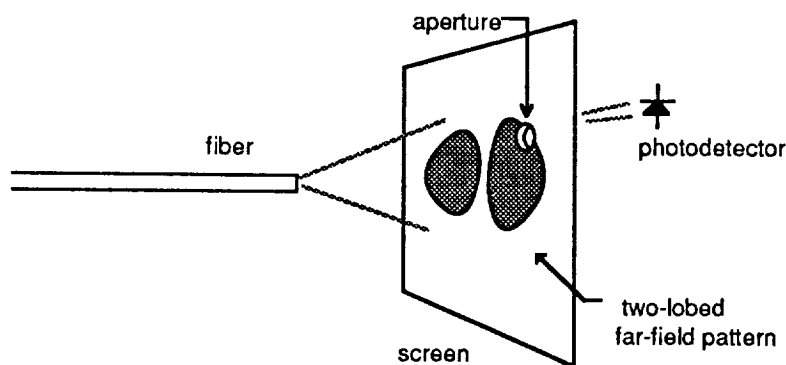


Figure 3.2.
Pin-hole processing of modal domain sensor output

intensity at that point. As the fiber is strained, the oscillation of the lobe intensity is converted to a changing electrical signal by the detector. In order to linearize the detector output and maximize the sensitivity, the aperture must be located at a position where it samples equal intensity in each lobe. This position defines the quadrature point of the lobe oscillations. With full-field processing, the entire far-field is sampled by a fiber bundle connected to a photodetector array. The output of the detector array is fed to a computer, which determines the centroid of each lobe. As the far-field pattern evolves with the application of strain to the sensor fiber, the strain can be calculated by tracking the change in the centroid location and magnitude.

A major disadvantage of the use of a fiber/detector array or camera for processing the sensor outputs is the slow speed of such a system. Detector arrays or CCD cameras must be read out serially to the computer, and after that the complexity of the required algorithms make it difficult for the sensor system to respond to high frequency perturbations in real time.

3.1.1. Holographic Matched Filters for Modal Domain Sensors

Holographically prepared optical matched filters have been used for pattern recognition and correlation¹³, but it is believed that the application described here is the first for processing of the output of an optical fiber sensor. In this use, the output of a coherent source is split by either a beamsplitter or a fiber optic coupler, with one output being injected into a single-mode reference fiber, and the other injected into a two-mode modal domain sensor fiber (Figure 3.3). The far-field

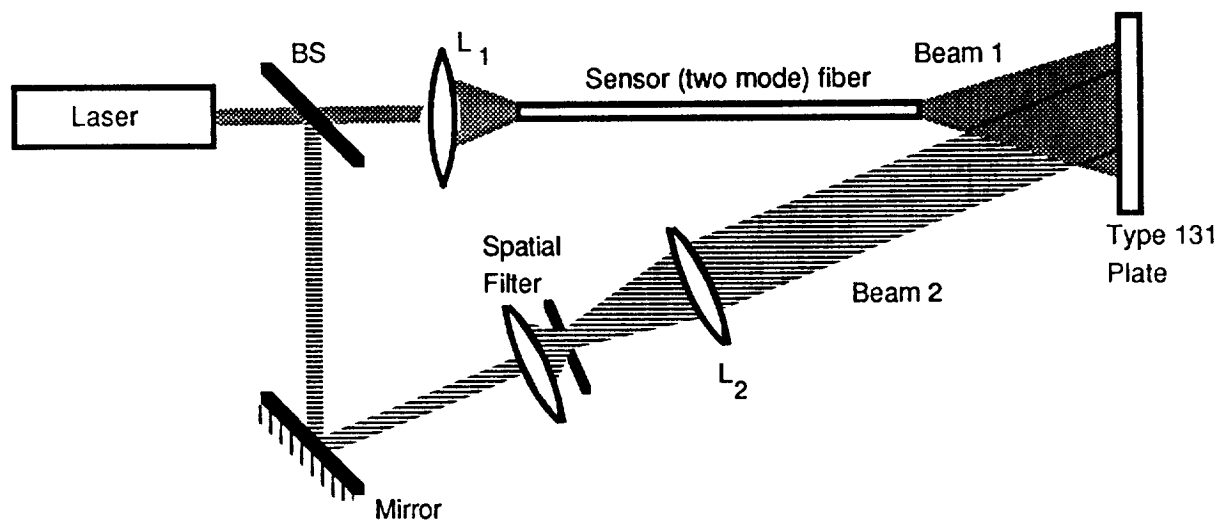


Figure 3.3.
Experimental set-up for writing matched filter

output from the two-mode sensor fiber is interfered at a holographic emulsion with the farfield output of the reference fiber. After development, the holographic emulsion becomes the matched filter. The filter is then placed in the same position, relative to the sensor fiber, and the reference fiber is removed. If the output of the sensor fiber then duplicates (correlates with) the farfield pattern used to write the filter, the light incident on the filter will be diffracted so as to reconstruct the previous reference beam. A lens may be used to collect this diffracted light and direct it to a photodetector (Figure 3.4). As the fiber is progressively perturbed, the far-field pattern will evolve, and the light detected by the photodetector will decrease, indicating a reduced correlation with the original, unperturbed pattern.

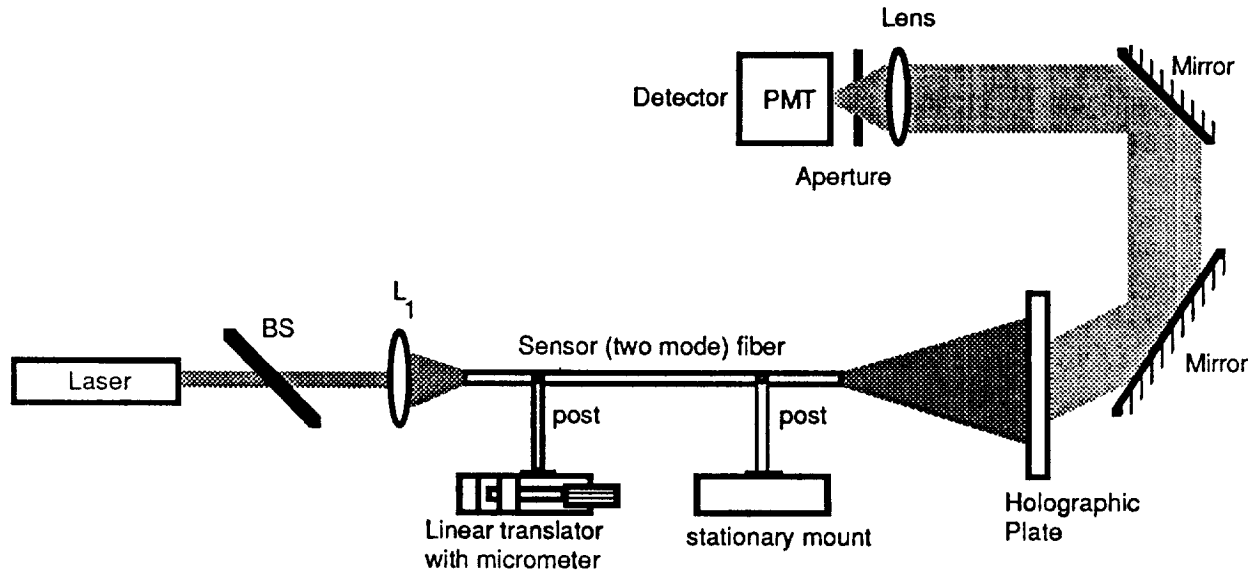


Figure 3.4.
Experimental set-up for processing sensor output with matched filter.

3.1.2. Theory

Let the electric field strength at the output end of the sensor fiber be denoted as $E_o(x,y)$, and the field at the reference fiber end be $R(x,y)$. The far-fields incident on the holographic film are related to the fiber outputs by the Fourier transforms of the outputs:

$$\begin{aligned} \mathfrak{F}\{E_o(x,y)\} &= E_o(\mu,\eta), \text{ and} \\ \mathfrak{F}\{R(x,y)\} &= R(\mu,\eta). \end{aligned} \quad (3.2)$$

Since the holographic film is a square law medium, the resulting filter amplitude transmittance will be given by

$$\tau(\mu,\eta) \propto [E_o(\mu,\eta) + R(\mu-\mu_o,\eta)]^2, \quad (3.3)$$

where the μ_o parameter indicates the angular offset of the incident reference wave with respect to the object (sensor fiber) wave, and where α indicates proportionality.

After development, the holographic filter is repositioned with the identical orientation with respect to the sensor fiber as when the filter was written. Thereafter, when the sensor fiber is strained or otherwise perturbed, the far-field incident on the filter will take the form $E_1(\mu,\eta)$, and the wave diffracted by the filter will be

$$C(\mu,\eta) = E_1(\mu,\eta) \tau(\mu,\eta) \alpha E_1(\mu,\eta) [E_o(\mu,\eta) + R(\mu - \mu_o, \eta)]^2. \quad (3.4)$$

The component that will be diffracted into an output wave in the same direction as the reference is the component given by

$$C_{\text{ref}}(\mu,\eta) = E_1(\mu,\eta) E_o^2(\mu,\eta) R^2(\mu - \mu_o, \eta) \quad (3.5)$$

It is this component that gives the correlation of the sensor signal output with the holographic filter function. A lens collects this component and focuses it onto a photodetector. This lens performs the inverse Fourier transform, so that the component incident on the photodetector is

$$C(x,y) = \mathfrak{F}^{-1}\{E_1(\mu,\eta) E_o^*(\mu,\eta) R(\mu - \mu_o, \eta)\} \\ \alpha \int E_1(x',y') E_o^*(x'-x, y'-y) dx' dy'. \quad (3.6)$$

Due to the small area of the photodetector, a small portion of this field is sampled, yielding

$$c_o = \left| \int E_1(x,y) E_o^*(x,y) dx dy \right|^2. \quad (3.7)$$

The magnitude of this correlation function depends on the similarity of the output of the perturbed fiber with the filter transmittance function that was formed with the output of the unperturbed fiber. As the fiber is further strained, the far-field continues to evolve, further decorrelating with the filter and yielding a further drop in output from the photodetector. In the case where the sensor fiber is a two-mode fiber, we can expect a cyclical output from the detector, since the two lobed output from such a fiber demonstrates a periodic cycling of power between the two lobes as the perturbation of the fiber is increased.

3.1.3. Experiment

To verify experimentally the concepts outlined above, a demonstration was assembled as shown in Figure 3.3. The output of a helium neon laser was divided by a 50/50 beamsplitter and one of the resulting beams was then focused into the sensor fiber, a polarization-preserving single mode fiber with a second mode cut-off wavelength of 850 nm. When operated at 633 nm, the sensor fiber supported propagation of the LP_{01} and LP_{11} linearly polarized modes. A portion of the sensor fiber was supported between two posts, one fixed, and the other capable of longitudinal movement by a linear translator. By measuring the movement of the translator and the separation of the posts, it was possible to calculate the strain imparted to the fiber. The output of this fiber was collimated by a 16 cm focal length lens and directed to the holographic film at normal incidence. The second beam was collimated and directed toward the holographic film at a 30° incidence from the normal, resulting in an interference region on the film of approximately 4 cm in diameter. The length of the sensor fiber was adjusted to equalize the optical path lengths in the object and reference beams. The film employed was a 2"x2" Kodak high speed type 131 plate. The plate was mounted on a two-axis micropositioner so that it could be accurately repositioned after development. An exposure of 1/50 second and processing in Kodak D-19 developer led to a diffraction efficiency of about 8%.

Before returning the developed plate to its position on the two-axis positioner, the output lens, photodetector, and aperture were put in place. To achieve this, the output of the sensor fiber was blocked, and the lens, aperture, and photodetector were placed as indicated in Figure 3.5. The component positions were then carefully positioned to maximize the output of the photodetector as the detector output was monitored. After development, the plate was returned to the two-axis positioner, and the reference beam was blocked and the sensor fiber output unblocked (Figure 3.4). The position was adjusted to maximize the light detected by the photodetector.

The sensor fiber was then strained by using the translator to increase the separation between the supporting posts. The fiber strain for each increment of post separation was calculated and the detector output at that strain was recorded. The results are illustrated in Figure 3.6. As expected, the periodic exchange of output power between the two lobes of the sensor fiber far-field result in a sinusoidal variation in detector output. The decreasing maxima exhibited in the detector output may be due to mode coupling effects. The effect that a maximum does not exist at the point of zero strain is likely due to the difficulty in accurately repositioning the plate after developing. The deviation from exact periodicity is the result of loose tolerances in the translator that was used to apply strain to the fiber.

The experiment was duplicated with a pinhole substituting for the matched filter, as explained in Section 3.1. The results of the experiment with pinhole detection are shown in Figure 3.7. The data is arbitrarily scaled vertically to facilitate comparison.

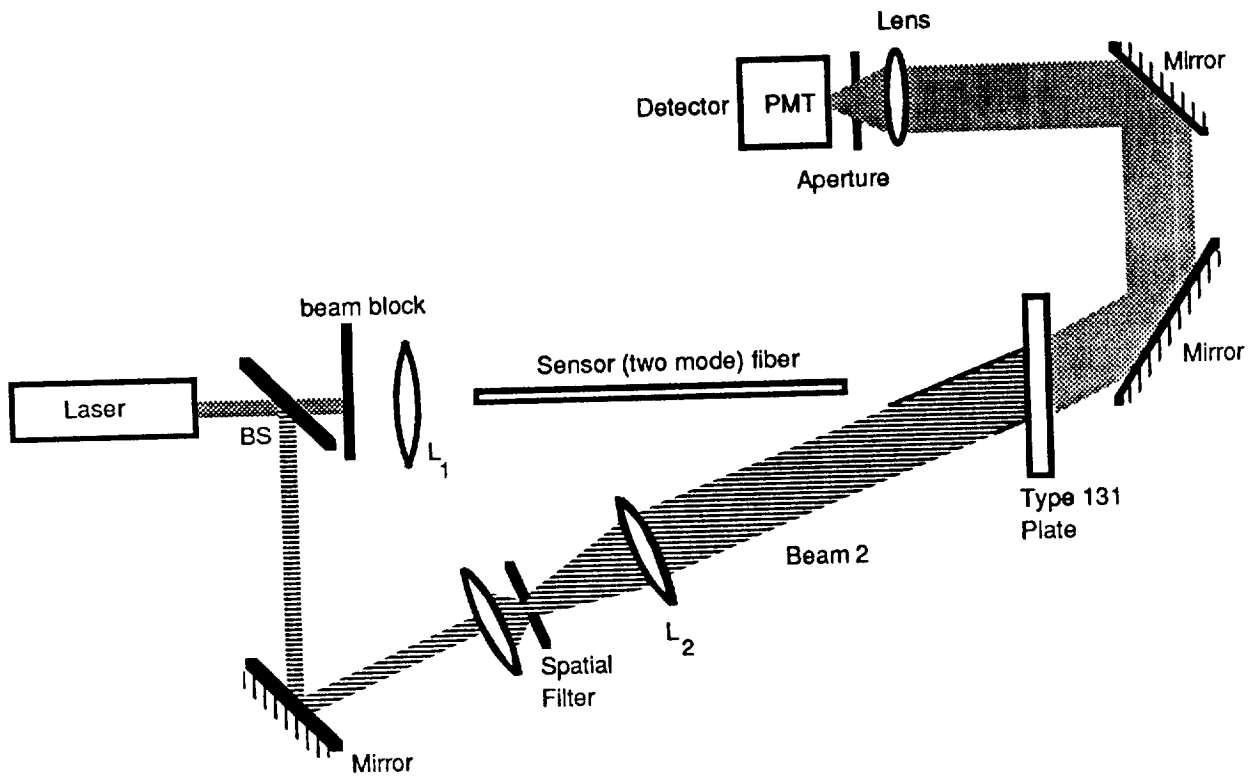


Figure 3.5
Alignment of mirrors and detector.

3.1.4. Experimental Results for Matched Filter Holography

The data in Figure 3.6 illustrates graphically the feasibility of the use of holographic matched filters for processing the output of modal domain sensors. Comparison with the output of a pinhole-processed sensor graphed in Figure 3.7 indicates that the matched filter processing yields very similar results. However, the matched filter approach offers several advantages. First, the matched filter may be easily assembled into a ruggedized, compact in-line configuration by using gradient index lenses (GRIN) rather than conventional bulk optical components. In addition, the filter may be matched to any arbitrary fiber output and is not restricted to use with two-moded fiber. In fact, preliminary experiments directed at the use of multimode fiber as a sensor fiber indicate that it is much more sensitive to strain than the two-mode fiber, and the filter-processed response does not exhibit periodic behavior. This result suggests that it may be possible to tailor the sensitivity of the system by adjusting fiber parameters to change the number of modes propagated by the fiber. Finally, by using real-time holographic materials it may be possible to realize adaptive filters with responses that may be changed dynamically.

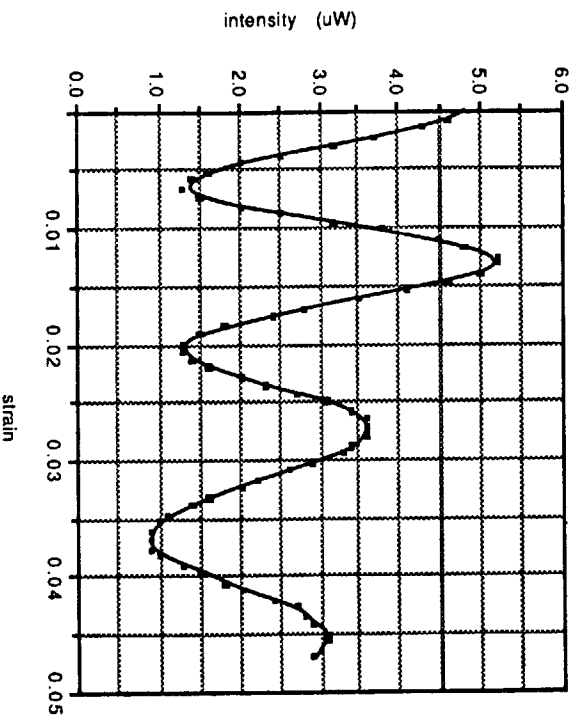


Figure 3.6. Output of matched-filter processed sensor.

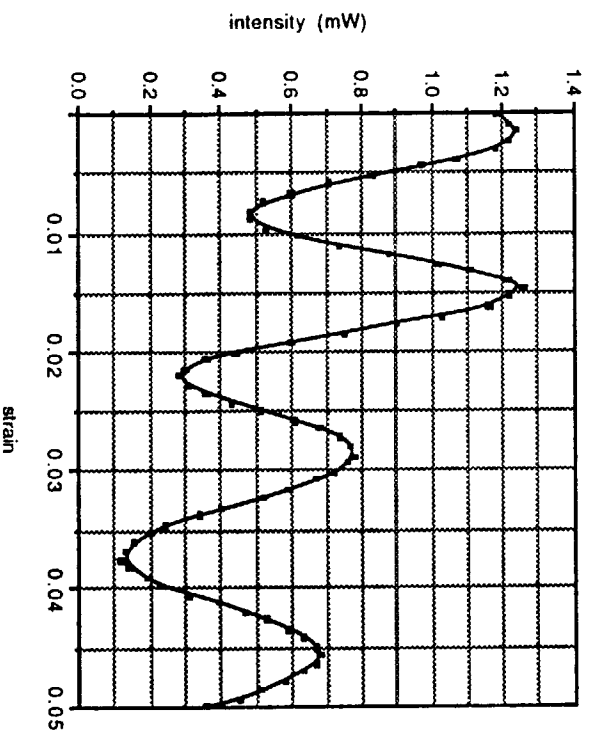


Figure 3.7. Output of pinhole aperture sampled sensor

3.2 Evanescent Wave Holography

Optical fibers have been used for holography in a variety of ways. Optical fibers have been used to transmit holographic images for recording and analysis at locations remote from an actual test object.^{14,15,16} Single mode fibers have been utilized as illuminators for holographic interferometry.^{17,14,18} Fiber bundles and large diameter individual fibers have been used as flexible illuminators for pulsed laser holography.^{19,20,21,22} Individual fibers and coherent fiber bundles have also been used in local and remote holographic systems including double exposure,^{23,24,13,14} time average,²⁵ and real time systems.^{26,27,28}

A number of previous efforts have been directed towards producing gratings in or along optical waveguides. Photosensitivity of a germanium-doped core has been exploited to form longitudinal Bragg reflection gratings.²⁹ A photoresist grating placed in the evanescent field region near the core of a side-polished fiber has been the key element of a proposed single mode optical fiber spectrometer.³⁰ A technique using photoresist has been used to fabricate surface-relief gratings for narrow band filtering in optical fibers.³¹ A similar concept has been reported where ultraviolet light has been used to write a phase grating along the core of an optical fiber.³²

This project researched the development of holograms which are recorded in a layer of holographic storage material coated in the cladding area of an optical fiber. The fiber cladding is ground down to an extent that the evanescent field of the fiber comes in contact with the holographic storage material. The evanescent field (U_e) is used as both the reference wave for recording and the read-out wave for recording and the reconstruction of the hologram. To make the hologram, the evanescent field is superimposed on an object wavefield (U_o) to form an interference pattern. The interference pattern is recorded in a very narrow region in the holographic storage material. The penetration depth of the evanescent wave thus determines the thickness of the hologram. The hologram exhibits a grating-type structure due to the nature of the interference phenomena. Similar waveguide holograms have been investigated in planar optical wave guides and a thorough theoretical treatment has been given.³³

All the papers involving holography and waveguides together have been restricted to experimental or theoretical investigations of grating type holograms along planar waveguides. To our knowledge this research is the first attempt to implement the expertise gained by working with waveguides and holographic storage materials, such as dichromated gelatin (DCG), to optical fibers. As mentioned before, work has been done with photoresist and etching techniques but no experiments with holographic storage materials, in or along optical fibers, has been reported. It is the primary attempt of this research to demonstrate experimentally the feasibility of developing a grating hologram in the cladding region of an optical fiber. Holograms of this type may turn out to be extremely useful as will be discussed in the next section.

3.2.1 Principles of Evanescent Wave Holography with Optical Fibers

The basic underlying idea of evanescent wave holography with optical fibers is to use an evanescent wave as the reference and read-out wave. The field distribution of a lightwave propagating in an optical fiber is periodic inside the core and evanescent outside of this region. The degree to which the field extends outside the core is typically on the order of a fraction of the wavelength and greatly depends on the order of the mode (higher order modes penetrating further outside). Due to the small penetration depths, the core region and the hologram storage material must be in direct optical contact. The refractive indices must also fulfill the condition for total internal reflection:

$$n_{\text{core}} > n_{\text{storage}}. \quad (3.8)$$

Figure 3.8 schematically shows the recording of the hologram in an optical fiber.

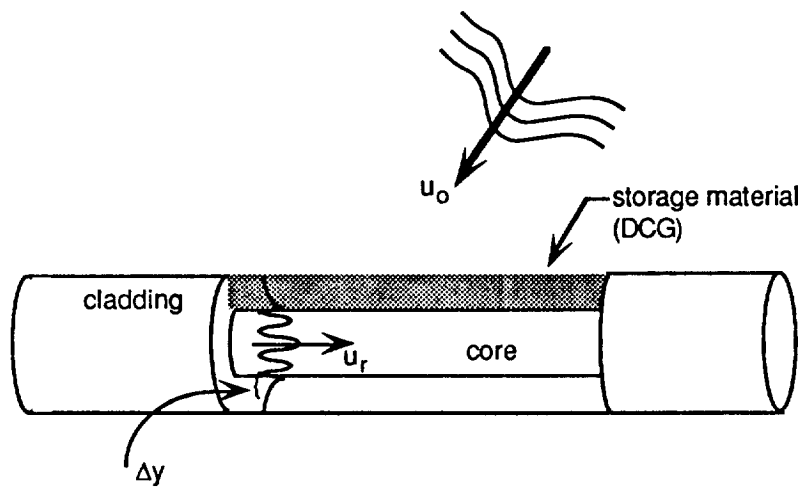


Figure 3.8
Recording of evanescent wave hologram in optical fiber.

The field distribution of a guided mode is considered. Its evanescent part in the core is the reference wave U_r . The object field U_o interferes with U_r and this interference is recorded. The thickness of the actual hologram is thus given by the penetration depth D_y and not by the core diameter. The storage material must hence be able to sustain volume holograms and not surface relief holograms, since the latter would require a storage material thickness which is small compared to the penetration depth of the evanescent wave. The theory developed here describes volume holograms made with evanescent waves.

The refractive index of the storage material must also be capable of a high modulation index since the effective thickness of the hologram is determined by the penetration depth of the evanescent

wave. If a storage material with a weak modulation of the refractive index is used, we must compensate for this by making the recording layer thicker. This would be useless due to the limited penetration depth of the evanescent wave, and thus high modulation of the refractive index is desired. It is for this fundamental reason that dichromated gelatin is chosen as the storage medium compared to other materials (such as photoresist) which have been used before.

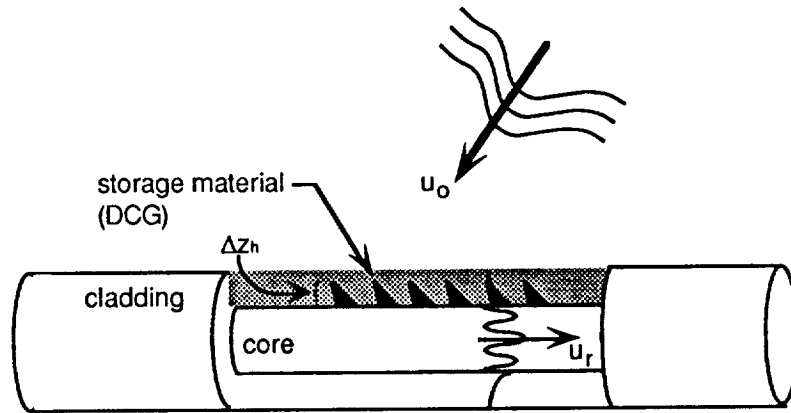


Figure 3.9. Refractive index variation of hologram in DCG.

Using a plane wave as the object wave will result in a hologram structure of regular periodic shape. The assumption is that the interference of U_o and U_r in the storage material will produce a proportional variation of the index of refraction which is periodic along the fiber, and periodic but multiplied by an exponential decay transverse to the fiber. The following figure shows this schematically.

The slanted lines extending a distance Z_H into the storage material indicate loci of constant refractive index. The distance Z_H is very small and due to the slanting of the lines of equal refractive index, the hologram is comparable to a blazed surface relief grating. The following figure shows the reconstruction of the hologram.

The guided read-out wave U_r is propagating in the same direction as did the reference wave during recording. This is diffracted by the hologram structure and reconstructs the object field U_o . In addition to U_o , a second weaker field U_o' is generated which is a mirror image of U_o with respect to the $y = 0$ plane. The condition for reconstructing the object wave exactly is that the read-out wave be identical to the reference wave. In other words the read-out and reference waves must have the same wavelengths and mode numbers for exact reconstruction of the object wave. The mirrored field U_o is generated by the diffraction of the read-out wave by the hologram and is not a reflection of any type from the boundaries. Reflection of the object field U_o does take place and only contributes to the intensity of U_o . In principle, reconstruction is also possible by any of the following methods shown here schematically in the following Figures 3.11 through 3.13.

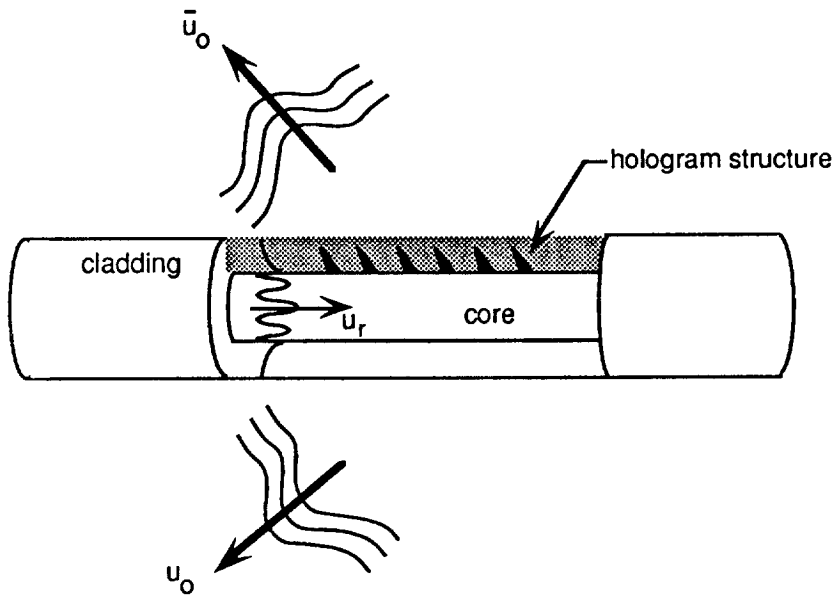


Figure 3.10
Reconstruction of the hologram.

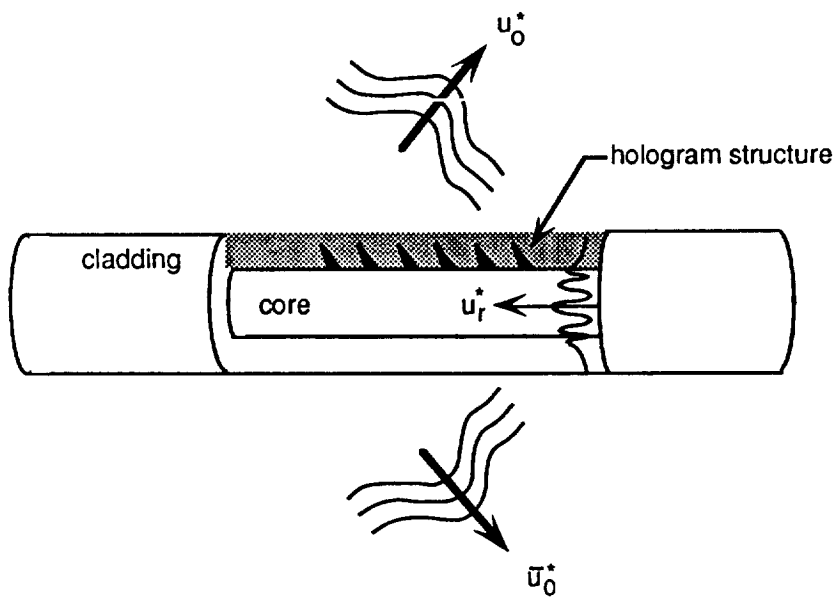


Figure 3.11.
Illumination with the conjugate reference wave U_r^* resulting in the conjugate object wave U_o^* .
 U_r^* essentially has the same mode number as U_r except that it is traveling in the opposite direction.

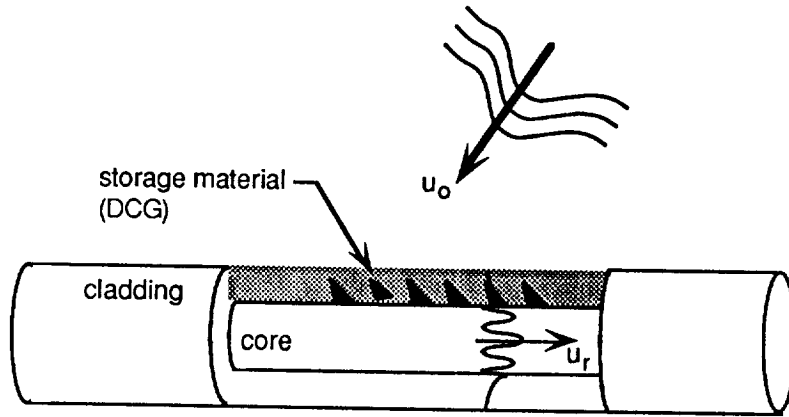


Figure 3.12.

Illumination with the object wavefield U_o resulting in the guided wave U_r . This case is of importance especially if the object wavefield is a laser beam (i.e. laterally limited plane wave) in which case we have a type of grating coupler.

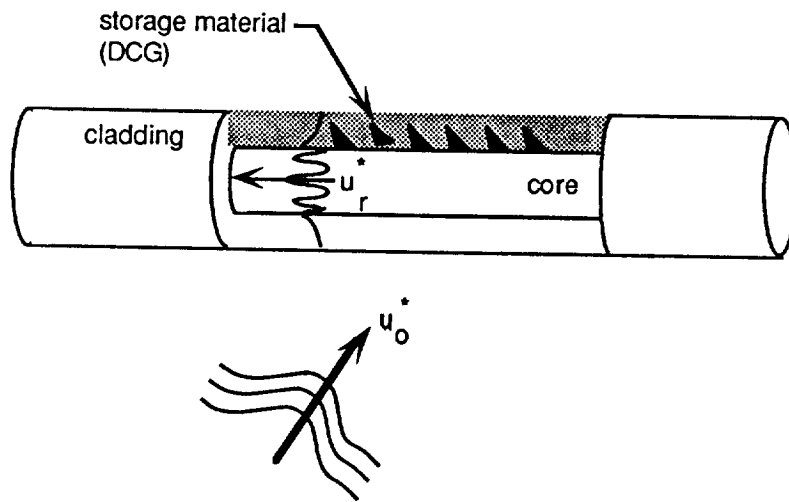


Figure 3.13.

Illumination with the conjugate object wavefield resulting in the conjugate reference wave U_r^* . Again we have a type of grating coupler as in the previous figure.

3.2.2 Theory

The theory presented in this chapter describes holograms with a plane wave as the object wave and a guided wave inside the optical fiber as the reference wave. The theory is totally adapted and extracted from reference 31 and is presented here with the particular case of evanescent wave holography with optical fibers in mind. The recording of the hologram is discussed first and the reconstruction process is presented. A brief discussion on diffraction efficiencies is also given. Table 3.1 is presented to clarify the symbols and notations used in the following discussion

U_e	evanescent wave
U_p	plane wave
n	refractive index of recording medium
n'	refractive index of surrounding medium
z_0	thickness of recording medium
U_c'	illuminating wave
U_d'	diffracted wave

Table 3.1 Symbol notation

Note that waves with a "prime" are outside the recording medium and "unprimed" waves are inside the medium.

3.2.2.1. Recording of the Hologram

The recording of the hologram is schematically shown in Figure 3.14. In that figure, U_e' is the ray that exceeds the critical angle within the core region and creates the evanescent wave U_e inside the recording medium. U_p' is the plane wave incident upon the recording medium and U_p is the transmitted part with the recording medium, which interferes with U_e .

Assuming TE-polarized vectors we have:

$$\begin{aligned}
 E_y(x,z) &= u(x,z); \\
 E_x &= E_z = 0; \quad H_y = 0; \\
 H_x(x,z) &= -\frac{1}{j\omega\mu_0} \frac{\partial U}{\partial z}; \text{ and} \\
 H_z(x,z) &= -\frac{1}{j\omega\mu_0} \frac{\partial U}{\partial x}. \tag{3.9}
 \end{aligned}$$

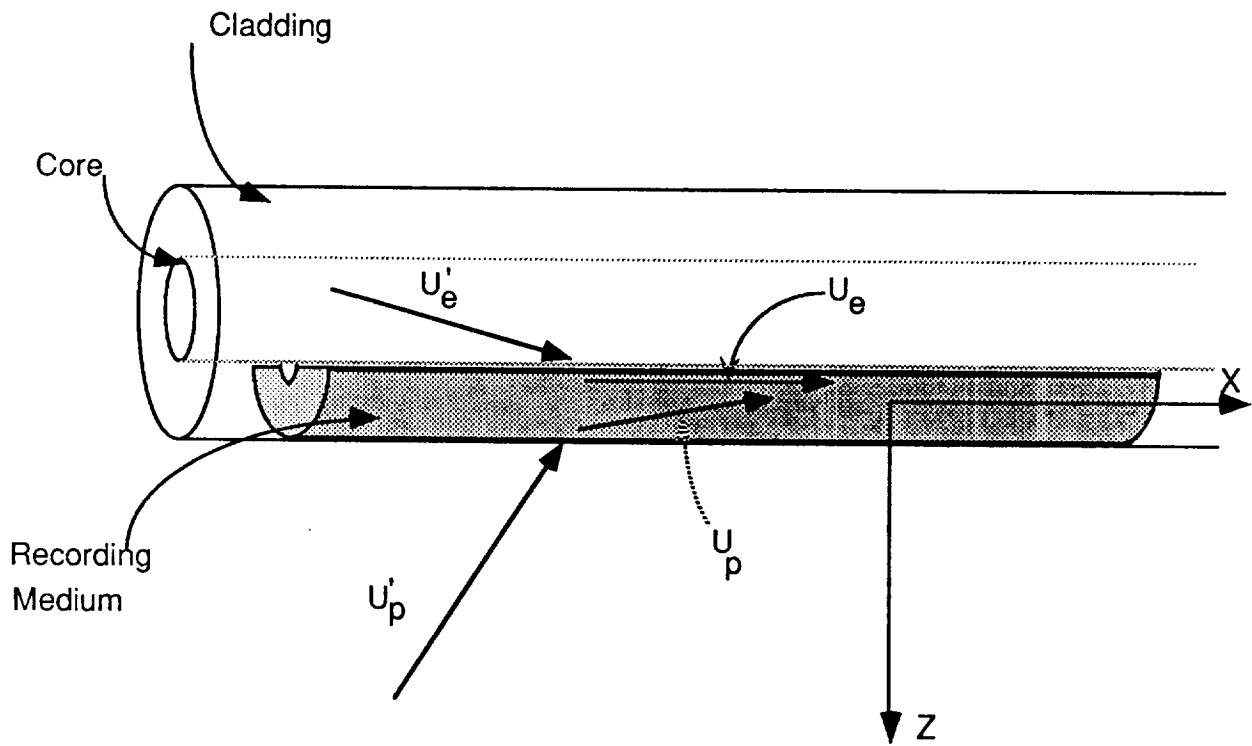


Figure 3.14.
Definition of beams employed in recording and reconstruction.

The time dependence $\exp(-j\omega t)$ is omitted and all fields are assumed periodic with angular frequency ω . In the recording medium we have

$$\begin{aligned} U_e(x,z) &= U_e \exp[j(k_{ex}x + k_{ez}z)] \\ &= U_e \exp[jk_{ex}x] \exp[-k_{ez}z], \end{aligned} \quad (3.10)$$

where

$$k_{ex} > k, \text{ and}$$

$$k_{ez} = j[(k_{ex})^2 - k^2]^{1/2}. \quad (3.11)$$

Also,

$$U_p(x,z) = U_p \exp[j(k_{px}x + k_{pz}z)] \quad (3.12)$$

with

$$k_{pz} = [k - (k_{px})^2]^{1/2} \quad (3.13)$$

The amplitudes U_e and U_p in the recording medium can be obtained from U_e' , and U_p' , respectively, with the Fresnel transmission coefficients:

$$\frac{U'}{U} = t_s = \frac{2k_z}{(k_z + k_z')} \quad (3.14)$$

where

$$r_s = t_s - 1. \quad (3.15)$$

The intensity is defined as

$$I(x,z) = \langle E^2(x,t) \rangle = \frac{1}{2} U^*(x,z) U(x,z) \quad (3.16)$$

Then the intensity of the interference between U_e and U_p is

$$\begin{aligned} I(x,z) &= \frac{1}{2} [u_p(x,z) + u_e(x,z)]^* [u_p(x,z) + u_e(x,z)] \\ &= \frac{1}{2} \{ U_p^2 \exp [j(k_{pz} - k_{pz}^*) z] + U_e^2 \exp (-2k_{ez}z) \\ &\quad + U_e^* U_p \exp [j(k_{ex} - k_{ex}) x + (k_{pz} - k_{ez}^*) z] \\ &\quad + U_e U_p^* \exp [j(k_{ex} - k_{px}) x + (k_{ez} - k_{pz}^*) z] \} \end{aligned} \quad (3.17)$$

For our case where U_p is a plane wave, (that is, k_{pz} is real), this expression reduces to

$$\begin{aligned} I(x,z) &= \frac{1}{2} \{ U_p^2 + U_e^2 \exp (-2k_{ez}z) \\ &\quad + 2\text{Re} \{ U_e^* U_p \exp [j(k_{px} - k_{ex}) x + k_{pz}z] \} \exp (-k_{ez}z) \} \end{aligned} \quad (3.18)$$

Inspection of equation 3.18 shows that an identical intensity distribution would result if the waves $U_e^*(x,z)$ and $U_p^*(x,z)$ interfere instead of $U_e(x,z)$ and $U_p(x,z)$. Complex conjugation is equivalent to the time-reversal transformation t to $-t$. The waves U_e^* and U_p^* can then be understood as U_e and U_p respectively, traveling in the opposite direction.

In the theory presented until now, no consequential assumption has been made. Now the assumption is made that the photosensitive or recording medium is homogeneous and weakly absorbing and equation 3.18 is a fairly good approximation to the intensity distribution. Furthermore, the response of the recording medium to this intensity distribution is that the dielectric constant ϵ is a linear function of the local intensity. More specifically,

$$\epsilon(x,z) = f[I(x,z)\tau] \quad (3.19)$$

where τ is the exposure time. The recorded hologram is therefore a dielectric grating with

$$\epsilon(x,z) = \bar{\epsilon} + \delta\epsilon(x,z) \quad (3.20)$$

where $\bar{\epsilon}$ is the mean dielectric constant of the hologram, and

$$\begin{aligned} \delta\epsilon(x,z) = \frac{1}{2} \frac{d\epsilon}{dI} \{ & U_e^* U_p \exp \left(j[(k_{px} - k_{ex})x + (k_{pz} - k_{ez}^*)z] \right) \\ & + U_e U_p^* \left(j[(k_{ex} - k_{px})x + (k_{ez} - k_{pz}^*)z] \right) \} \end{aligned} \quad (3.21)$$

which is the spatial variation of ϵ due to the interference.

Since a linear function $f(I(x,z))$ was assumed, $\delta\epsilon(x,z)$ can be thought of having two separate interference terms, as given by

$$\delta\epsilon(x,z) = \delta\epsilon_1(x,z) + \delta\epsilon_2(x,z), \quad (3.22)$$

where

$$\delta\epsilon_1(x,z) = \frac{1}{2} \left(\frac{d\epsilon}{dI} \right) U_e^* U_p \exp \left(j[(k_{px} - k_{ex})x + (k_{pz} - k_{ez}^*)z] \right) \quad (3.23)$$

and

$$\delta\epsilon_2(x,z) = \frac{1}{2} \left(\frac{d\epsilon}{dI} \right) U_e U_p^* \exp \left(j[(k_{ex} - k_{px})x + (k_{ez} - k_{pz}^*)z] \right). \quad (3.24)$$

The significance of this shall become clear later.

It should be noted that the interference fringes are periodic in the x -direction and multiplied by an exponential decay in the z -direction. The fringes are slanted with an angle φ given by

$$\tan \varphi = \frac{k_{pz}}{(k_{ex} - k_{px})} \quad (3.25)$$

3.2.2.2. Reconstruction of the hologram

Reconstruction of the hologram can, in principal, be accomplished in different configurations as explained in Section 3.2.1. Here it is assumed that the hologram is illuminated with a TE-polarized plane wave U_c' where the frequency may be different from the frequency used upon recording of the hologram.

$$U_c'(x,z) = U_c' \exp \left[j(k'_{cx}x + k'_{cz}z) \right] \quad (3.26)$$

where

$$k'_{cx} = \bar{k} \sin \alpha_c, \text{ and } \bar{k} = \bar{n} \frac{\omega_c}{c}, \quad (3.27)$$

with

α_c = incident angle

\bar{n} = mean refractive index of surrounding medium.

The time dependence $\exp(-j\omega_c t)$ is again omitted. The total field inside the hologram can be represented as

$$U(x,z) = U_c(x,z) + U_d(x,z) \quad (3.28)$$

with

$$\begin{aligned} U_c(x,z) &= \text{illuminating wave, and} \\ U_d(x,z) &= \text{diffracted wave.} \end{aligned}$$

By solving

$$\left[\frac{\partial^2}{\partial x^2} + \frac{\partial^2}{\partial z^2} + \left(\frac{\omega_c}{c} \right)^2 \epsilon(x,z) \right] U(x,z) = 0 \quad (3.29)$$

we find that

$$U_c(x,z) = U_c \exp [j(k_{cx}x + k_{cz}z)] \quad (3.30)$$

with

$$k'_{cx} = k_{cx}$$

and

$$k_{cz} = \begin{cases} -[\bar{k}^2 - (k_{cx})^2]^{1/2} \\ j[(k_{cx})^2 - \bar{k}^2]. \end{cases} \quad (3.31a)$$

$$(3.31b)$$

Equation 3.31a describes the reconstruction of the form indicated in Figures 3.10 and 3.11.

Equation 3.31b describes the reconstruction of the form indicated in Figures 3.12 and 3.13.

Solving for U_d , the assumption is made that the penetration depth of the evanescent wave is much larger than the thickness of the recording medium, Z_0 . The wavelets scattered by each volume element of the hologram are calculated using a Green's function and integrated over the volume of the hologram. U_d is found to have two components:

$$U_d(x,z) = U_d(x,z=0) + U_d(x,z=z_0) \quad (3.32)$$

where

$$U_d(x,z=0) = \left(\frac{\omega_c}{2c} \right) \frac{d\epsilon}{dI} \frac{U_c U_e^* U_p \exp(jk_x x)}{k_z (k_z + k_{cz} + k_{pz} - k_{ez}^*)} \quad (3.33)$$

and

$$U_d(x,z=z_0) = \left(\frac{\omega_c}{2c} \right) \frac{d\epsilon}{dI} \frac{U_c U_e^* U_p \exp[j(k_x x + k_z z_0)]}{k_z (-k_z + k_{cz} + k_{pz} - k_{ez}^*)} \quad (3.34)$$

with

$$k_x = k_{cx} + k_{px} - k_{ex}. \quad (3.35)$$

The physical interpretation of this result is that upon reconstruction of the hologram, two diffracted waves are generated. One is radiated toward the boundary $z = z_0$ and the other is radiated toward

the boundary $z = 0$. These are denoted U_d^+ and U_d^- , respectively, with $k_{dx}^+ = k_{dx} = k_x$ and

$$k_{dz}^+ = -k_{dz}^- = \begin{cases} [\bar{k}^2 - (k_{dx})^2]^{1/2} & \text{if } |k_{dx}| \leq \bar{k} \\ j[(k_{dx})^2 - \bar{k}^2] & \text{if } |k_{dx}| > \bar{k} \end{cases} \quad (3.36a)$$

$$(3.36b)$$

For our present case with optical fibers we are interested in only the observable parts which are transmitted into the surrounding medium. These observable parts occur when $|k_{dx}| \leq \bar{k}$ and when $\bar{k} < |k_{dx}| \leq \bar{k}'$. The first case is obvious from the mathematics; however, the second case needs to be explained. When $\bar{k} < |k_{dx}| \leq \bar{k}'$ we are left with evanescent waves at the boundary $z = 0$. Then U_d is thus radiated into the cladding with an angle $|\alpha_d'| > |\alpha_{\text{critical}}|$ via the evanescent wave, but U_d^+ (unprimed i.e. inside holograms) decays before it reaches interface $z = z_0$ and is therefore not observable.

The figures presented in Section 3.2.1 can now be understood more clearly keeping in mind the dielectric structure (equations 3.23 and 3.24). In Figure 3.10, illumination with the reference wave $U_r(x)$ reconstructs the object wavefield $U_o(x)$ by interaction with the term $U_r^* U_o$ in the dielectric structure of the hologram. Figure 3.11 is the case when the hologram is illuminated with the conjugate reference wave, U_o^* , and this interacts with the terms $U_r^* U_o$ in the dielectric structure of the hologram. In Figure 3.12, illumination is via the object wavefield, U_o , which interacts with $U_r^* U_o$ term of the hologram. Finally, Figure 3.13 is the case of illumination with the conjugate object wavefield, U_r^* , which interacts with the terms $U_r^* U_o$.

3.2.2.3. Diffraction Efficiency

The diffraction efficiency, η , is defined as the ratio of the diffracted power P_d , and the illuminating wave P_c , both measured in the medium surrounding the hologram:

$$\eta \equiv P_d / P_c \quad (3.37)$$

Each of these powers is defined as the product of the illuminated area of the hologram, A , times the z component of the time averaged energy flow density, $\langle S_z \rangle$, as given by

$$P = A \langle S_z \rangle$$

where

$$S = E \times H \text{ (all quantities are vectors)}$$

and

$$\langle S_z \rangle = [1/(j\omega\mu_0)] U^2 \text{Re}\{k_z\}.$$

However, η is dependent on which terms in the dielectric structure are subject to interaction (see equations 3.21 - 3.24). Two separate efficiencies are found. For the interaction with $U_e^* U_p$ we

have

$$\eta_{\pm}(U_e^*U_p) = \left(\frac{\omega_c}{c}\right)^4 \left(\frac{d\epsilon}{dI}\right)^2 |U_d|^2 |U_p|^2 \frac{|k'_{cz}|}{|k'_{cz} + k_{cz}|^2} \frac{|k'_{dz}|}{|k'_{dz} + k_{dz}|^2} \frac{1}{|-k_{dz} + k_{cz} + k_{pz} - k_{ez}^*|^2}. \quad (3.38)$$

This is for the case where $|k_{dx}| \leq \bar{k}$ and for the configurations of Figures 2.3 and 2.4. Note that if $\bar{k} \leq |k_{dx}| \leq \bar{k}'$, then

$$\eta_+(U_e^*U_p) \equiv 0 \quad (3.39)$$

and $\eta_-(U_e^*U_p)$ is given by equation 3.38.

For the interaction with the term $U_e^*U_p$ we have for $|k_{dx}| \leq \bar{k}$

$$\eta_{\pm}(U_eU_p^*) = \left(\frac{\omega_c}{c}\right)^4 \left(\frac{d\epsilon}{dI}\right)^2 |U_d|^2 |U_p|^2 \frac{|k'_{cz}|}{|k'_{cz} + k_{cz}|^2} \frac{|k'_{dz}|}{|k'_{dz} + k_{dz}|^2} \frac{1}{|-k_{dz} + k_{cz} + k_{ez} - k_{pz}^*|^2}. \quad (3.40)$$

For $\bar{k} \leq |k_{dx}| \leq \bar{k}'$, we have

$$\eta_+(U_eU_p^*) \equiv 0 \quad (3.41)$$

and for $|k_{dx}| > \bar{k}$,

$$\eta_{\pm}(U_eU_p^*) \equiv 0. \quad (3.42)$$

3.2.3. Experiment

This section presents the details of the actual experiment performed. The experiment consisted of the following steps:

- 1) Fiber Preparation
- 2) Fiber Coating
- 3) Experimental Set-up
- 4) Sensitization of Gelatin
- 5) Exposure and Development
- 6) Data

Dichromated Gelatin (DCG) was employed as the holographic emulsion for the evanescent wave holograms produced in our experiments. DCG has been extensively used for hologram recording, and is a gelatin colloid that is sensitized to light with a ammonium dichromate solution. Upon exposure to light of a wavelength of 514 nm or shorter, cross-linking of the sensitized gelatin occurs where it was illuminated by light energy.³⁴ After exposure, the DCG emulsion is immersed

in a bath of water which swells the unexposed gelatin, while the cross-linked gelatin remains fixed. The refractive index of the cross-linked gelatin differs from that of the unexposed gelatin, making the resulting structure a phase hologram.

3.2.3.1. Fiber Preparation

The fiber utilized for the experiment was a Corning fiber with a 1521 glass code and a dual acrylate coating. The core diameter was 9 μm and the cladding diameter was 125 μm . The fiber had a single mode cutoff wavelength of approximately 1200 μm . A length of approximately 1.5 m of fiber is selected and the acrylate jacket was stripped by a razor blade near the middle. The length that is stripped was approximately 6 cm. The buffer layer between the jacket and the cladding must be chemically cleaned with isopropanol.

At this point the fiber was ready to be attached to special microscope-type slides prepared specifically for side-polishing of fibers. The microscope-type slides are ordinary slides of glass of a 6 to 7 cm length and approximately 2 cm width. One side of the slide is rounded with a radius of curvature of 10 inches (see Figure 3.15). It is on this curved side that the fiber is attached for side-polishing. The slides are placed in a wedge cut into a small block of wood so that they may stand upright with the curved portion on top. A thin layer of adhesive is spread onto the curved portion of the slide. The adhesive used is Revlon Clear Nail Polish which is chosen for its ease of spreading, relatively quick drying, and hardness. Before the nail polish dries, the stripped portion of the fiber is carefully placed on top and held slightly taut along the curved portion of the slide. It must be ensured that a small length (0.5 cm) of jacketed fiber extends onto the slide at both ends as this will provide extra mechanical strength. Also, care must be taken so that the fiber is not placed near the edges of the slide but is near the middle of the thickness of the slide. After the nail polish is relatively dry and the fiber is securely in place, an extra drop of polish is placed near the ends of the slide where the 0.5 cm of jacket is extending onto the slide. This is for extra mechanical strength (see Figure 3.15). The fiber/slide combination is then allowed to dry overnight in such a position so that the fiber is free to hang vertically from the edges of the slide.

After the fiber/slide is allowed to dry overnight, the fiber is ready for side-polishing. The slide is attached to a special apparatus designed at FEORC for side polishing of fibers. A helium neon laser beam is injected into the fiber and the output is constantly monitored via a power meter.

The slide is carefully lowered onto a polishing wheel with a 0.3 mm Aluminum oxide polishing pad. The wheel is turned at a moderate speed while water is flowing on the polishing pad. The slide is gently moved radially inwards and outwards along the wheel. Care must be taken to move the slide radially and also to avoid the very center and the outer edge of the wheel. Otherwise mechanical stress is placed in the fiber, which is easily broken.

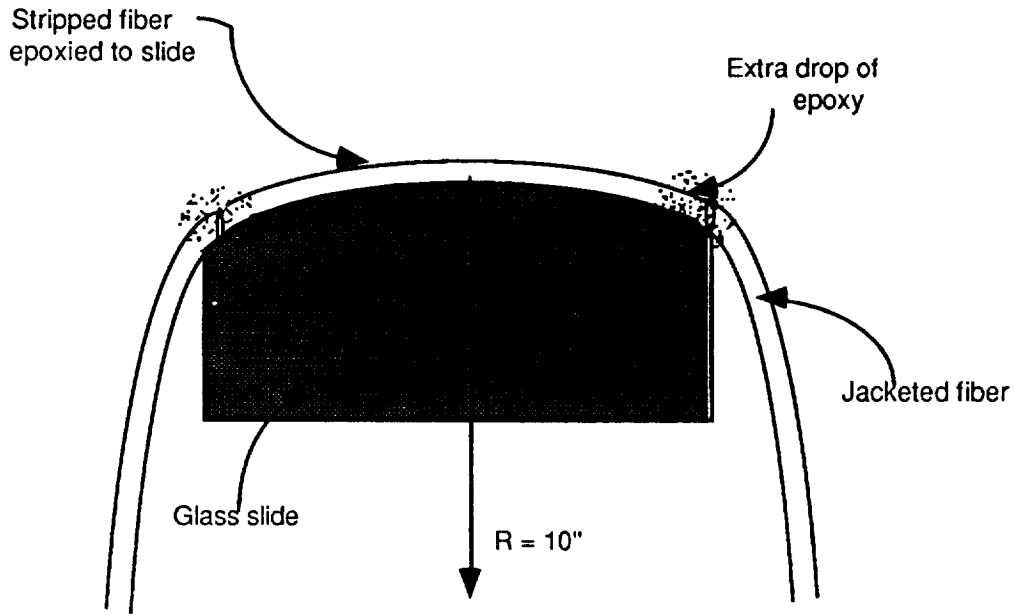


Figure 3.15.
Attachment of fiber to glass slide mount.

As the polishing is being performed, the power throughput of the fiber is constantly monitored. Since the fiber is in few mode operation, approximately 20% - 30% of its power is in the cladding region. As the side of the fiber is slowly polished and more of the cladding is removed, a portion of the cladding power escapes to the outside of the fiber. Generally, after 3 to 4 minutes of

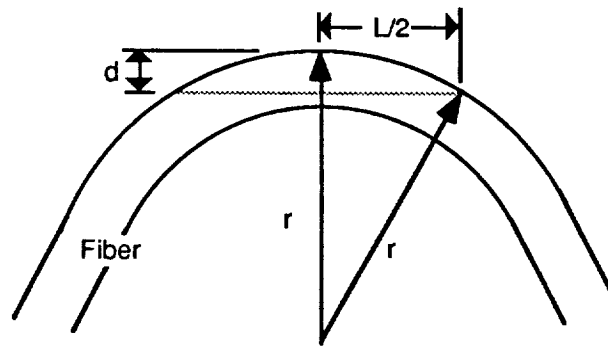


Figure 3.16.
Geometry for determination of depth of polish.

polishing an approximately 3 dB of power drop is encountered. This signifies that the evanescent region has been reached. At this point the slide is carefully removed and a drop of index matching fluid is placed on the polished portion of the fiber. The index matching fluid facilitates the radiation of escaped light, and eases the monitoring of the length of the portion of the cladding which has been removed. This length gives information as to how deep into the cladding we have penetrated as shown in Figure 3.16.

If the depth of polishing is found to be insufficient, the fiber is once again placed onto the polishing wheel. In the experiments performed, the depth polished was generally between 40 and 55 μm (The upper cladding later was only 60 μm thick). After the fiber has been polished to a satisfactory level, it is then ready for coating with gelatin.

3.2.3.2. Fiber Coating

Preparation of dichromated gelatin (DCG) film has been extensively discussed in the literature. Numerous methods and techniques for recording holograms in DCG films have been proposed. The number of variables affecting the outcome is enormous and strict control over every step of the process is necessary. For this reason, a detailed explanation of the steps and considerations involved in coating fibers for evanescent wave holography with DCG will be presented here.

In preparing the DCG for coating of fibers in this experiment, the general steps outlined in reference 31 were followed. The experiments reported by reference 31 dealt with producing holograms along planar optical waveguides utilizing the same principles of evanescent waves as discussed in the previous chapters.

The first obstacle to be overcome was that of satisfying the condition for internal reflection:

$$n_{\text{core}} > n_{\text{DCG}}$$

The approach taken in the experiment is as follows. The index of refraction of the core is 1.458 and that of the cladding is 1.455. The index of refraction of water is approximately 1.3; therefore preparing a gelatin solution in water with the least amount of gelatin possible would raise the index of refraction of water by a very small amount. A 12% solution by weight of gelatin in water has an index of refraction of 1.54 (which further increases when sensitized, see section 3.2.3.4 and reference 33), so that the amount of gelatin needed for our experiments had to be less than 12%.

Another important consideration in determining an acceptable gelatin to water ratio was that if there was not enough gelatin present, the solution would be useless since it would not be able to sustain a useful hologram. This was tested by making ordinary microscope slide DCG plates and

developing simple holograms.

The following steps were performed. Starting with deionized water at 40° C, an amount of gelatin was gradually added and the solution was stirred for approximately one hour. The gelatin to water ratio (by weight) was varied from 12% to 1% in increments of 1%. The gelatin used was Fisher gelatin with a bloom strength of 200.

Each time a solution was made, it was coated onto the fiber/slide by dipping the fiber/slide into it. The fiber/slide was then pulled out so that the polished edge of the fiber came out last and a fine film of gelatin clung to this polished edge. The thickness of the fine film remaining is not important as long as it is much larger than a few wavelengths of the light used for exposure (i.e. 441.6 nm) . Care must be taken so that no air bubbles are allowed to cling to the fiber as this will distort the results. At this point the fiber is hung up for overnight drying in such a manner that the polished edge is facing down so that most of the gelatin is allowed to flow to the polished edge. The polished edge was parallel to the ground so that a uniform film coated the polished edge of the fiber.

When the gelatin had dried overnight, it was then prehardened for 15 minutes in Kodak Rapid Fix® and rinsed in running water of approximately 22° C for another 15 minutes. The reason for the prehardening step is to make the gelatin insoluble in water when further processed.

The film was again allowed to dry overnight in the same manner as discussed previously, and was then ready to be tested for the internal reflection condition. The test performed is as follows: Each time a film was prepared with a different gelatin content (varying from 12% to 1%) , a helium-cadmium laser was injected into one end of the fiber. If the condition for internal reflection was met, then no light should escape from the polished edge of the fiber. This condition was met for gelatin solutions of 1%, 2% and 3%. However, when these concentrations were used to prepare conventional holograms of simple objects using these DCG concentrations on ordinary microscope slides, all attempts failed. This indicated that these concentrations (1%, 2%, and 3%) were insufficient for writing holograms with sufficient depth of refractive index modulation. A compromise had to be made between the amount of index mismatch tolerable between the fiber and DCG, and the ability to obtain useful holograms. For this reason the concentration of gelatin was again increased in increments of 1% until a satisfactorily conventional DCG plate and an ordinary hologram was obtained. Satisfactory results were achieved with gelatin concentrations of 5% and 6%. At 5% and 6% concentrations a small amount of light did escape near the polished edge of the fiber but this had to be tolerated in order to obtain useful holograms. All the experiments reported from here with optical fibers were performed with a gelatin concentration of 5%.

3.2.3.3 Experimental Set-up

A number of factors were kept in consideration upon arranging the set-up illustrated in Figure 3.17. First, successful results were obtained with a helium-cadmium laser emitting at 441.6 nm in a TEM_{00} mode. The coherence length of the laser was measured to be approximately 7 cm, so the optical path length difference of the two interfering beams measured at the polished spot had to be much less than 7 cm. Since the fiber propagated more than one mode at 441.6 nm, determining a value for the exact path length difference requires solving for the path length of the various modes within the fiber. This was simplified by assuming that the velocity of each mode is equal to c/n_1 (where n_1 is the fiber core refractive index, and c is the free space speed of light) and then solving for the path length within the fiber.

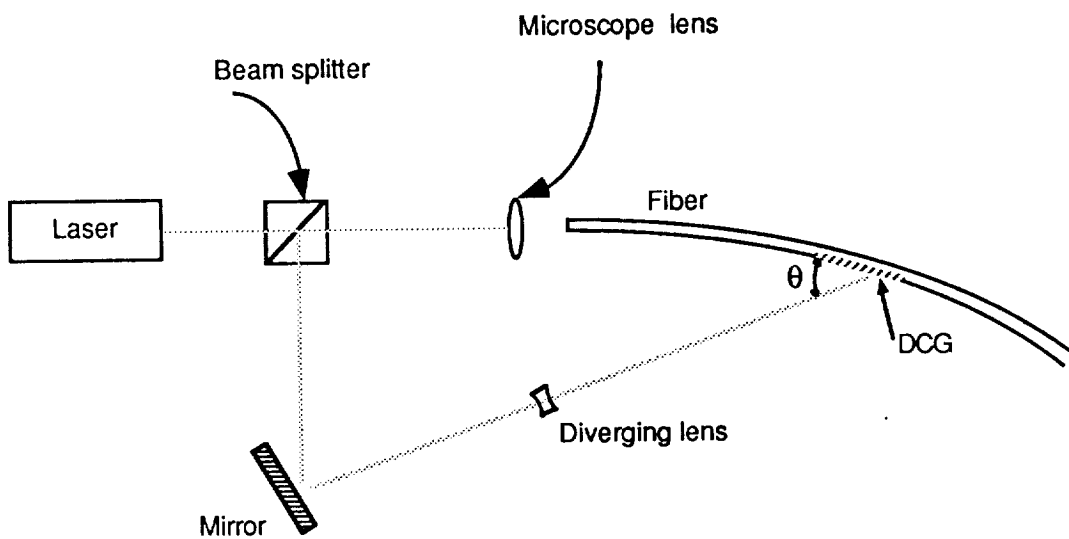


Figure 3.17.
Experimental set-up for exposure of hologram.

Another consideration was the ratio of the beam intensities. Generally a reference to object wave ratio of 3/1, to 6/1 is recommended for good holograms. In our experiments this ratio was difficult to determine since the exact intensity of the reference or evanescent wave was unknown. A good approximation to the intensity of the evanescent wave is to view the amount of light that is leaking out at the polished spot due to the index mismatch of the fiber and the gelatin. This would provide a lower-bound estimate of the strength of the evanescent wave, due to the fact that most of the power of the evanescent wave would remain very close to the fiber and only a small portion travels away. In the experiments performed, we attempted to maintain the beam ratio at 3 to 1. This was achieved by using a 80/20 beamsplitter and injecting the stronger beam into the fiber.

3.2.3.4 Sensitization of Gelatin

In the experiments performed, sensitization of the gelatin film with ammonium dichromate $[(\text{NH}_4)_2\text{Cr}_2\text{O}_7]$ also proved to be more complicated than anticipated. The first problem encountered was the determination of the proper concentration of the ammonium dichromate. Recipes for concentrations of 4% up to concentrations of 7% ammonium dichromate in water exist in the literature. Experiments performed in evanescent wave holography with planar optical waveguides suggest the use of concentrations of 1% to 2% of ammonium dichromate.³⁵ The concentration changes the index of refraction of the film drastically from 1.54 for a concentration of 0%, to 1.58 for a concentration of 3%.³³ In order to keep the index of refraction as low as possible, we required the smallest concentration of ammonium dichromate. The figures cited are for a gelatin concentration of 12% by weight. Again since we need a very low film index (for lightwave guidance in the fiber), both the gelatin concentration (as discussed in section 3.2.3.2) and the ammonium dichromate concentration needed to be as low as possible but high enough to yield sufficient modulation of refractive index in the recorded holograms. The appropriate concentration for ammonium dichromate was determined empirically through a series of well-controlled trials. That is, each time a certain concentration of gelatin was tested, the test microscope slides were sensitized with concentrations of 0.5% and 1.5% of ammonium dichromate, and then simple holograms of ordinary objects were attempted. At a concentration of 0.5% of ammonium dichromate, the attempts of making simple holograms failed both at low and high concentrations of gelatin. At a concentration of 1.5% of ammonium dichromate, attempts of making simple holograms failed for gelatin concentrations of up to 3% but were more successful at higher concentrations.

Again a compromise had to be made between the gelatin concentration, ammonium dichromate concentration and the index mismatch tolerable between the fiber and the DCG. Best results were obtained with a gelatin concentration of 5% to 6% and an ammonium dichromate concentration of 1%.

Another practical problem was the technique of sensitization. The film had to be sensitized after the fiber had been aligned with the lens and the two laser beams. This was required since the film would have to be exposed to the laser beams for alignment, if the film were sensitized before alignment, and this would prematurely expose it. For this reason, the fiber was aligned and then the film was sensitized very carefully without misaligning the fiber. The film was then allowed to dry for approximately 24 hours in place and in a light tight box, again without misaligning the fiber. The actual sensitization was accomplished by dipping the fiber/slide in the ammonium dichromate solution for 4 to 5 minutes.

3.2.3.5 Exposure and Development

The next step in making the holograms is the exposure. Numerous attempts were made at various angles of incidence and with different exposure times. Best results were obtained with exposure times of 20 seconds and 30 seconds. The angle of incidence varied from 15 degrees to 90 degrees as shown in Figure 3.17.

Development of the film was fairly straight forward. To develop the film, it was first washed in running water at approximately 20° C for 15 minutes. As the film is pulled out of the water it was rinsed with a jet of isopropyl alcohol to remove excess water. The film was then bathed in fresh isopropyl alcohol for 2 minutes and finally pulled out slowly while simultaneously being dried with a stream of warm air. If all steps involved in making the hologram were successful, at this point the hologram was now recorded.

3.2.3.6 Data

Data is presented in Table 3.2 for three separate holograms illuminated as in Figure 3.10. The diffracted waves were measured by a detector with a wedged cap on it. The slide was carefully inserted into the wedge so only the diffracted wave being measured is incident upon the detector. Even with the precaution of using a wedged cap, a small amount of stray light was still present. The reconstructing(reference) wave was measured by a cut back technique, after the diffracted waves were measured. The fiber was cut near the slide without moving it with respect to the lens and the laser beam. The cut end was then cleaved and the total power in the fiber was measured. It must be realized that at the wavelength of 441.6 nm approximately 10% of the total power is in the cladding and it is this 10% which illuminates the hologram. Therefore, the efficiencies are calculated with this 10% figure and not the total power measured.

θ_i	\overline{U}_o		U_o		Power in Fiber	
	Power	η	Power	η	Total	10%
15	.0006	3.79%	.0012	7.59%	.0158	.158
45	.0018	4.10%	.0019	4.34%	.0438	.438
60	.0021	2.17%	.0037	3.83%	.0965	.965

Table 3.2 Measured efficiencies for hologram reconstruction.

Efficiencies varied from 2.17% to 7.59%. The efficiency for U_o is generally higher than that for \overline{U}_o . The efficiencies are not very high and techniques for improving the efficiencies have not been investigated yet. Illumination as shown in Figure 3.12 was attempted but was not successful,

and a diffracted beam was not observed. Two reasons may explain the failure of this mode of illumination. First, the angular dependence of this mode of illumination is very strong. In other words, if U_o is not incident at a very precise angle, U_T is not diffracted. The second reason for this may be that upon the interaction of U_o with the hologram, a true evanescent wave is not generated along the boundary due to scattering, and therefore U_r is not observed.

3.2.4 Discussion

The evanescent wave holograms made in our experiments demonstrated a sensitivity to injection conditions at the fiber input. A diffracted beam was not always seen even when light was injected into the fiber. Only after adjusting the fiber with respect to the input laser beam and changing the launching conditions, was it possible to see a diffracted beam. Also, when the power launched into the fiber was monitored and maximized, the diffracted beams were not necessarily maximized. Only by changing the initial launching conditions could the diffracted beams be maximized. The reason for this is probably that the hologram reconstruction is most efficient for specific propagating modes: that is, those modes which constructed the hologram initially, most likely the higher order modes with greater evanescent field penetration into the fiber cladding. Changing the launching conditions changes the power distribution among the modes and therefore the hologram efficiency.

We also attempted reconstructing the holograms with two different wavelengths simultaneously. A helium-neon (632.8 nm) laser beam was combined with the helium-cadmium output (441.6 nm) by using a beamsplitter. Due to the Bragg-grating-like structure of the DCG, the hologram should angularly translate these different wavelengths to different output angles. In other words the two different wavelengths would be diffracted at different angles and would thus be viewed at different positions. This phenomena was not clearly observed in our experiments. A number of possible reasons for this exist, the first and most important being the low efficiency obtained with our emulsions. Another reason was the inability to visually resolve this angular separation. Viewing the angular separation was made difficult by the large amount of the helium-neon light being scattered into the cladding and blurring the diffracted beams. Changing the launching conditions would result in either helium-neon laser light being diffracted or helium-cadmium light being diffracted. The launching conditions thus determined which wavelength was being diffracted. An efficient hologram which separated the wavelength efficiently could be of great interest for communications technology and could be used as a type of fiber spectrometer as proposed in reference.¹³

The lifetime of the hologram is also found to be rather short. Since the temperature, humidity and cleanliness of the lab environment was not controlled, the holograms deteriorated with time. One or

two days after exposure (depending on the factors just mentioned) , the hologram would completely deteriorate. This problem can be alleviated by encasing the hologram in a plate of glass or an optical cement. However, this was not investigated.

3.2.5 Conclusions

The experiments performed demonstrate the feasibility of developing a grating hologram along an optical fiber. The steps involved are summarized in Table 3.3.

- 1) Stripping of fiber coating and adhering to glass slide with 10 inch radius edge.
- 2) Dry overnight.
- 3) Gelatin coating with 5 to 6 percent gelatin in de- ionized water.
- 4) Dry overnight in vertical position.
- 5) Prehardening in Kodak Rapid Fix for 15 minutes.
- 6) Rinse in running water for 15 minutes.
- 7) Dry and store.
- 8) Alignment of optics including fiber/slide.
- 9) Sensitization in 1% solution of ammonium dichromate for 4 - 5 minutes without disturbing alignment. This is done approximately 24 hours before exposure.
- 10) Exposure at a wavelength of 441.6 nm.
- 11) Development: a) wash in running water (T= 20 C) for 15 minutes.
b) rinse with a jet of isopropyl alcohol for 2 minutes.
c) immerse in fresh isopropyl alcohol for 2 minutes.
d) Pull out slowly while simultaneously drying with a stream of warm air.

TABLE 3.3
Procedure for fabrication of Evanescent Wave Holograms in Optical Fibers

The efficiencies obtained varied from 0% to 7.5% depending on the mode of reconstruction. These efficiencies are fairly low but the intent of the experiment is to demonstrate only the feasibility of evanescent wave holography with optical fibers. Certain modes of reconstruction need to be better controlled so as to improve efficiency. Temperature, humidity and cleanliness of the environment in which the experiment is performed is critical and must be controlled. Preserving the hologram by an optical cement or a plate of glass must be investigated. The experiments performed show that evanescent wave holography with optical fibers is indeed possible and further investigations should improve technique and hologram efficiency.

4.0 Active Fiber Technology

Research was initiated into the development of low cost techniques for doping glass rods with lanthanide rare earth in order to render the rods capable of amplification of optical signals. Samples were prepared by indiffusion of neodymium into soda lime glass, but the level of doping could not be measured due to limits of the available spectroscopy instruments. Optical signal amplification has not yet been observed. Optical fibers doped with rare earths are expected to have applications for signal amplification in optical communications, and as distributed temperature sensors due to the temperature dependence of the fluorescence of rare earths.³³

4.1. Rare-earth Based Glass Amplifiers

The main project goal for development rare-earth glass amplifiers was to examine the existing technique of manufacturing rare earth-based optical fiber and to develop some novel inexpensive techniques to fabricate such a fiber/glass rod. An experiment to demonstrate light amplification with a newly developed glass rod was also performed. However, a significant amount of amplification could not be observed due to the unavailability of a suitable pumping source.

4.1.1. Existing Technique to Manufacture Rare-earth Fiber/Glass Rod

The technique presently used for manufacture of active fibers is an extended modified chemical vapor deposition (MCVD) process.³³ It allows the fabrication of both singlemode and multimode optical fibers containing rare earth ions at concentrations of up to 0.25 percent by weight in the core region. The process is shown in Figure 4.1. The starting material can be a rare earth halide, e.g. $\text{NdCl}_3 \cdot 6\text{H}_2\text{O}$ (99% pure, melting point = 758°C). It is first inserted into a dopant carrier chamber, where it is dehydrated by heating under a Cl_2 atmosphere. This step also fuses the anhydrous NdCl_3 crystals to the chamber wall, thus preventing them from passing down the tube and forming bubbles in glass subsequently deposited. The inside of the glass tube is then cleaned by gas-phase etching using SF_6 to remove any dopant deposited during the drying process. After this drying stage, the cladding glass is deposited.

During the core deposition, the dopant carrier chamber is heated to about 1000°C by a stationary burner which produces small amounts of NdCl_3 vapor. This vapor is subsequently carried downstream, is oxidized to form Nd_2O_3 , which in turn is incorporated in the core. This process takes place in the hot zone which is formed by the moving deposition burner. In order to produce low-loss fibers, a second drying stage is also introduced. In this process the core, consisting of SiO_2 , GeO_2 and a small amount of Nd_2O_3 , is deposited unfused at a low temperature. This porous core layer on the inside of the deposition tube is subsequently dried by heating in a Cl_2 atmosphere, after which it is fused to form a clear nonporous layer. The tube is then conventionally

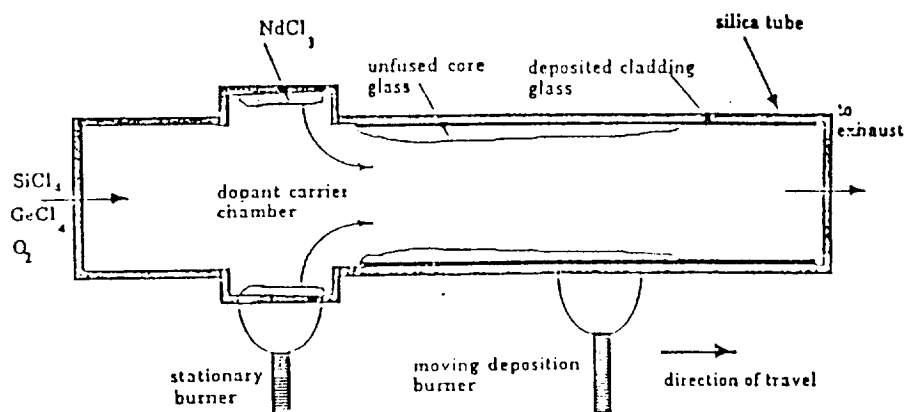


Figure 4.1
Extended MCVD process for fabrication of rare-earth-based optical fibers

collapsed to form a solid rod and then pulled into a fiber. This is a very flexible technique as any kind of rare earth ions can be incorporated. Fibers fabricated by this technique have produced losses as high as 3000 dB/Km in the visible and near infrared regions, and < 2 dB/km in the low-loss window between 950 and 1350 nm.

4.1.2. Diffusion Technique to Fabricate Rare-earth Fiber/Glass Rod

A novel technique to fabricate rare earth-based fiber/glass rod was investigated by diffusing the rare earth ions from the outside surface of a glass rod. The glass rod selected for this experiment was a soda-lime glass rod (Fisher Cat. No. 11-375C). This type of glass contains a relatively large amount of easily displaceable impurity ions, and hence the process of diffusion by the ion displacement technique can be made possible.

Several techniques were attempted which involved coating different rare-earth compounds on the outside surface and then subjecting the glass rod to high temperatures for various durations of time. One of the problems faced in coating the glass rod was that the rare-earth compound did not adhere to the glass surface very firmly because of its smoothness. As a result, a uniform layer of coating was not achieved. This problem was alleviated by first sand-blasting the glass rod, at the expense of adding higher transmission losses in the rod due to scattering at the roughened surface. The rare-earth compound used was neodymium 2,4-pentanedionate. This compound has the advantage that it readily dissolves in acetone, and once this paste was coated on the glass rod, the acetone evaporated leaving behind a uniform coat of this rare-earth compound. The coated glass

rod was then heated in a tube furnace at a temperature of 500° C for a period of ten days (the softening point of this glass rod was 700 °C). Different temperatures ranging from 550° C to 650° C were also tried. However, this resulted in the bending of glass rods when a few hours had elapsed. The initial part of the experiment was performed under a fume-hood since neodymium 2,4-pentanedionate emits carbon monoxide, carbon dioxide, and other toxic fumes before forming Nd_2O_3 .³⁴ Figure 4.2 shows the experimental set-up for this process.

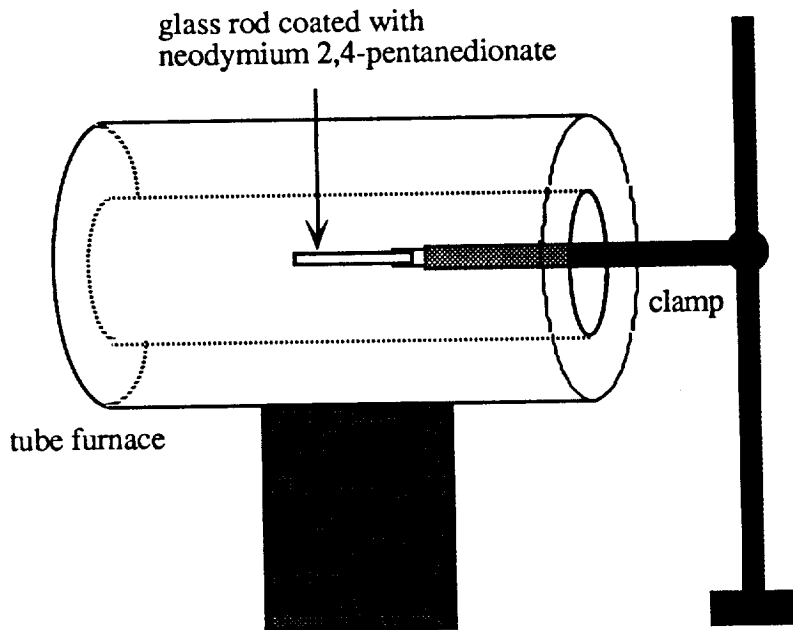


Figure 4.2
Set-up for diffusion experiment.

The diffused sample was observed across its diameter with a cathode luminescope, while the neodymium ions were bombarded by electrons to cause their excitation. Typically, a zoning effect would determine the presence of a particular kind of impurity in the bulk material. A zoning effect could not be observed to a significant amount with this sample. However, a bright blue layer, of the order of a few microns, close to the circumference, was observed. Again, this did not confirm the presence of Nd doping since the presence of a high concentration of Nd_2O_3 on the surface can possibly give an impression of diffusion when the sample is observed under a microscope. Further characterization of this sample is required to determine the exact nature of the diffusion effect on the glass rod.

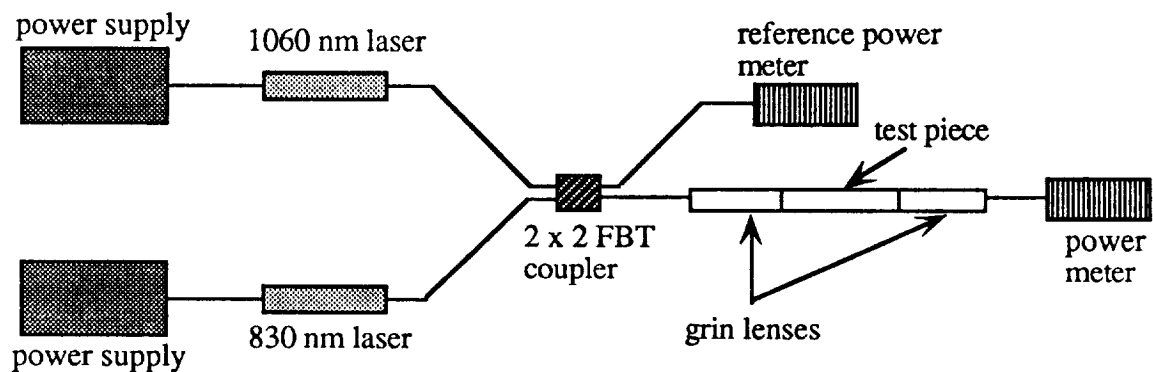


Figure 4.3
Experiment for measurement of optical signal amplification.

4.1.3. Optical Signal Amplification Experiment

The experimental set-up which was used is shown in Figure 4.3. A 2x2 multimode FBT coupler was used to combine the pump signal and the signal to be amplified onto a single fiber. A quarter-pitch gradient index (GRIN) lens collimated the light from the fiber into the test piece, thereby allowing end pumping of the test piece. This test piece was the diffused sample described earlier. The pumping source used was an 830 nm LED and the signal to be amplified came from a 1060 nm LED. This LED, which had a 30 nm full width half maximum linewidth (FWHM), was selected because the main transition line occurring from the transition ${}^4F_{3/2} \rightarrow {}^4I_{11/2}$, was assumed to be within this region. No prior information for the main transition line was found in the available literature. No significant amount of amplification was observed. This can be attributed to the fact that most of the neodymium ions, if any, were concentrated close to the surface of the glass rod.

4.2. Discussion

The lack of success in either measuring optical gain in the glass rod or even a detectable level of dopant suggest that a simple diffusion of neodymium into a soda-lime glass rod will not yield a dopant concentration sufficient to support amplification. Even if a suitable concentration level had been achieved, the sandblasting of the rod surface would have resulted in very high surface scattering losses. Had such a neodymium-doped rod been incorporated into a silica tube and collapsed to form an active fiber preform, the attenuation of the resulting fiber drawn from such a preform would have been large from core-clad interface imperfections.

¹ Thomas J. Rathz and Michael B. Robinson, "The NASA/Marshall Space Flight Center Drop Tube User's Manual," NASA Technical Memorandum TM-100392, March 1990.

² Michael B. Robinson, "Radiative and Gas Cooling of Falling Molten Drops," NASA Technical Memorandum TM-78189, 1978.

³ W. Hofmeister and R.J. Bayuzik, "Noncontact Temperature Measurement of a Falling Drop," Proceedings of the Second Noncontact Temperature Measurement Workshop, JPL Publication 89-16, Jan.17, 1989.

⁴ A. Feingold, K.G. Gupta, "New Analytical Approach to the Evaluation of Configuration Factors in Radiation from Spheres and Infinitely Long Cylinders," *Jour. of Heat Transfer*, Feb. 1970, pp. 69 - 76.

⁵ Bornstein, A., Bichman, P., "Multimode and single-mode IR fiber characterization," *Proceedings of SPIE*, vol. 1048, Infrared Fiber Optics, 16 - 17 January 1989, Los Angeles, CA, pp 104 - 111.

⁶ Dror, J., Gannot, I., Croitoru, N.I., "Hollow tubes for transmitting IR laser energy for surgery applications," *Proceedings of SPIE*, vol. 1048, Infrared Fiber Optics, 16 - 17 January 1989, Los Angeles, CA, pp. 112 - 116.

⁷ Harrington, J.A., Gregory, C.C., Nubling, R.K., "Hollow waveguides for CO₂ laser delivery systems," *Proceedings of SPIE*, vol. 1048, Infrared Fiber Optics, 16 - 17 January 1989, Los Angeles, CA, pp 117 - 121.

⁸ Milman, Microelectronics, McGraw-Hill Book Company, New York, 1979, Pg 586.

⁹ Ziemer and Tranter, Principles of Communications - Systems, Modulation, and Noise, Houghton Mifflin Company, 1976, Pg. 63.

¹⁰ K. A. Murphy, M.S. Miller, A.M. Vengsarkar, R.O. Claus, and N.E. Lewis, "Embedded modal domain sensors using elliptical core optical fibers," *Proc. of SPIE on Smart Structures*, Boston, MA, Sept. 1989.

¹¹ R.O. Claus, B.D. Zimmermann, K.A. Murphy, and A.M. Goette, "Distributed Strain Sensing in Structures using Optical Fiber Time Domain Methods," *Proceedings, Eighth Biennial Conference of Failure Prevention and Reliability*, Montreal, Sept. 17 - 21, 1989.

¹² K.D. Bennett, J.C. McKeeman, and R.G. May, "Full Field Analysis of Modal Domain Sensor Signals for Structural Control," *Proc. of SPIE on Fiber Optic Smart Structures and Skins*, vol 986, Boston, MA, 8-9 September 1989.

¹³ J.W. Goodman, Introduction to Fourier Optics, McGraw-Hill, New York, 1968.

¹⁴ Hadbawnik, D., "Holographische endoscopic", *Optic*, 45, 1, pp. 21-38, 1976.

¹⁵ Yonemura, M., Nishisaka, T., Machida, H., "Endoscopic hologram interferometry using fiber optics", *Appl. Opt.*, 20, 9, pp. 1664-1667, 1981.

- ¹⁶ Gilbert, J. A., Dudderar, T. D., Schultz, M. E., Boehnlein, A. J., "The monomode fiber - a new tool for holographic interferometry", Proc. of the 1982 Joint Conference on Exp. Mech. SESA/JSME, Oahu-Maui, Hawaii, May 23-28, pp. 920-922, 1982.
- ¹⁷ Brunetaud, J. M., Enger, A., Berjot, M., Moschetto, Y., "The interest of optical monofibres in medical practice", *Onde. Electr.*, 59, 2, pp. 59, 1979.
- ¹⁸ Jones, J. D. C., Corke, M., Kersey, A. D., Jackson, D. A., "Single-mode fibre-optic holography", *J. Phys. E.*, 17, 4, pp. 271-273, 1984.
- ¹⁹ von Bally, G., "Otosopic Investigations by Holographic Interferometry: A Fiber Endoscopic Approach Using a Pulsed Ruby Laser System", *Springer Ser. Opt. Sci. (Optics in Biomedical Sciences)*, 31, pp. 111-114, 1981.
- ²⁰ Dudderar, T.D., Gilbert, J. A., "Fiber optic pulsed laser holography", *Appl. Phys. Lett.*, 43, 8, pp. 730-732, 1983.
- ²¹ Albe, F., "High-speed fiber optic holography", *J. Opt.* 15, 6, pp. 397-402, 1984.
- ²² Albe, F., Fagot, H., Smigielski, P., "Use of optical fibers in pulsed holography", *Proc. SPIE*, Vol. 492 ECOOSA '84, pp. 324329, 1985.
- ²³ Gilbert, J. A., Herrick, J. W., "Holographic displacement analysis with multimode-fiber optics", *Exp. Mech.*, 21, 8, pp. 315-320, 1981.
- ²⁴ Gilbert, J. A., Schultz, M. E., Boehnlein, A. J., "Remote displacement analysis using multimode fiber-optic bundles", *Exp. Mech.*, 22, 10, pp. 398-400, 1982.
- ²⁵ Dudderar, T. D., Gilbert, J. A., Franzel, R. A., Schamell, J. H., "Remote vibration measurement by time-averaged holographic interferometry", *Proc. of the V Int. Cong. on Exp. Mech.*, Montreal, Canada, June 10-15, 1984, pp. 362-366, 1984. See also: *Exp. Tech.* 9, 1, pp. 25-27, 1985.
- ²⁶ Dudderar, T. D., Hall, P. M., Gilbert, J. A., "Holointerferometric measurements of the thermal deformation response to power dissipation in multilayer printed wiring boards", *Exp. Mechs.*, 25, 1, pp. 95-104, 1985.
- ²⁷ Dudderar, T. D., Gilbert, J. A., "Real-time holographic interferometry through fibre optics", *J. Phys. E*, 18, 1, pp. 39-43, 1985.
- ²⁸ Corke, M., Jones, J. D. C., Kersey, A. D., Jackson, D. A., "All single-mode fibre optic holographic system with active fringe stabilization," *J. Phys. E.*, 15, 3, pp. 185-186, 1985.
- ²⁹ Hill, K., Fujii, Y., "Photosensitivity in optical fiber waveguides: Applications to reflection filter fabrication", *Appl. Phys. Lett.*, 32, 10, pp. 647-649, 1978.
- ³⁰ Russell, P., Ulrich, R., "Grating-fiber coupler as a high resolution spectrometer", *Optics Lett.*, 10, 6, pp. 291-293, 1985.
- ³¹ Bennion, I., Reid, D., "High-reflectivity monomode fiber grating filters", *Electronics Lett.*, 22, 6, pp. 343-345, 1986.

³² Glenn, W.H., Meltz, G., Snitzer, E., "Method for Impressing Gratings Within Fiber Optics," United States Patent 4,725,110, Feb. 16, 1988.

³³ Wuthrich, A., Lukosz, W., "Holography with Evanescent Waves", *Optik*, 41, 2, pp. 191-211, 1974

³⁴ Saxby, G., Practical Holography, Prentice Hall, NY, 1988, pp 274 - 275.

³⁵ Jeong, T. H., Kupiec, optics in holography," *Proc. Int. Symp. on Display Holography* Vol. II, Pub. by Holography Workshops, Lake Forrest College, Lake Forest, Il 60045, pp. 6971, 1986.

Appendix A.
NASA1 FORTRAN
Configuration Factor Model

```

PROGRAM NASA1
IMPLICIT REAL*8 (A-Z)
PI=3.141592700
DO 50 K=773.000,3773.000,500.000
DO 40 H=10.000,200.000,10.000
D1=0.200
R1=D1/2.000
A1=PI*(R1)**2
D2=3.000
R2=D2/2.000
A2=4.000*PI*(R2)**2
L=0.152400
G=9.80600
NA=0.400
THETA=DARSIN(NA)
X=L*DTAN(THETA)
S1=H-X
S2=H+X
V0=(2.000*G*H)**0.5
V1=(2.000*G*S1)**0.5
V2=(2.000*G*S2)**0.5
T0=V0/G
T1=V1/G
T2=V2/G
T=(T2-T1)
DT=T*1000.000
SF=5.66961D-8

R=((R1/1000.000)**2)/(4.000*L)
A=(L**2)+(X**2)
B=-((4.000*X**2)/T)
C=((2.000*X)/T)**2
DF0=C*(T0**2)+B*T0+A
DF1=C*(T1**2)+B*T1+A
C1=C**0.5
DF2=(1.000/C1)*DLOG(DF0**0.5+T0*C1+B/(2*C1))
DF3=(1.000/C1)*DLOG(DF1**0.5+T1*C1+B/(2*C1))
DF=2.000*R*(DF2-DF3)
Q=SF*(K**4)*DF*(A2/(1000.000**2))
WRITE (9,10) H, DT, Q, K
10  FORMAT (2X,F6.1,2X,F10.5,2X,D18.10,2X,F6.1)
40  CONTINUE
50  CONTINUE
STOP
END

```

Appendix B.

**NASA2 FORTRAN
Tilted Fiber Model**

```

PROGRAM NASA2
IMPLICIT REAL*8 (A-Z)
PI=3.1415927D0
K=3773.0D0
DO 40 H=10.0D0,200.0D0,10.0D0
DO 30 BETA=1.0D0,20.0D0,1.0D0
D1=0.2D0
R1=D1/2.0D0
A1=PI*(R1)**2
D2=3.0D0
R2=D2/2.0D0
A2=4.0D0*PI*(R2)**2
L=0.1524D0
G=9.806D0
NA=0.4D0
THETA=DARSIN(NA)
THETA1=(180.0D0/PI)*THETA
BETA1=THETA1+BETA
BETA2=(PI/180.0D0)*BETA1
NX1=L*DTAN(BETA2)
BETA3=THETA1-BETA
BETA4=(PI/180.0D0)*BETA3
NX2=L*DTAN(BETA4)
NX=NX1+NX2

S1=H-NX1
S2=H+NX2
V0=(2.0D0*G*H)**0.5
V1=(2.0D0*G*S1)**0.5
V2=(2.0D0*G*S2)**0.5
T0=V0/G
T1=V1/G
T2=V2/G
T=(T2-T1)
DT=T*1000.0D0
SF=5.66961D-8

R=((R1/1000.0D0)**2)/(4.0D0*L)

A=(L**2)+((NX1)**2)
B=-((2.0D0*NX1*NX)/T)
C=(NX/T)**2
DF0=C*(T0**2)+B*T0+A
DF1=C*(T1**2)+B*T1+A
C1=C**0.5
DF2=(1.0D0/C1)*DLOG(DF0**0.5+T0*C1+B/(2*C1))
DF3=(1.0D0/C1)*DLOG(DF1**0.5+T1*C1+B/(2*C1))
DF4=R*(DF2-DF3)

A1=(L**2)+((NX2)**2)
B1=-((2.0D0*NX2*NX)/T)
C2=(NX/T)**2
DF01=C2*(T2**2)+B1*T2+A1
DF11=C2*(T0**2)+B1*T0+A1
C3=C2**0.5

```

NASA2 FORTRAN A1 09/22/88 22:04 F 80 67 RECS 09/22/88

```
DF21=(1.0D0/C3)*DLOG(DF01**0.5+T2*C3+B1/(2*C3))
DF31=(1.0D0/C3)*DLOG(DF11**0.5+T0*C3+B1/(2*C3))
DF41=R*(DF21-DF31)
```

```
DF=DF4+DF41
Q=SF*(K**4)*DF*(A2/(1000.0D0**2))
WRITE (9,10) H, BETA, DT, Q
10  FORMAT (2X,F6.1,2X,F6.1,2X,F6.3,2X,D18.10)
30  CONTINUE
40  CONTINUE
STOP
END
```

Appendix C.
Ratio Pyrometry Model

C234567

```
*****
* THIS PROGRAM EVALUATES THE INTEGRAL OF PLANCK'S EQUATION OVER THE *
* WAVELENGTH LIMITS OF TWO IDEALIZED FILTERS, SEPERATELY. IT THEN *
* TAKES THE RATIO OF THESE RESULTS TO OBTAIN A SINGLE-VALUED CURVE *
* WHICH IS USED FOR THE RATIO PYROMETRY EXPERIMENT. *
* SARA MONEYHUN *
*****
```

```
PROGRAM PROOF
$DEBUG
EXTERNAL F
COMMON K,EMM
INTEGER T
REAL A1,B1,EPS,R1,E1,KF1,KE1,K,F,C1,C2,EMM,A2,B2,R2,E2,
& KF2,KE2,RT
OPEN(2,FILE='PROOF.DAT')
OPEN(3,FILE='FILTER1.DAT')
OPEN(4,FILE='FILTER2.DAT')
OPEN(5,FILE='RATIO.DAT')
M=30
WRITE(2,*)M
```

```
C PARTICLE EMISSIVITY
EMM=0.8
WRITE(3,50) EMM
WRITE(4,50) EMM
WRITE(5,50) EMM
```

```
C SET FILTER LIMITS
a1=2.763
b1=2.882
a2=3.0465
b2=3.1535
```

```
EPS=0.01
WRITE(3,150) A1,B1
WRITE(3,151)
WRITE(4,152) A2,B2
WRITE(4,153)
WRITE(5,150) A1,B1
WRITE(5,152) A2,B2
WRITE(5,154)
DO 10 T=500,3500,100
K=T+273.0
CALL H2A1 (A1,B1,EPS,R1,E1,KF1,KE1)
CALL H2A1 (A2,B2,EPS,R2,E2,KF2,KE2)
WRITE(3,*) R1,T
WRITE(4,*) R2,T
RT=R1/R2
WRITE(2,100) RT,T
WRITE(5,*) RT,T
```

```
10 CONTINUE
50 FORMAT(3X,'Particle Emmissivity =',F5.4,/)
100 FORMAT(F14.9,1X,I5)
150 FORMAT(5X,'FILTER R1 where A1=',F6.3,1X,'and B1=',F6.3,
& '(in microns)',/)
151 FORMAT(15X,'R1',10X,'T',/)
152 FORMAT(5X,'FILTER R2 where A2=',F6.3,1X,'and B2=',F6.3,
& '(in microns)',/)
153 FORMAT(15X,'R2',10X,'T',/)
154 FORMAT(9X,'R1/R2',13X,'T',/)
BTOP
```

Appendix D.
Prototype Pyrometer
Component List

The following components were mounted on rails for ease in positioning:

- 1 - Calcium Fluoride (CaF_2) Rod
 - manufacturer: Glass Fab
 - 1" X 6" rod with polished endfaces

- 1 - Calcium Fluoride Beamsplitter
 - manufacturer: Oriel Corporation
 - model number: 44373

- 2 - Infrared Narrowband Filters
 - manufacturer: Corion
 - center wavelength 2.82 μm (half peak bandwidth 119 nm)
 - center wavelength 3.12 μm (half peak bandwidth 107 nm)

- 2 - Calcium Fluoride Lenses
 - manufacturer: Ealing Electro-optics
 - catalog number: 34-3483

- 2 - Indium Antimonide (InSb) Detectors
 - manufacturer: EG&G Judson
 - J10D Series

- 2 - Preamplifiers
 - manufacturer: Perry
 - model number: 481-44

Appendix E.
Data Transfer Program

```

/* This is a C program to acquire waveforms from a LeCroy 9450
   oscilloscope via a GPIB interface. */

#include <stdio.h>
#include <math.h>
#include <stdlib.h>
#include <string.h>
#include <decl.h>

/* strdel() */
/* deletes character from string */

void strdel(char str[], int n)
{
    strcpy(&str[n], &str[n+1]);
}

/* asc_convert() */
/* returns floating point values from ascii string */

void asc_convert(char wave[], float value[])
{
    int count2,points=0,time,num,count;
    int position;
    char temp[12];

    count = 0;
    while(count < 19000)
    {
        if(wave[count] != ' ' && wave[count] != '\n')
        {
            count2 = 0;
            while(wave[count] != ' ' && wave[count] != '\n')
            {
                /* printf("\n wave[%d] = %c",count,wave[count]); */
                temp[count2++] = wave[count++];
            }
            for(position = count2; position<11; position++)
            {
                strdel(temp,count2);
            }
            value[points] = atof(temp);
            /* printf("\ntemp = %s\n",temp); */
            printf("\nvalue[%d] = %f\n",points,value[points]); /*
            points++;
        }
        else
            count++;
    }
}

main()
{
    char command1[70],command2[70],command3[70],command4[70],command5[70];
    char command6[70],command7[70],command8[70],command9[70],comm10[70];
    char comm11[70],comm12[70],comm13[70],comm14[70],comm15[70],comm16[70];
    int lec, board, start, count=0, i;
    char wave[21000];
    char port[] = "GPIB0";
    char device5[] = "DEV5";
    float value[1500];
    FILE *fp1, *fp2;

```

THIS PAGE IS
 OF POOR QUALITY

```

if ((board = ibfind (pc)) < 0) printf(" can't find board\n");
if ((lec = ibfind (device5)) < 0) printf(" can't find device\n");
if ( (fp1 = fopen( "rod1.dat","w" )) != NULL )
if ( (fp2 = fopen( "rod2.dat","w" )) != NULL )

/* Create useful strings for communicating with the LeCroy */
#define command1 "GR10 DUAL"
#define command2 "TUIV .5S"
#define command3 "C1:VBIV 20MV"
#define command4 "C2:VBIV 20MV"
#define command5 "C1:TRGL NEG"
#define command6 "TRMD SINGLE"
#define command7 "TRDL .5S"
#define command8 "CHDR OFF"
#define command9 "C2:TRCP DC"
#define comm10 "C1:CPL D50"
#define comm11 "C2:CPL D50"
#define comm12 "C1:INSP? 'SIMPLE',FLOAT"
#define comm13 "C2:INSP? 'SIMPLE',FLOAT"
#define comm14 "WFSU SF,0,NP,1500,FP,24800"
#define comm15 "CMFT DEF9,BYTE,BIN"

/* ibclr(lec); */
ibwrt(lec,command1,9);
ibwrt(lec,command2,8);
/* ibwrt(lec,command3,12); */
ibwrt(lec,command4,12); /*
ibwrt(lec,command5,11);
ibwrt(lec,command6,11);
ibwrt(lec,command7,8);
ibwrt(lec,command8,8);
ibwrt(lec,command9,10);
ibwrt(lec,comm10,10);
ibwrt(lec,comm11,10);
ibwrt(lec,comm14,26);
ibwrt(lec,comm15,18);

ibwrt(lec,comm12,23);
ibrd(lec,wave,20000);
printf("\n FILTER1 DATA = %s\n",wave);
asc_convert(wave,value);

for( i=0; i<1425; i++)
fprintf( fp1, "\n%f", value[i]);
fclose( fp1 );

ibwrt(lec,comm13,23);
ibrd(lec,wave,20000);
printf("\n FILTER2 DATA = %s\n",wave);
asc_convert(wave,value);

for( i=0; i<1425; i++)
fprintf( fp2, "\n%f", value[i]);
fclose( fp2 );

ibclr(lec);
ibsic(board);
ibsr(board,0);
ibsic(board);
)

```

Appendix F.
Published Papers Relating to
Fiber Optic Holography

Correlation-Based Fiber Sensor Using A Holographic Matched Filter

PINYI ZHANG, KIMBERLY D. BENNETT, AND GUY INDEBETOUW

Abstract—The principle of a fiber sensor based on an optical correlation technique is described and assessed for its feasibility. The device measures the correlation between the far-field radiation pattern of a multimode sensing fiber and a reference pattern stored in a holographic matched filter. The output is expected to be a monotonically decreasing function of the changes in the pattern caused by the perturbation applied to the fiber. The results of some preliminary experiments are discussed and some drawbacks of the technique are pointed out.

INTRODUCTION

MOST fiber sensors based on interferometry are very sensitive and cyclic. In many applications, however, the output should ideally be a monotonous function of a perturbation (strain, temperature changes, etc.). In this paper, we explore the possibility of using a matched filtering technique to achieve this goal. To our knowledge, matched filtering techniques have not been studied in connection with fiber sensors. Yet, modern fiber technology and holographic techniques have sufficient maturity to justify a study of the potential usefulness of such an approach. The aim of this paper is to present the results of some preliminary experiments assessing the feasibility of the technique.

MATCHED FILTERING OF FIBER OUTPUT

Holographic matched filtering techniques [1] have been used extensively for optical signal detection, pattern recognition, and the measurement of pattern difference [2]. These applications are based on the measurement of the correlation between a reference pattern which has been stored on a hologram and a different pattern or the same pattern which has undergone some changes. The correlation peak is taken as a measure of the similitude of the two patterns or of the changes which have affected it.

A fiber sensor based on this principle would use the changes in the far-field radiation pattern of a multimode

fiber which occur when the fiber is being perturbed. The output of the sensor is the degree of correlation between the modified pattern and the original pattern stored holographically. This output is expected to drop monotonically with increased perturbation.

There are two possible ways of incorporating a holographic matched filter with a fiber sensor. The first uses a transmission hologram (Fig. 1) and the second uses a reflection hologram (Fig. 2). In the device of Fig. 1, the hologram is recorded by mixing the far-field radiation pattern $\tilde{E}_0(\mu, \eta)$ of the multimode test or signal fiber with that of a single-mode fiber $R(\mu, \eta)$ excited with light from the same laser. The far-field pattern of the fiber is proportional to the Fourier transform of the field distribution $E_0(x, y)$ at its output end. For a multimode fiber, the far field is a speckle pattern with a speckle distribution which depends on the fiber's numerical aperture. The far field of the single mode is taken as a reference beam.

In Fig. 1, the far fields of the fibers are taken at the output side of a quarter-pitch GRIN lens. This has the advantage of small size, ruggedness, and tolerance to mechanical vibration during the hologram recording. The entire structure is also sufficiently compact to be sealed into a single unit.

After development, the amplitude transmittance of the hologram has the form

$$T(\mu, \eta) \propto |\tilde{E}_0(\mu, \eta) + R(\mu - \mu_0, \eta)|^2 \quad (1)$$

where μ_0 is the average angular displacement of the two interfering beams. The result of this average displacement is that the developed hologram acts as a grating, diffracting an incident beam into the angular directions $\pm\mu_0$. For example, if the hologram is illuminated by the far-field pattern $\tilde{E}(\mu, \eta)$ of the perturbed signal fiber, as shown in Fig. 1(b), one of the diffracted beams will travel in the same average direction, μ_0 as that of the reference beam. The amplitude of this beam, at the output of the hologram is

$$\tilde{C}(\mu, \eta) \propto \tilde{E}(\mu, \eta)\tilde{E}_0(\mu, \eta)R(\mu - \mu_0, \eta). \quad (2)$$

A second GRIN lens focuses this beam into an amplitude distribution which is proportional to the inverse Fourier transform of $\tilde{C}(\mu, \eta)$. From the correlation theorem of Fourier transforms, this amplitude distribution is proportional to the two-dimensional correlation of the output field of the perturbed fiber with that of the unperturbed

Manuscript received April 6, 1989; revised February 17, 1990.

P. Zhang is with the Electrical Engineering Department, Virginia Polytechnic Institute and State University, Blacksburg, VA 24061 on leave from the Physics Department, Tianjin Normal University, Tianjin, The People's Republic of China.

K. D. Bennett is with the Electrical Engineering Department, Virginia Polytechnic Institute and State University, Blacksburg, VA 24061.

G. Indebetouw is with the Physics Department, Virginia Polytechnic Institute and State University, Blacksburg, VA 24061.

IEEE Log Number 9035459.

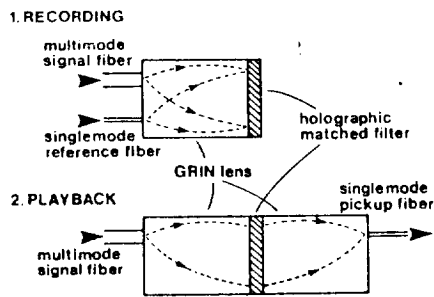


Fig. 1. Fiber sensor using a transmission holographic matched filter. 1) Recording of the matched filter as a hologram of the far-field speckle pattern at the output of the multimode signal fiber. 2) Real-time measurement of the correlation of the signal-fiber output with the stored pattern.

fiber:

$$C(x, y) \propto \int E(x', y') E_0^*(x' - x, y' - y) dx' dy'. \quad (3)$$

The correlation peak (i.e., the square of the value of the correlation distribution at the origin) is conveniently used as a measure of the similitude of the two patterns. As shown in Fig. 1(b), the correlation peak can be estimated by measuring the energy coupled into a pick-up single-mode fiber centered where the reference beam would come to a focus at the output of the second GRIN lens. The pick-up fiber acts as a spatial filter and the power delivered to a detector gives a signal proportional to

$$c_0 = \left| \int E(x, y) E_0^*(x, y) dx dy \right|^2. \quad (4)$$

This signal varies from a maximum when the two patterns are identical to a small value when they become uncorrelated.

The pattern used in this correlation technique is the far-field speckle pattern of a multimode fiber. This pattern results from the interference of a large number of modes with uncorrelated phases. As the fiber is perturbed, the relative phase of these modes changes, and so does the speckle pattern. We therefore expect the perturbed pattern to be completely uncorrelated with the original one when the relative phase of the modes has changed, in average, by about π . The amount of perturbation necessary to produce such a result depends on the effective number of speckles on the hologram. Just as the fringe sharpness of an N -beam interferometer increases proportionally to N , we expect the rate at which the correlation peak drops with increased perturbation to sharpen with the number of speckles in the hologram. This offers a simple means of tailoring the sensitivity of the device to different applications.

When the two patterns become uncorrelated, the correlation peak drops to a small value. Further changes in the perturbed pattern can never bring it back to its original shape, so the average correlation peak value remains small. It may, however, exhibit random fluctuations, the average amplitude of which depends on the exact statistical property of the pattern.

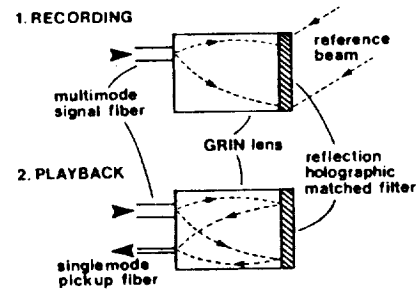


Fig. 2. Same as Fig. 1 but using a reflection holographic matched filter.

Fig. 2 shows a similar arrangement using a reflection hologram as a matched filter. With this configuration, it is easier to use an external reference beam such as a plane wave to record the hologram. The correlation peak is again proportional to the energy coupled into a single-mode pick up fiber located where the reference beam is brought into a focus by the GRIN lens. Reflection holograms require more demanding conditions of stability for their recording but they have a unique advantage. They can be made spectrally and angularly selective, an invaluable property for the design of many multiplexing schemes.

Although it is outside the scope of this paper to discuss specific design considerations, it should be mentioned that the choice of a holographic material is open to a broad range of possibilities, from photoemulsions, dichromated gelatins, or photoresists for permanent holograms to reusable materials such as thermoplastics or photoconductive devices [3].

EXPERIMENTAL RESULTS.

To check the feasibility of the idea described in the previous section, we constructed a matched filter by recording the interference of the far-field pattern of a multimode fiber with a plane wave. For these first experiments, we used a conventional lens with a 15-cm focal length instead of a GRIN lens. The hologram was about 1.5 cm in diameter and the average speckle size was approximately 3 mm. In later experiments, we made holograms with a GRIN lens having an approximate quarter pitch of 10 mm. The dimensions of the speckle and the hologram were then reduced proportionally by a factor of 15. The correlation peak was selected by a 25- μm pinhole and measured by a photodetector. The technique used to stress the fiber was simple but crude. Two areas of fiber about 15 cm apart were stripped of their cladding and glued at the top of two vertical rods. The unit of strain was taken as that produced by a 100- μm translation of one of the rods.

The value of the correlation peak as a function of strain is shown in Fig. 3. It is seen to drop monotonically and then to fluctuate somewhat randomly. With this particular hologram, the amplitude of these fluctuations were rather large because the speckle field included a few speckles of larger size than average. To test the reversibility of the measurement, the strain on the fiber was reduced. The signal followed the same curve back, within experimental error, except for a loss of correlation smaller than 10%

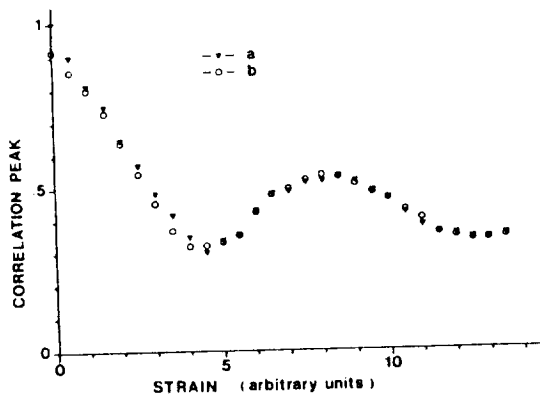


Fig. 3. Correlation peak value as a function of applied strain. The strain is measured in units of $100\ \mu\text{m}$ stretching of a section of fiber (see text for details). a) Increasing strain. b) Decreasing strain.

near the maximum. This can easily be accounted for by some irreversible factors in the way the strain was applied to the fiber. Several runs with increasing and decreasing strain gave reproducible results, within experimental errors.

In most holographic matched filtering setups, repositioning the hologram is a critical issue. It is clear that a translation of the hologram by an amount comparable to the average speckle size has the same effect on the correlation peak as that of a change of the input pattern corresponding to a 100% decorrelation. To estimate this effect quantitatively, we made another hologram, with speckles more evenly distributed in size. We compared the value of the correlation peak versus strain with the hologram correctly positioned with the result with the hologram translated by 1 and 2 mm. The result is shown in Fig. 4 where the hologram displacement is measured in terms of the angular shift $\epsilon = \Delta/f$, where Δ is the lateral translation of the hologram and f is the focal length of the lens. For example, the same effect as that shown in trace b, which corresponds to a 1 mm translation of the hologram in our setup (i.e., $\epsilon \approx 7 \times 10^{-3}$), would be obtained with a $70\text{-}\mu\text{m}$ translation of a hologram taken with a GRIN lens of 10-mm quarter pitch.

A factor of perhaps more critical importance than hologram repositioning is the fact that in such a sensor, the launching conditions must be invariant. Indeed, a slight change of coupling conditions may produce great changes in the far-field speckle pattern, making it necessary to record a new hologram. There are two ways to possibly alleviate this difficulty. One is to use sealed devices in which the input conditions will not change unless the entire unit has to be replaced. The other is to use a real-time holographic technique, at the price of increasing the technical difficulty by several orders of magnitude.

CONCLUSION

We have described a fiber sensor based on a holographic matched filtering technique. Incorporating a holographic filter into a fiber sensor may, at first sight, ap-

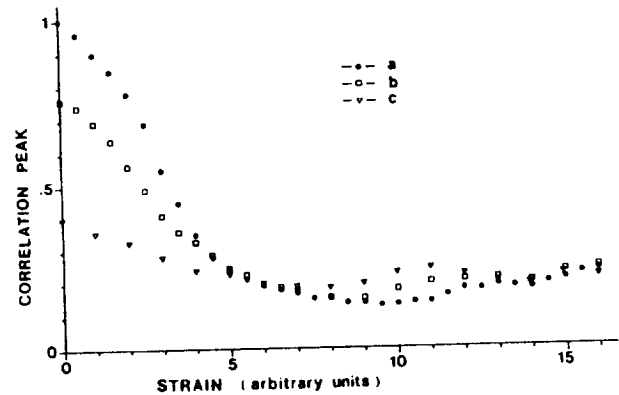


Fig. 4. Correlation peak value as a function of strain for various positioning errors of the hologram. a) Hologram in perfect position; b) angular positioning error $\epsilon = 7 \times 10^{-3}$; and c) angular positioning error $\epsilon = 1.5 \times 10^{-2}$ (see text for definition).

pear to be an unnecessarily complicated proposal. Some preliminary experiments have shown, however, that the systems requirements are by far less critical than were originally expected. The system is relatively easy to align and the method is reproducible.

This new type of sensor opens up a number of design possibilities. For example, the mode pattern used can be tailored to the selective detection of a particular physical observable, if this observable affects different modes differently. The mode pattern can also be modified to vary the sensor's sensitivity. Finally, the hologram can be multiplexed for the simultaneous detection of several parameters.

Some preliminary results were obtained using the speckle field at the output of a multimode fiber. From these experiments, the main drawback of the technique appears to be that the speckle field is not only sensitive to the measured fiber's perturbation but also depends on the launching conditions and on the quality of the fiber's end. A hard-sealed device or a real-time holographic technique could presumably alleviate this problem.

As a final point, one may mention that there exists other possible means of measuring changes in the far-field speckle pattern of a multimode fiber. Speckle interferometry is an example.

ACKNOWLEDGMENT

We would like to thank several members of the Fiber Optics Research Center at Virginia Tech. for many discussions and technical advice. This includes R. O. Claus, R. G. May, and K. A. Murphy.

REFERENCES

- [1] A. B. Vander Lugt, "Signal detection by complex spatial filtering," *IEEE Trans. Inform. Theory*, vol. IT-10, pp. 134-145, 1964.
- [2] S. P. Almeida and G. Indebetouw, in *Applications of Optical Fourier Transforms*, H. Stark, Ed. New York: Academic, 1982, ch.2.
- [3] H. M. Smith, Ed., *Holographic Recording Materials*. New York: Springer, 1977.

Holographic Matched Filter for Full-Field In-Line Signal Processing of Optical-Fiber Sensor Outputs

GUY INDEBETOUW, KIM D. BENNETT, PINYI ZHANG, AND RUSSELL G. MAY, MEMBER, IEEE

Abstract—A holographic matched filter is used to measure the changes in the output of a dual-mode fiber undergoing axial strain. The hologram is formed by interfering collimated light from a single-mode reference fiber and an unstrained dual-mode sensor fiber on a small piece of holographic material. When the hologram is illuminated by the strained sensor fiber, the cross-correlation field comparing the dual-mode output and its previous state, as recorded in the hologram, is collected, focused into a pick-up fiber, and sent to a photodiode. This arrangement allows for a compact, in-line method for full-field processing of the strain-induced changes in phase and amplitude in the sensor fiber. Other uses of such fiber-based correlators are suggested.

I. INTRODUCTION

IT has now been well over ten years since research in the field of fiber-optic sensors began in earnest. Workers have reported monitoring a host of mechanical and environmental observables, such as strain and temperature, by causing the observable to interact with one of the fundamental parameters of the light inside a fiber. These include the optical phase, intensity, wavelength, polarization, modal content, and propagation time. It is well known that the most sensitive fiber transduction mechanism involves modulation of the optical phase of either the light in one single-mode fiber with respect to that in another fiber [1] or the light in a mode versus that in another mode within a single fiber [2]. The latter method, herein referred to as modal domain sensing, has received much attention in the literature, and has been successfully applied to the measurement of such perturbations as acoustic emissions and structural vibrations, as well as electric current, temperature fluctuations, and simply induced axial strain [3]–[8].

The most basic modal domain sensor consists of a single-mode fiber operated slightly below its cutoff wave-

length, such that only the two lowest order modes propagate. For ordinary communications-grade fiber, this implies that the LP_{01} and LP_{11} modes are employed, generally resulting in a two-lobe interference pattern in the output, represented in Fig. 1. It can be seen analytically that as the fiber is axially strained, power in the output is transferred periodically from one lobe to the other [7]. That is, a dual-mode fiber can act as a strain sensor by monitoring the intensity of one or both output lobes. Detection is most often accomplished by imaging a single lobe, or part of a lobe, onto a photodiode through a pinhole. Sensors based on this mechanism are predictably three orders of magnitude less sensitive than conventional two-fiber interferometers [2], [9], but they offer the advantages of stability and simplicity, while retaining high sensitivity relative to other fiber-optic sensor types. It has also been pointed out that sensitivity could be significantly enhanced with the use of a specialty fiber which was designed to increase the difference between intermodal phase velocities.

A concern with modal domain sensors arises from the fact that most of the energy emerging from the fiber does not reach the detector. Also, the position of the detector in the output field is important to maintaining the highest signal quality. This can present complications in systems involving long-wavelength radiation, in miniaturized or encapsulated devices, and especially in sensors utilizing many modes.

One approach aimed at addressing these concerns has been to employ a detector array which collects intensity information from the entire output field [10]. Computations are then performed in order to track the movement of the lobes and infer the fiber strain. It is noted, however, that a trade-off exists between resolution and processing time. For example, a typical charge-coupled device (CCD) array containing several thousand individual elements offers high spatial resolution of the output field, but complicates the electronic processing requirements and increases the processing time, as well as raises the system cost. The optimum number of detector elements varies depending on the number and arrangement of lobes in the output and the strain mechanism being monitored.

In this paper, we explore the possibility of using holographic matched filters [11] as full-field signal-processing elements. To our knowledge, matched filtering and opti-

Manuscript received September 8, 1989; revised January 9, 1990. The work of P. Z. Zhang was supported by the NASA Langley Research Center, Hampton, VA, under Grant NAG-1-831 and by the Virginia Center for Innovative Technology under Grant TDC-86-001-03.

G. Indebetouw is with the Department of Physics, Virginia Polytechnic Institute and State University, Blacksburg, VA 24067.

K. D. Bennett and R. G. May are with the Fiber and Electro-Optics Research Center, Bradley Department of Electrical Engineering, Virginia Polytechnic Institute and State University, Blacksburg, VA 24061.

P. Z. Zhang is with the Fiber and Electro-Optics Research Center, Bradley Department of Electrical Engineering, Virginia Polytechnic Institute and State University, Blacksburg, VA 24061, on leave from the Department of Physics, Tianjin Normal University, Tianjin, People's Republic of China.

IEEE Log Number 9034659.

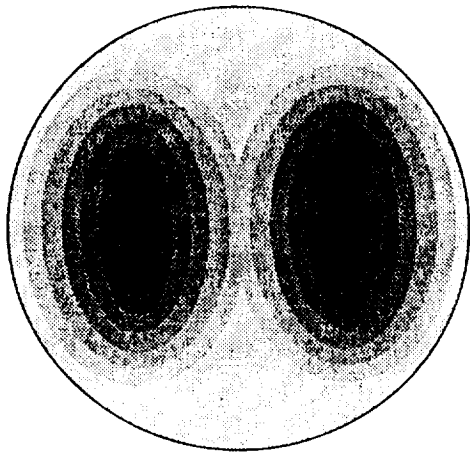


Fig. 1. Representation of a two-lobe pattern typically observed emerging from a dual-mode fiber.

cal correlation [12] methods have not been studied in connection with optical-fiber sensors, although using a hologram to provide the reference beam in a multimode acoustic sensor has been proposed [13]. Yet modern fiber technology and holographic techniques have sufficient maturity to justify a study of the potential usefulness of such an approach.

The paper is organized as follows. In the next section, we develop the theory of an optical correlator with a holographic filter matched to the pattern of a dual-mode fiber, and derive an expression for the output of the correlator as a function of fiber strain. In Section III, we discuss some approximate relationships useful in calculating the values of several parameters needed for a particular setup. The results of preliminary experiments are described in Section IV and are followed by a conclusion and some final remarks.

II. THEORY

The device to be analyzed is shown in Fig. 2. We first describe briefly the principle of its operation and then study it quantitatively.

The far-field pattern of the dual-mode sensor fiber is recorded holographically on the back face of a quarter-pitch GRIN lens. The reference beam which is made to interfere with the mode pattern for this recording is provided by a single-mode reference fiber. Upon illumination with the field from the strained sensor fiber, the developed hologram acts as a matched filter, reconstructing a distorted reference beam. This beam is focused by a second GRIN lens on the input face of a single-mode pick-up fiber. This fiber acts as a spatial filter, and the amount of power detected is proportional to the cross correlation of the pattern emerging from the strained fiber and that recorded on the hologram. This correlation signal measures the similitude of the two patterns and consequently is a measure of the strain-induced changes.

Using the terminology of holography, we call the field exiting the sensing fiber when recording the hologram the object field. In our experiment, the sensing fiber was a

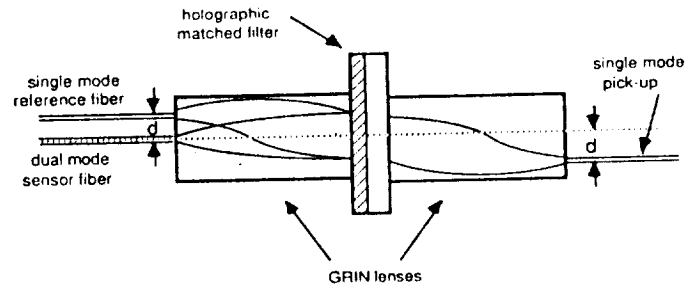


Fig. 2. Miniaturized optical correlation using quarter-pitch GRIN lenses and a holographic matched filter.

two-mode fiber. Under the assumption of weak guidance, wherein the difference between the core and cladding refractive indexes is considered to be small, the object field can in general be written as the sum of the LP_{01} and the LP_{11} pseudomodes [2]

$$F_{\text{Obj}}(r) = E_0 + E_{1e} + E_{1o} \quad (1)$$

with

$$E_0 = A_0 f_0(r) e^{-i\theta_0} \quad (2a)$$

for the LP_{01} mode, and

$$E_{1e} = A_{1e} f_1(r) \cos \phi e^{-i\theta_{1e}} \quad (2b)$$

$$E_{1o} = A_{1o} f_1(r) \sin \phi e^{-i\theta_{1o}} \quad (2c)$$

for the even and odd LP_{11} mode. In these expressions, A_n 's are constants, and ϕ is the azimuthal angle in a plane normal to the direction of propagation. The phase terms θ_n can be expressed as $(\beta_n z_0 - \theta_i)$, where the β_n terms are the propagation constants of the LP_{n1} modes, z_0 is the length of the fiber, and θ_i is some arbitrary initial phase. The transverse amplitude distributions are included in the factors $f_n(r)$

$$f_n(r) = J_n(ur/a), \quad \text{for } r < a \quad (3a)$$

$$f_n(r) = K_n(wr/a), \quad \text{for } r > a \quad (3b)$$

where J_n and K_n are the n th-order Bessel function of the first kind, and the modified Bessel function of the second kind, respectively. Furthermore

$$u = k_0 a \sqrt{n_1^2 - (\beta/k_0)^2} \quad (4a)$$

$$w = k_0 a \sqrt{(\beta/k_0)^2 - n_2^2} \quad (4b)$$

where a is the fiber core radius, k_0 is the wavenumber in free space, and n_1 and n_2 are the indexes of refraction of the core and the cladding, respectively. The appropriate boundary conditions at $r = a$ are assumed satisfied by a proper choice of the constants. Similarly, the field at the exit of the single-mode reference fiber can be written as

$$F_{\text{Ref}}(r) = A_R f_0(r) e^{-i(\beta_R z_R - \theta_R)} \quad (5)$$

The fields in (2) and (5) are all oscillating at the same frequency ω and are assumed to be mutually coherent. This will be the case if the object and the reference fibers are excited with radiation from the same laser and if the

time of propagation in the two fibers differs by less than the coherence time of the source. Under these conditions, the object and reference fields can interfere to form a hologram. It is further assumed that all the fields are in the same polarization. If it were not, one should project each field onto two orthogonal sets and superpose the two independent holograms thus formed.

Measuring all phases relative to the phase of the reference field at the exit of the reference fiber, the total amplitude distribution in the front plane of the first lens can be written as

$$U(\mathbf{r}) = F_{\text{Obj}}(\mathbf{r}) + F_{\text{Ref}}(\mathbf{r} - d\hat{\mathbf{x}}) \quad (6)$$

with

$$F_{\text{Obj}}(\mathbf{r}) = A_0 f_0(\mathbf{r}) e^{-i\theta_0} + A_{1e} f_1(\mathbf{r}) \cos \phi e^{-i\theta_{1e}} + A_{1o} f_1(\mathbf{r}) \sin \phi e^{-i\theta_{1o}} \quad (7)$$

and $F_{\text{Ref}}(\mathbf{r})$ is given in (5), and where $\hat{\mathbf{x}}$ is a unit vector along the x axis. Equation (6) reflects the fact that the object (or sensing) fiber is centered on the axis of the lens, while the reference fiber is offset by a distance d along the x axis, as seen in Fig. 2.

Stress-induced axial strain in the sensing fiber introduces an additional relative phase shift between the LP₀₁ and LP₁₁ modes; these changes are presumed to be large relative to any changes in their constituent vector modes. Calling this phase shift θ_s , the field at the output of the stressed sensing fiber can be written as

$$F_S(\mathbf{r}) = A_0 f_0(\mathbf{r}) e^{-i(\theta_0 + \theta_s)} + A_{1e} f_1(\mathbf{r}) \cos \phi e^{-i\theta_{1e}} + A_{1o} f_1(\mathbf{r}) \sin \phi e^{-i\theta_{1o}} \quad (8)$$

where an unessential phase factor has been dropped.

Within the limit of paraxial approximation, the relationship between the field amplitudes in the front and back faces of the quarter-pitch lens is the same as that between the front and back focal planes of a conventional lens. A plane wave entering the lens at an angle α with respect to its axis is focused on its back face at a lateral distance $d = 2Z\alpha/\pi$ from the axis, where Z is the length of the GRIN lens. Similarly, a point source in its front plane exits as a plane wave. Thus, the field in the back plane of the lens is proportional to the Fourier transform of the field in its front plane [14] as for a conventional lens, provided that we replace the focal length of the conventional lens by

$$f = 2Z/\pi. \quad (9)$$

Denoting the Fourier transform by a tilde, we have

$$\tilde{U}(\rho) = \tilde{F}_{\text{Obj}}(\rho) + \tilde{F}_{\text{Ref}}(\rho) e^{+i2\pi\xi d/\lambda f} \quad (10)$$

where ρ is the coordinate vector in the plane of the hologram, ξ is the axis parallel to the x axis, λ is the wavelength *in vacuo*, and f is the effective focal length of the lens. Expression (10) is the sum of two terms, the object field traveling on axis, and the reference field traveling at an angle $\theta = \sin^{-1}(d/f)$ with respect to the z axis. The

interference of these two fields is recorded on a quadratic medium to form the hologram.

As is customary, we assume that the hologram is recorded linearly. This means that after appropriate processing, the amplitude transmittance of the hologram is proportional to the local intensity with which it was irradiated. The hologram amplitude transmittance can thus be written as

$$T_H(\rho) = T_0(\rho) + \Delta T(\rho) e^{+i2\pi\xi d/\lambda f} + \Delta T^*(\rho) e^{-i2\pi\xi d/\lambda f} \quad (11a)$$

where

$$T_0(\rho) = \eta \left[\left| \tilde{F}_{\text{Obj}}(\rho) \right|^2 + \left| \tilde{F}_{\text{Ref}}(\rho) \right|^2 \right] \quad (11b)$$

and

$$\Delta T(\rho) = \eta \tilde{F}_{\text{Obj}}^*(\rho) \tilde{F}_{\text{Ref}}(\rho). \quad (11c)$$

Here, η is a constant of proportionality and $*$ indicates a complex conjugation.

In the sensing mode, the hologram is illuminated by the field $\tilde{F}_S(\rho)$ from the strained sensing fiber. The part of the field carrying the correlation information is the component scattered by the hologram in the same direction θ as the original reference field, shown in Fig. 2. Using (8) and (11), this component is found to be

$$\tilde{U}(\rho) = \eta \tilde{F}_S(\rho) \tilde{F}_{\text{Obj}}^*(\rho) \tilde{F}_{\text{Ref}}(\rho) e^{+i2\pi\xi d/\lambda f}. \quad (12)$$

The field in the back plane of the second lens is again proportional to the Fourier transform of the total field scattered by the hologram. The component $\tilde{U}_H(\rho)$ produces a distribution centered at a point located a distance d from the axis and proportional to

$$U_H(\mathbf{r}) \propto [F_S(\mathbf{r}) \otimes F_{\text{Obj}}(\mathbf{r})] \star F_{\text{Ref}}(\mathbf{r}) \star \delta(\mathbf{r} - d\hat{\mathbf{x}}) \quad (13)$$

where \star and \otimes stand for convolution and correlation operations, respectively. In obtaining (13), it was assumed that the two GRIN lenses were identical. A second lens of different focal length would only introduce a scaling of the distribution [14]. As can be inferred from (11a), the two other waves scattered by the hologram are traveling parallel to the axis and at an angle $-\theta$, respectively, so that if d is large enough, they do not overlap with the correlation term in the back plane of the second lens.

The parameter measured by the sensor is the peak of the correlation distribution described by (13). The correlation signal is proportional to the power collected by a single-mode pick-up fiber of small diameter centered at $\mathbf{r} = d\hat{\mathbf{x}}$ in the back plane of the lens. As is usually done in the analysis of the response of optical correlators [12], we will assume that the detector, or here, the core diameter of the pick-up fiber, is small compared to the width of the correlation peak. Some approximate expressions will be derived in the next section, allowing one to quantitatively estimate the needed values of these parameters. It should already be clear, however, that a trade-off will

have to be adopted. A high sensitivity is obtained with a small core diameter pick-up fiber. The price is of course a low signal level. With a large core diameter fiber, the signal contrast is considerably reduced because the total energy scattered by the hologram is, to a large extent, independent of the changes in F_S . Only the distribution of that energy, and in particular the amplitude at $r = d\xi$, is affected.

With a small core diameter pick-up fiber, the collected power is simply proportional to the correlation peak value

$$P \propto |U_H(d\xi)|^2 \propto \left| \int_0^\infty \int_0^{2\pi} F_S(r) F_{Obj}^*(r) r dr d\phi \right|^2. \quad (14)$$

Using (7) and (8), this becomes

$$P \propto \left| A_0^2 e^{-i\theta_s} \int_0^\infty f_0^2(r) 2\pi r dr + \frac{1}{2} |A_{1e}^2 + A_{1o}^2| \int_0^\infty f_1^2(r) r dr \right|^2. \quad (15)$$

The sensor output signal can be written in a normalized form as

$$P \propto 1 + m \cos \theta_s \quad (16)$$

with

$$m = \frac{2\Gamma}{1 + \Gamma^2} \quad (17a)$$

$$\Gamma = \frac{4\pi C_0 A_0^2}{C_1(A_{1e}^2 + A_{1o}^2)} \quad (17b)$$

and, using (13),

$$C_n = \int_0^a J_n^2(ur/a) r dr + \int_a^\infty K_n^2(wr/a) r dr. \quad (17c)$$

Here,

$$\theta_s = \Delta\beta z_0 - \Delta\theta_i \quad (17d)$$

where $\Delta\beta$ is the difference in propagation constants for the LP_{01} and LP_{11} modes, and $\Delta\theta_i$ is the difference between their initial phases. Significantly, this term contains z_0 , the length of the sensor fiber. Thus, (16) describes the oscillatory sensor response expected due to a strain-induced phase shift in the dual-mode fiber.

III. APPROXIMATE SOLUTIONS

In the preceding section, the relationship between the correlation signal P and the strain-induced phase shift θ_s was established. In designing a system, however, it would be useful to have additional expressions allowing one to estimate the needed values of parameters such as the hologram size or the pick-up fiber diameter. In this section, we derive some approximate expressions for this purpose. The approximation used consists of assuming that the fields at the end of the fiber falls within a Gaussian en-

velope. Comparison to the actual field profile in the core and the cladding of a weakly guiding fiber seems to confirm this assumption as being reasonable. One could further argue that the choice of an approximate beam profile is not at all critical in the theory of the correlator. It is known, for example, that except for a scaling factor, the output of the correlator is not greatly affected by spatial variations of the hologram transmittance. The quantity of importance is the change of phase distribution in the object wavefront. In fact, recording nonlinearities make amplitude distortions practically unavoidable and hardly controllable. In addition, a phase-only hologram, which has a higher throughput, a higher diffraction efficiency, and a sharper correlation peak, should be used in a practical system [15], [16]. The relationships derived in this section are not exact but may be regarded as good approximations in most practical cases.

Using the Gaussian envelope approximation, we thus write the object and reference fields of (5) and (7) in the form

$$F_{Obj}(r) = [A_0 e^{-i\theta_0} + A_{1e} \cos \phi e^{-i\theta_{1e}} + A_{1o} \sin \phi e^{-i\theta_{1o}}] e^{-(r/a_0)^2} \quad (18a)$$

and

$$F_{Ref}(r) = A_R e^{-(r/a_R)^2} \quad (18b)$$

where the radii a_0 and a_R of the Gaussian envelopes are related, but not necessarily equal to the core radii of the respective fibers. These parameters can be calculated for a best fit to the actual field profiles.

The field recorded on the hologram can be calculated by taking the Fourier transform of (18). This gives

$$\begin{aligned} \tilde{F}_H(\rho) = & [A_0 e^{-i\theta_0} + A_{1e} \cos \psi e^{-i\theta_{1e}} \\ & + A_{1o} \sin \psi e^{-i\theta_{1o}}] e^{-(\pi a_0 \rho / \lambda f)^2} \\ & + e^{-(\pi a_0 \rho / \lambda f)^2} e^{+i2\pi \xi d / \lambda f} \end{aligned} \quad (19)$$

where ψ is the azimuthal angle in the hologram plane. It should be noted that except for a scaling factor, the fields in the plane of the hologram have the same amplitude distributions as the fields exiting the fibers.

A linearly recorded hologram has an amplitude transmittance given by

$$T_H(\rho) \propto |\tilde{F}_H(\rho)|^2. \quad (20)$$

Using (19) we see that the intensity distribution in the hologram plane has a Gaussian envelope with a radius (measured at $1/e^2$) equal to

$$R_H = \frac{\lambda f}{\pi(a_0^2 + a_R^2)^{1/2}}. \quad (21)$$

The field from the strained dual mode sensing fiber can be expressed as

$$\begin{aligned} \tilde{F}_S(\rho) = & [A_0 e^{-i(\theta_0 + \theta_s)} + A_{1e} \cos \psi e^{-i\theta_{1e}} \\ & + A_{1o} \sin \psi e^{-i\theta_{1o}}] e^{-(\pi a_0 \rho)^2}. \end{aligned} \quad (22)$$

Upon illumination by this field, the hologram scatters a wave toward the pick-up fiber, which can be written as

$$\begin{aligned} \bar{U}_H(\rho) = & \eta [A_0 e^{i\theta_0} + A_{1e} \cos \psi e^{i\theta_{1e}} \\ & + A_{1o} \sin \psi e^{i\theta_{1o}}] [A_0 e^{-i(\theta_0 + \theta_s)} \\ & + A_{1e} \cos \psi e^{-i\theta_{1e}} + A_{1o} \sin \psi e^{-i\theta_{1o}}] \\ & \cdot (\exp [-\pi^2(2a_0^2 + a_R^2)\rho^2/\lambda^2 f^2]) \\ & \cdot (e^{+i2\pi\xi d/\lambda f}). \end{aligned} \quad (23)$$

This field is brought to a focus at $x = d$ in the back plane of the second lens. The amplitude distribution about that point is given by the Fourier transform of (23). From the Fourier transform of the broad Gaussian envelope, one can infer that the correlation peak, centered at $x = d$, has a radius (measured at $1/e^2$) equal to

$$R_C = (2a_0^2 + a_R^2)^{1/2}. \quad (24)$$

The general effect of a change of phase distribution at the output of the sensing fiber is to broaden the correlation peak and to reduce its amplitude. The sensitivity of the technique thus depends on the relative size of the correlation peak and a_p , the radius of the pick-up fiber core. For $a_p > R_C$, the signal is large, but the sensitivity or signal contrast is poor since the entire correlation peak is collected by the fiber. For $a_p \ll R_C$, the detected power is proportional to

$$P \propto \left| \int_0^\infty \int_0^{2\pi} \bar{U}_H(\rho) \rho \, d\rho \, d\psi \right|^2. \quad (25)$$

In this case, the sensitivity is optimum but the signal is small. A generally acceptable trade-off is to choose $a \approx R_C/n$, with $1 < n < 4$. In this case, the sensitivity remains good and the detected power is still a large fraction of the total power of the correlation peak.

Using (25), the normalized correlation signal is found to be equal to

$$P \propto 1 + m \cos \theta_s \quad (26a)$$

with

$$m = \frac{8\pi A_0^2(A_{1e}^2 + A_{1o}^2)}{16\pi^2 A_0^2 + (A_{1e}^2 + A_{1o}^2)^2} \quad (26b)$$

which is the same expression as found in the previous section if we use the approximation that $C_0/C_1 \approx 1$.

IV. INITIAL EXPERIMENT

For the sake of simplicity, the initial setup used to fabricate the holographic matched filter employed bulk optics, as depicted in Fig. 3. Light from a 5-mW polarized He-Ne laser was divided into two beams, one of which was launched into a polarization preserving single-mode optical fiber operated below its cutoff wavelength, resulting in the dual-mode operation described above. The far-field pattern was projected in the back focal plane of a 16-cm focal length lens. The reference beam was redirected, filtered, and collimated as shown. The length of fiber was

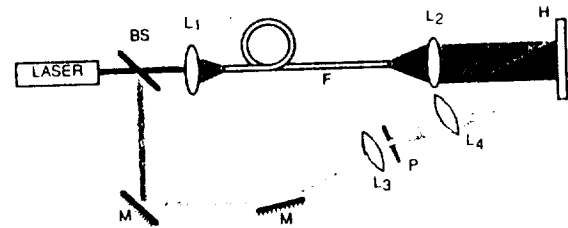


Fig. 3. Setup for holographically recording the output pattern of a dual-mode optical fiber: BS beam splitter; L lens; F dual-mode fiber; H holographic plate; M mirror; P pinhole.

chosen so as to equalize the optical path lengths of the two beams. The two beams interfered at an angle of about 30° on a 2×2 in Kodak high-speed holographic plate type 131. The diameter of the exposed area on the plate was about 4 cm. Exposure time of $\sim 1/50$ s and development of ~ 3 min in Kodak D19 yielded a reasonable diffraction efficiency, but no attempt was made to optimize this parameter.

In the sensing mode, the hologram was illuminated by the fiber output, as shown in Fig. 4. The reconstructed reference beam was focused onto a pinhole P which filtered the correlation peak. The correlation signal was detected by a silicon photodetector. The fiber was mounted rigidly between two posts, one of which was fixed, while the other was itself mounted on a micropositioner. As axial strain was applied by turning the micrometer, the fiber-output pattern changed, changing the correlation signal.

A plot of the reconstructed output intensity as a function of applied axial strain appears in Fig. 5. As was theoretically expected, increasing perturbation caused a periodic exchange of power between the lobes of the dual-mode fiber, resulting in a harmonic output. The fact that the zero strain point was not an absolute maximum in output intensity may be attributed to the spatial variation of diffraction efficiency existing in the hologram field, while the decreasing maxima result from mode coupling effects. The output of the correlator is also compared to the signal picked up by a small pinhole located near the center of one of the lobes of the far-field pattern of the fiber. Both data were arbitrarily scaled to ease the comparison. The slight difference in periodicity is due to a certain degree of irreproducibility in the method used to apply strain to the fiber.

A miniature correlator, such as that shown in Fig. 2 was also constructed and tested. In this device, the sensor and reference fibers were rigidly coupled to the front face of the first GRIN lens, and the hologram was recorded in its back face on a small piece of holographic emulsion. The hologram was about 2 mm in diameter.

After recording, developing, and repositioning the hologram, the reference fiber could be removed or decoupled from the sensor. A second GRIN lens collected the field scattered by the hologram when the latter was illuminated by light from the sensing fiber. The correlation peak was collected by the pick-up fiber and detected. The device was found to be easy to align, although a 3-D positioner was needed to accurately position the pick-up fiber.

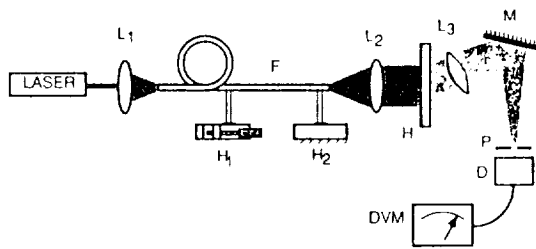


Fig. 4. Setup for using the hologram as a matched filter to detect changes in the fiber output due to axial strain: L lens; F dual-mode fiber; $H_{1(2)}$ movable (fixed) fiber holder; M mirror; FH fiber holder and positioner; H hologram; P pinhole; D photodetector; DVM digital volt meter.

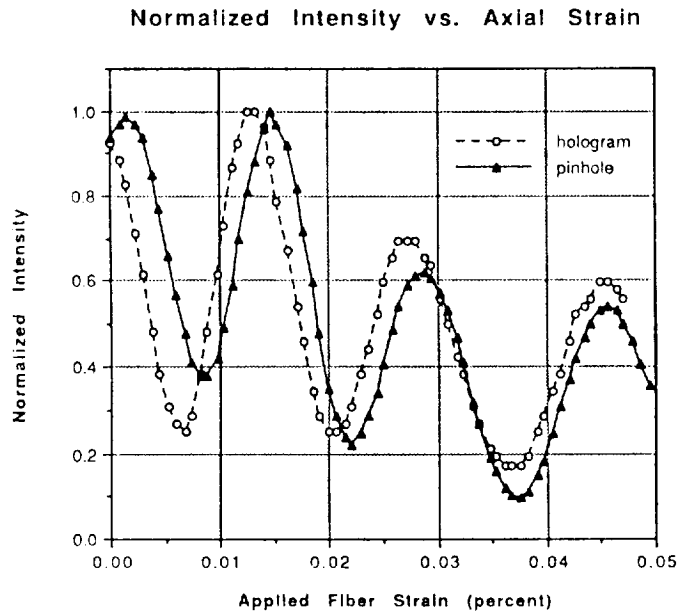


Fig. 5. Comparison of the output intensity (normalized) of the correlator using a holographic matched filter and the pinhole detection of a single lobe.

V. CONCLUSION

A method for optically processing the output of a fiber sensor has been presented. The technique makes use of a holographic matched filter to record an initial sensor state and provide a reference against which changes in the fiber output due to axial strain can be compared. The theory of the optical correlator was developed for the case of a dual-mode fiber sensor and a number of useful expressions were derived to facilitate practical implementation of the design. Initial experiments were performed to determine fiber strain, and the results agreed well both with predictions and conventional test procedures.

Several advantages accrue to the application of optical correlation methods to fiber-optic sensor technology. For one, rather than collecting light at a single point in the output field, the full-field output is collected, potentially offering higher signal power. For another, the need for precise positioning of a pinhole at the spatial Q point of the output field is considerably relaxed, especially if polarization preserving fiber is employed. A number of fundamental fiber parameters, such as core eccentricity or fiber modal content could also potentially be determined using matched filters. To this effect, fibers having a more complex mode pattern may be used in connection with

filters matched to specific modes. Multimode fibers could also be used to provide a monotonically decreasing correlation signal.

Sensing via holographic matched filtering has two additional advantages which may greatly enhance the versatility and power of the technique, namely, the capability of multiplexing and the possibility of real time operation. For example, multiple sensors, or multiple states of a single sensor could be monitored simultaneously by using a multiplexed holographic filter matched to a number of different fiber modes. Similarly, filters could be stacked or sequenced to perform logical operations on sensor outputs. Finally, real time holographic methods could be employed to provide the ability of updating the filter and allowing time-dependent measurements. These last two features are particularly appealing since they open up the possibility of applying optical data processing techniques directly on the optical signals of the sensors, that is, before transferring the data to the electronic domain. For complex or high data rate sensors, this may lead to a higher speed or more elegant architectures.

REFERENCES

- [1] C. D. Butter and G. B. Hocker, "Fiber optics strain gage," *Appl. Opt.*, vol. 17, no. 18, p. 2867, Sept. 1978.
- [2] M. R. Layton and J. A. Bucaro, "Optical fiber acoustic sensor utilizing mode-mode interference," *Appl. Opt.*, vol. 18, no. 5, p. 666, Mar. 1979.
- [3] K. D. Bennett, R. O. Claus, and M. J. Pindera, "Internal monitoring of acoustic emission in graphite/epoxy composites using embedded optical fiber sensors," in *Proc. Quant. NDE Conf.*, San Diego, CA, Aug. 1986.
- [4] K. D. Bennett and R. O. Claus, "Analysis of composite structures using fiber optic modal sensing," in *Proc. IEEE Region 3 Conf.*, Richmond, VA, Apr. 1986.
- [5] G. L. Tangonan, D. I. Persechini, R. J. Morrison, and J. A. Wysocki, "Current sensing with metal-coated multimode optical fibers," *Electron. Lett.*, vol. 16, no. 25, p. 958, 1980.
- [6] J. L. McMillan and S. C. Robertson, "Dual-mode optical-fiber interferometric sensor," *Electron. Lett.*, vol. 20, no. 3, p. 136, Feb. 1984.
- [7] B. D. Duncan, "Modal interference techniques for strain detection in few-mode optical fibers," M.S.E.E. thesis, Virginia Polytech. Instit. State Univ., Dec. 1987.
- [8] D. Kreit, R. C. Youngquist, and D. E. N. Davies, "Two-mode fiber interferometer/amplitude modulator," *Appl. Opt.*, vol. 25, no. 23, p. 4433, Dec. 1986.
- [9] B. D. Duncan, B. W. Brennan, and R. O. Claus, "Intermodal pattern modulation in optical fiber modal domain sensor systems: Experimental results," *Proc. SPIE-Int. Soc. Opt. Eng., Fiber Optic Smart Structures and Skins Conf.*, Boston, MA, Sept. 1988, vol. 986, p. 186.
- [10] K. D. Bennett, J. C. McKeeman, and R. G. May, "Full field analysis of modal domain sensor signals for structural control," *Proc. SPIE-Int. Soc. Opt. Eng., Fiber Optic Smart Structures and Skins Conf.*, Boston, MA, Sept. 1988, vol. 986, p. 186.
- [11] A. Vander Lugt, *IEEE Trans. Inform. Theory*, vol. IT-10, p. 139, 1964.
- [12] S. P. Almeida and G. Indebetouw, "Pattern recognition via complex spatial filtering," in *Applications of Optical Fourier Transform*, H. Stark, Ed. New York: Academic, 1982, ch. 2, pp. 41-81.
- [13] T. J. Hall, M. A. Fiddy, and M. S. Ner, "Detector for an optical-fiber acoustic sensor using dynamic holographic interferometry," *Opt. Lett.*, vol. 5, no. 11, p. 485, Nov. 1980.
- [14] J. W. Goodman, *Introduction to Fourier Optics*. New York: McGraw-Hill, 1968.
- [15] J. L. Horner and P. D. Gianino, "Phase only matched filtering," *Appl. Opt.*, vol. 23, no. 6, p. 812, Mar. 1984.
- [16] J. L. Horner, "Light utilization in optical correlations," *Appl. Opt.*, vol. 21, no. 24, p. 4511, Dec. 1986.